

Small Business Innovation Research Program

Phase II Final Report

SBIR 1985 Phase II

ICING SENSOR & ICE PROTECTION SYSTEM

71-03-02
2805
P, 123

Contract No. NAS3-25200

*SBIR - :03-01-4846**RELEASED: 8-9-92*

Prepared for:

National Aeronautics and Space Administration
Lewis Research Center
Cleveland, OH 44135

Prepared by:

INNOVATIVE DYNAMICS

Cornell Research Park
Langmuir Laboratories
Ithaca, NY 14850-1296Gail A. Hickman
Joseph J. Gerardi
Yong X. Feng
Ateen A. Khathkate

October 30, 1990

SBIR Rights Notice

These SBIR data are furnished with SBIR rights under NASA Contract No. NAS3-25200. For a period of 2 years after acceptance of all items to be delivered under this contract, the Government agrees to use these data for Government purposes only, and they shall not be disclosed outside the Government (including disclosure for procurement purposes) during such period without permission of the Contractor, except that, subject to the foregoing use and disclosure prohibitions, such data may be disclosed for use by support Contractors. After the aforesaid 2-year period, the government has a royalty free license to use, and to authorize others to use on its behalf, these data for government purposes, but it is relieved of all disclosure prohibitions and assumes no liability for unauthorized use of these data by third parties. This notice shall be affixed to any reproductions of this data, in whole or in part.

N94-70776

Unclas

29/03 0183155

122P(NASA-CR-194245) ICING SENSOR AND
ICE PROTECTION SYSTEM, REVISION 3
Final Report (Innovative Dynamics)
123 p*11/6/91*

Project Summary

The Icing Sensor and Ice Protection System (ISIPS) is a unique distributed system based on "smart structures" technology. By monitoring the vibration signature of a structure, the system determines ice accretion using embedded sensor arrays and electromagnetic actuators. The structure is initially excited by a low level impulse using the embedded actuator. Pattern recognition techniques are utilized to classify the sensor signals and determine the thickness and distribution pattern of leading edge ice. The memory of the system is formed through a learning process in which a systematic series of experiments is presented to the system. Once identified, leading edge ice is removed electromechanically with a high level impulse.

A prototype system has been successfully tested in a series of experiments at NASA Lewis that demonstrated the feasibility to detect and remove leading edge ice accretion. In these experiments, twenty-six features were extracted from the sensor signals, and best feature sets for classification were identified. Results are presented from tests performed in the NASA Icing Research Tunnel and on NASA's DHC-6 research aircraft showing the ability of the system to accurately identify different types of signals corresponding to changes in the physical properties of the structure resulting from ice build-up. Both active and passive sensing techniques were evaluated. The active technique utilizes an eddy coil actuator whereas the natural in-flight engine and aerodynamic noise sources are used in the passive technique. Using conventional minimum distance algorithms, system sensitivity was sufficient to detect ice accretion ranging from 0.05 inch to 0.5 inch with a recognition rate of 93%. A recognition rate of 100% was achieved with a slightly lower resolution of .075".

Although extensive training was required to teach the pattern recognition software various ice thickness signatures, it may be possible teach the system by only some representative patterns, while the missing information would be substituted algorithmically by a proper interpolation procedure. The generation of a larger ice database will enable the optimization of the feature set and decision procedure to reduce software processing overhead and increase sensitivity. Because the system can be trained to recognize changes in structural signatures, its application as an overall structural health monitor could provide the means for detecting damage within a structure in addition to providing real time ice protection.

TABLE OF CONTENTS

PROJECT SUMMARY	i
1 INTRODUCTION	
1.1 Program Overview	1
1.2 Phase II Tasks	2
1.2.1 Vibration Deicing Actuator Development/Evaluation	2
1.2.2 Impulse Deicing Actuator Development/Evaluation	3
1.2.3 Deicing Actuator Selection	4
1.2.4 Icing Sensor & Ice Protection System Design and Fabrication	4
1.2.5 Prototype System Testing	6
2 ISIPS SYSTEM DESCRIPTION	
2.1 System Operation	10
2.2 Hardware Configuration	11
3 ELECTRICAL DESIGN	
3.1 System Components	14
3.1.1 EIDI Coils	14
3.1.2 Ice Accretion Sensors	15
3.1.3 Digital Signal Processor	15
3.1.4 Analog to Digital Converter and Multiplexer	16
3.1.5 Signal Conditioner	16
3.1.6 High Voltage Power Supply	16
3.1.7 EIDI Switch	19
3.1.8 Temperature Sensor and Conditioner	20
3.2 Wiring Specifications	20
3.3 Power Specifications	22
4 MECHANICAL DESIGN	
4.1 Wing Cuff Mechanical Design	24
4.2 Wing Cuff Structural Analysis	27
5 PATTERN RECOGNITION SOFTWARE	
5.1 Description	32
5.2 Feature Extraction	33
5.2.1 Time Domain	35
5.2.2 Frequency Domain	36
5.2.3 General Properties and Curve Shape	38
5.2.4 Transfer Function	39
5.3 Classification	39
5.4 Detailed Program Structure	40

6	ICING TUNNEL TESTS	
6.1	Test Procedure	48
6.2	Results	49
6.2.1	IRT Tests	49
6.2.2	Feature Set Analysis/Optimization	49
6.2.3	Simulation Tests	56
7	FLIGHT TESTS	
7.1	Test Procedure	58
7.2	Results	59
8	CONCLUSIONS	
8.1	System Performance	64
8.2	Future Development	64
	REFERENCES	65
	APPENDIX A. Fatigue Analysis	A1
	APPENDIX B. Structural Analysis	B1
	APPENDIX C. Features Generated in IRT Training	C1

1 INTRODUCTION

1.1 Program Overview

Available methods for detecting ice accretion on aircraft are currently quite limited. Current methods are largely considered "point sensing" in that the ice must form directly over the sensor in order to detect its presence. Because ice is known to form at varying chordwise locations along the leading edge, a number of sensors must be used to ensure against failure of detecting the ice. Achieving "distributed sensing" will depend on the ability to develop a sensor which can reliably detect the ice over large areas. Recently, the concept of smart structures has arisen as an alternative to the traditional design methodology for sensing and control of structures. A smart structure is defined as a distributed sensor and actuator network embedded within the material which forms the structure. Such a structure would possess the ability to adapt, through software adjustments, to changing environments. Piezoelectric materials are excellent candidates for the role of sensors. These materials generate a charge in response to a mechanical deformation. Piezoelectric sensors have been shown to be lightweight, passive, immune to electromagnetic interference, very sensitive, and easily attached to structures without complex cutting or drilling of the surface. They can be incorporated into a structure without greatly increasing the mass or modifying its passive dynamic properties. Note, however, that piezoelectric constants are temperature dependent and must therefore be compensated accordingly.

During a Phase II program, Innovative Dynamics has developed a flightworthy prototype system referred to as the Ice Sensor and Ice Protection System (ISIPS) based on the smart structures concept. This system combines piezoelectric sensors with Electro-Impulse De-Icing (EIDI) actuators to produce a fully automatic deicing system. The principal underlying the operation of the system is the use of vibration data to determine the amount of ice accretion on the leading edge structure. Eddy-coils are pulsed at low voltage levels to mechanically excite the structure. The vibration signals are analyzed using pattern recognition techniques to classify the signals and determine ice thickness and distributions. Once a predetermined ice thickness has been detected, the eddy-coils are fired at a much higher voltage level to remove the ice. The system was demonstrated in the NASA Icing Research Tunnel (IRT) and on NASA's DHC-6 Icing Research Aircraft (IRA) (see following photos). Research results from these icing tests demonstrate the capabilities of the system to reliably detect and remove leading edge ice accretion.

The research was supported by the Small Business Innovation Research (SBIR) program of the NASA Lewis Research Center under Contract No. NAS3-25200. Innovative Dynamics performed the work over a 2 year period starting in January 1988. Joseph J. Gerardi served as Principal Investigator for the project along with Gail A. Hickman as Co-Investigator. Ateen Khakhate performed the finite element analysis studies and Y. Feng developed the pattern recognition software code. Ken Sherman and Russ Wallace designed

and constructed electronic hardware components. Dr. Zumwalt served as technical consultant on the fabrication of the wing cuff and EIDI system.

The Phase II development program consisted of basic analyses, laboratory tests, icing tunnel tests and flight tests. The following section discusses the tasks performed during the program and summarizes the results.

1.2 Phase II Tasks

Phase II was a prototype hardware demonstration focusing on development of an ice protection system for aircraft using piezoelectric film embedded or attached to a structure as the ice accretion sensor. During the previous Phase I program, the basic ice sensor concept was shown to be feasible (Contract #NAS3-24852).¹ A broadband vibration excitation source was applied to the structure. Changes in the structural vibration signature detected with the piezoelectric sensors were used as a measure of accreted ice mass on the structure. During this study, a 150 Watt voice coil was used as the sensor excitation source as well as the deicing actuator. Once a threshold ice thickness was identified, the voice coil was used to vibrate the structure at a specific resonant mode identified by the sensor to remove the ice. While this actuator was found to be efficient in exciting the sensor and removing the ice, this particular actuator is too massive for use in a practical aircraft system. During Phase II, various actuators including vibration as well as impulse type actuators were investigated. Based on results of deicing performance and estimated size, weight, and power requirements, the most promising deicing actuator was selected for development into a closed-loop system prototype. The program consisted of the following five major tasks.

1.2.1 Vibration Deicing Actuator Development/Evaluation

Task 1 investigated the development of a practical system based on a vibration deicing approach. A survey of commercially available actuators which could be used for aircraft applications was performed. Based on the results of the study, candidate actuators were then tested on a wing test section at ID using freezer ice to determine overall deicing performance: single winding voice coil (Morrell), dual winding voice coil (Kimco Magnetics), and a solenoid coil (Ledex). A comparison of actuator performance is shown in Table 1.

Of the vibration actuators tested, the overall performance of the Kimco voice coil was the most promising. The excitation used was a periodic chirp signal requiring a frequency sweep from 500 Hz to 50 Hz. Approximately 50 V was used to remove up to at least 1/4" ice thickness. The high frequencies caused the ice to crack and the low frequencies shattered the ice off the model. Total time to remove the ice was a few seconds and the total power to break the ice was approximately 300 Watts. For a given amount of energy, the Kimco coil provided an order of magnitude more force and displacement than the other

TABLE 1. Comparison of Vibration Deicing Actuator Capabilities

Actuator	Deicing Performance	Advantages	Disadvantages
Morrel Voice Coil	Poor - Glaze Ice	* High Bandwidth	* Insufficient Force (15 lb Max)
Ledex Solenoid Coil	Poor - Glaze Ice	* High Force Levels (80 lb)	* Not Push - Pull * Non-Linear Response - Low Displacement * Low Bandwidth (60 Hz)
Kimco Coil	Good - Glaze Ice	* High Displacement (0.1") * High Bandwidth * Low Voltage (200 cyc @ 50V) * Linear Response * High Efficiency (>90%)	* Larger Ice Particles & More Residual than EIDI * Higher Displacement & Stress than EIDI
EIDI	Poor - Glaze Ice		* Low Bandwidth

actuators tested. The ice, however, came off in large chunks which may not be desirable in aircraft applications.

1.2.2 Impulse Deicing Actuator Development/Evaluation

Task 2 investigated the development of a practical system based on an impulse deicing approach. The objective was to compare the deicing performance of this approach with the vibration deicing approach investigated in Task 1. The EIDI system was chosen for evaluation as the deicing actuator due to its good deicing characteristics.² The Kimco voice coil, which was demonstrated to work well in a vibration mode of operation, was also evaluated for use in an impulse mode. These actuators were installed on a wing test section and tested using freezer ice as in Task 1. Test results are summarized in Table 2.

The Kimco coil was effective in removing ice up to at least 1/4 inch thick using a 250 V impulse. This actuator generated lower stress levels in the metal when operated in the impulse mode versus the vibration mode but still higher stress levels than generated with the EIDI eddy current actuator. The main advantage of the Kimco coil is that it requires much less voltage than the eddy coil actuator. However, eddy coils are much lighter, approximately 50%. Eddy coils were also more effective in removing all types of ice tested due to the high acceleration levels obtainable with the coils.

TABLE 2. Comparison of Impulse Deicing Actuator Capabilities

Actuator	Deicing Performance	Advantages	Disadvantages
Kimco Coil	Good - Glaze Ice	<ul style="list-style-type: none"> * Lower Stress Levels on Aluminum than Kimco Chirp * Low Voltage (250V) * High Efficiency (>90%) 	<ul style="list-style-type: none"> * Larger Ice Particles & More Residual than EIDI * Lower Acceleration Levels than EIDI * Higher Displacement & Stress than EIDI
EIDI - Pulse	Good - Glaze & Rime Ice	<ul style="list-style-type: none"> * Lower Stress Levels on Aluminum than Kimco * High Acceleration (Several K g's) * Smaller Ice Particles & Less Residual than Kimco 	<ul style="list-style-type: none"> * Higher Voltage Required (600-700V) * Low Efficiency (<10%)

1.2.3 Deicing Actuator Selection

Task 3 involved selection of the most promising deicing actuator for use in the closed-loop system. Based on the icing test results, the Kimco voice coil, operated in both the vibration and impulse modes, and the EIDI eddy-coil operated in the impulse mode were the most effective in removing ice. A comparison of the size, weight and power requirements of these selected actuators was made for a typical installation on a Twin Otter aircraft. In addition, a comparison of the effects of impacting the surface with the various actuators was made. A finite element analysis was performed to determine the structure's fatigue life and is described in Appendix A. Table 3 shows the overall system performance comparison of the three actuators. Of the actuators studied, the banded mount eddy-coil was chosen as the most attractive deicing actuator for aircraft application. Banded refers to the geometric shape of the coil mounting bracket. The Kimco coil is also a promising candidate; however, to achieve comparable deicing performance, the weight must be reduced and the frequency response increased.

1.2.4 Icing Sensor & Ice Protection System Design and Fabrication

Task 4 developed the distributed piezoelectric ice sensor and the actuator into a flightworthy closed-loop prototype ice protection system. The system was designed for installation on a wing cuff that could be mounted in NASA's IRT and IRA for performance validation. Details of the system operation, electrical design, and mechanical design are presented in Sections 2, 3, and 4, respectively.

TABLE 3. System Performance Comparison for Typical Twin Otter Installation

Actuator	Size (in)	Weight (lbs)	Power (watts)	Voltage (V)	Fatigue (10 cyc)
Kimco- Vibration	6x2.5X1.5	140	300 (3 min)	50	0.03
Kimco- Impulse	6x2.5x1.5	150	140 (3 min)	250	10.0
EIDI- Bandaïd	6x2.5x0.8	90	300 (3 min)	600	42.0

Based on initial analytical and experimental test results, the original plan was to develop an algorithm to track modal frequency shifts of the structure as a function of ice buildup.³ A finite element analysis of one bay of the wing cuff was performed to determine the effect of ice accretion on the resonant modes of the leading edge, in addition to determining the optimal placement of the eddy-coils and sensors. This analysis is described in Appendix B.

During initial icing tests in the IRT, however, it was found that frequency data does not provide sufficient information to be used for reliably determining ice thickness or distribution/location. Depending on many factors such as temperature, angle of attack, liquid water content and droplet size, the type of ice that is formed as well as the distribution can vary substantially. Therefore, additional features of the vibration response of the structure are required. Due to the complex nature of icing, pattern recognition techniques were evaluated for use in analyzing the vibration patterns. These techniques have been shown to be useful in solving complicated signal processing problems.⁴ Based on these techniques, software was developed at ID to classify the sensor signals and determine the ice thickness. A patent application for processing the vibrational modes indicative of structural icing has been filed under the name "Smart Skin Ice Detection and Deicing System".

This software analyzes the digitized sensor data in a pattern space composed of waveform parameters (features) which characterize the signals. The features extracted from the time signals provide a means of identifying the ice accretion. The pattern recognition system first goes through a learning stage to extract the feature vector and to build up the statistics which describe the signals. The properties derived from the reference samples are

compared with their unknown counterparts extracted from incoming signals. By analyzing their differences and similarities, the system identifies these signals. The pattern recognition software is described in further detail in Section 5.

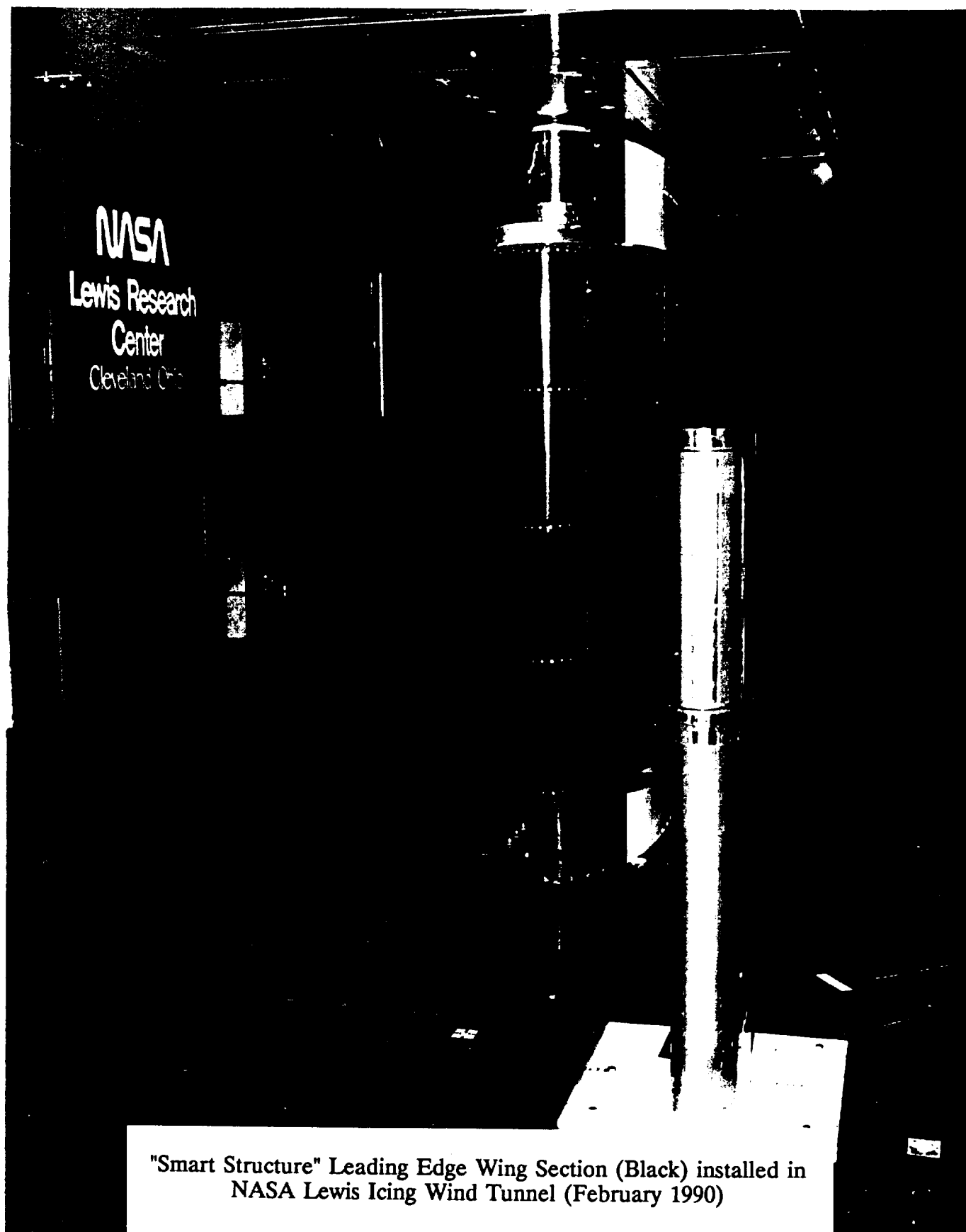
1.2.5 Prototype System Testing

This task involved prototype system testing in the NASA Icing Research Tunnel and on the NASA Icing Research Aircraft over a range of icing conditions. Results of these tests are presented in Sections 6 and 7, respectively.

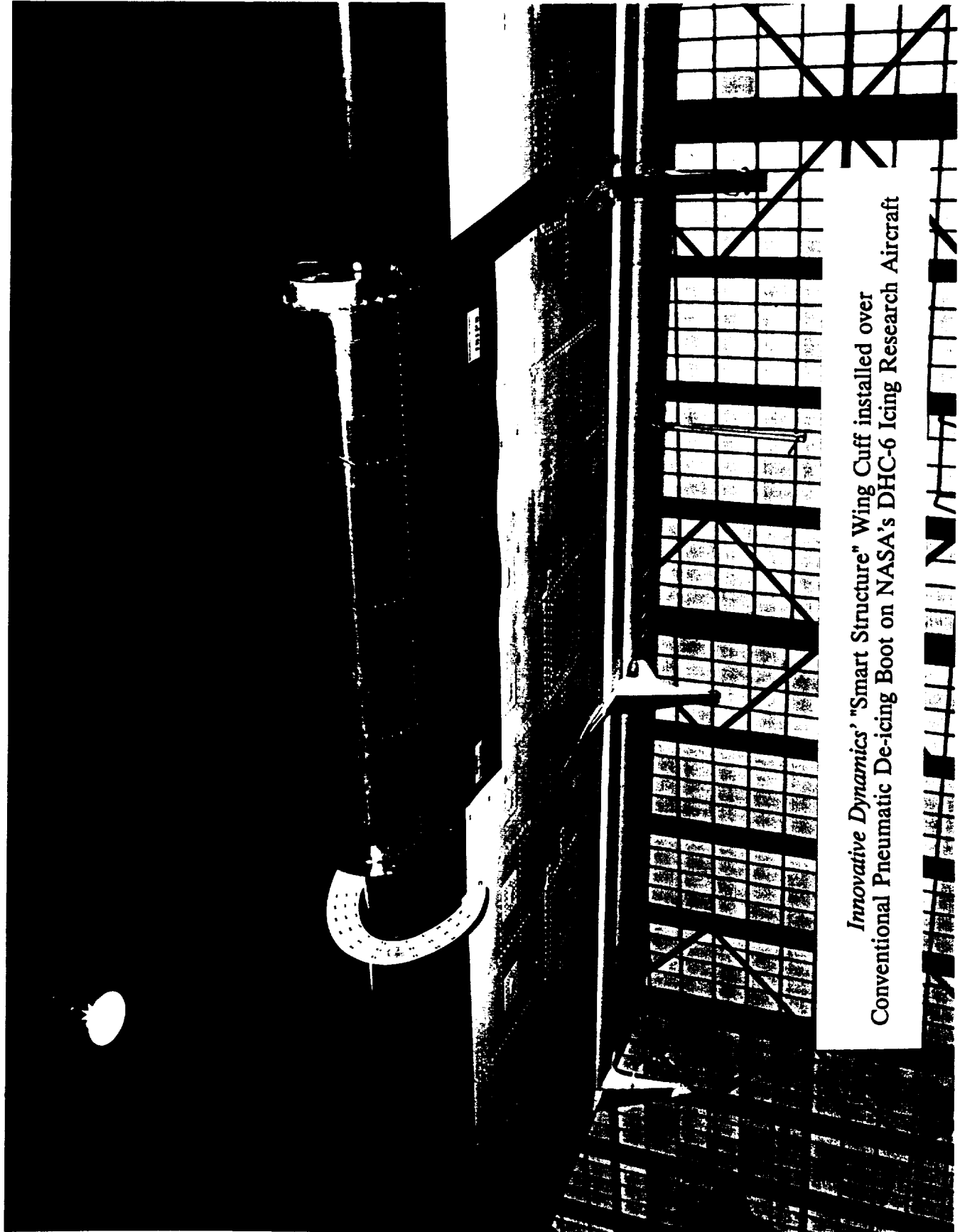
The memory of the system was formed through a learning process in which a systematic series of icing tests were presented to the system. The system was trained in the IRT for ice thickness increments of 0.05 inch up to a total thickness of 0.5 inch. The system was then tested to determine reliability and overall performance. Without any feature set optimization, the system worked well in detecting ice thickness ranging from 0 to 0.3 inch. Above 0.3 inch, the recognition rate, however, decreased. This can be explained by the fact that above 0.3 inch, several of the signal features used to classify the ice thickness tended to level out and therefore no further information could be gained about the ice buildup on the structure. Without any feature set optimization, the overall recognition rate of the system was 63.3% with a resolution of 0.05 inch. By optimizing the feature set, the recognition rate was improved to 93.3%. A recognition rate of 100% was obtained with a resolution of 0.075 inch.

The system was then installed on the IRA for in-flight system performance verification. Due to differences in installation of the cuff on the Twin Otter wing than on the tunnel test fixture, the boundary conditions of the cuff were changed enough so that the ice database generated in the tunnel could not be used. Therefore, the system had to be retrained on the aircraft. Because only limited icing conditions were available, a comprehensive database could not be generated. For the cases tested however, the system worked well. Further tests were performed using simulated ice consisting of 0.005" layers of aluminum tape attached to the leading edge of the wing cuff. The tape was positioned at the stagnation line and ran the spanwise length of the cuff. A recognition rate of 100% was achieved in detecting the simulated ice up to 4 layers thick.

In addition to these tests performed using the eddy-coil actuators, tests were performed using natural in-flight engine and aerodynamic vibration noise as the excitation source. This technique would be advantageous for application in a passive health monitoring system. Unfortunately, the results were inconclusive. The power spectral data of the sensor signals indicate that it may be possible to identify icing if the pattern features were optimized for the correct frequency range. Further research should be performed to verify this approach.

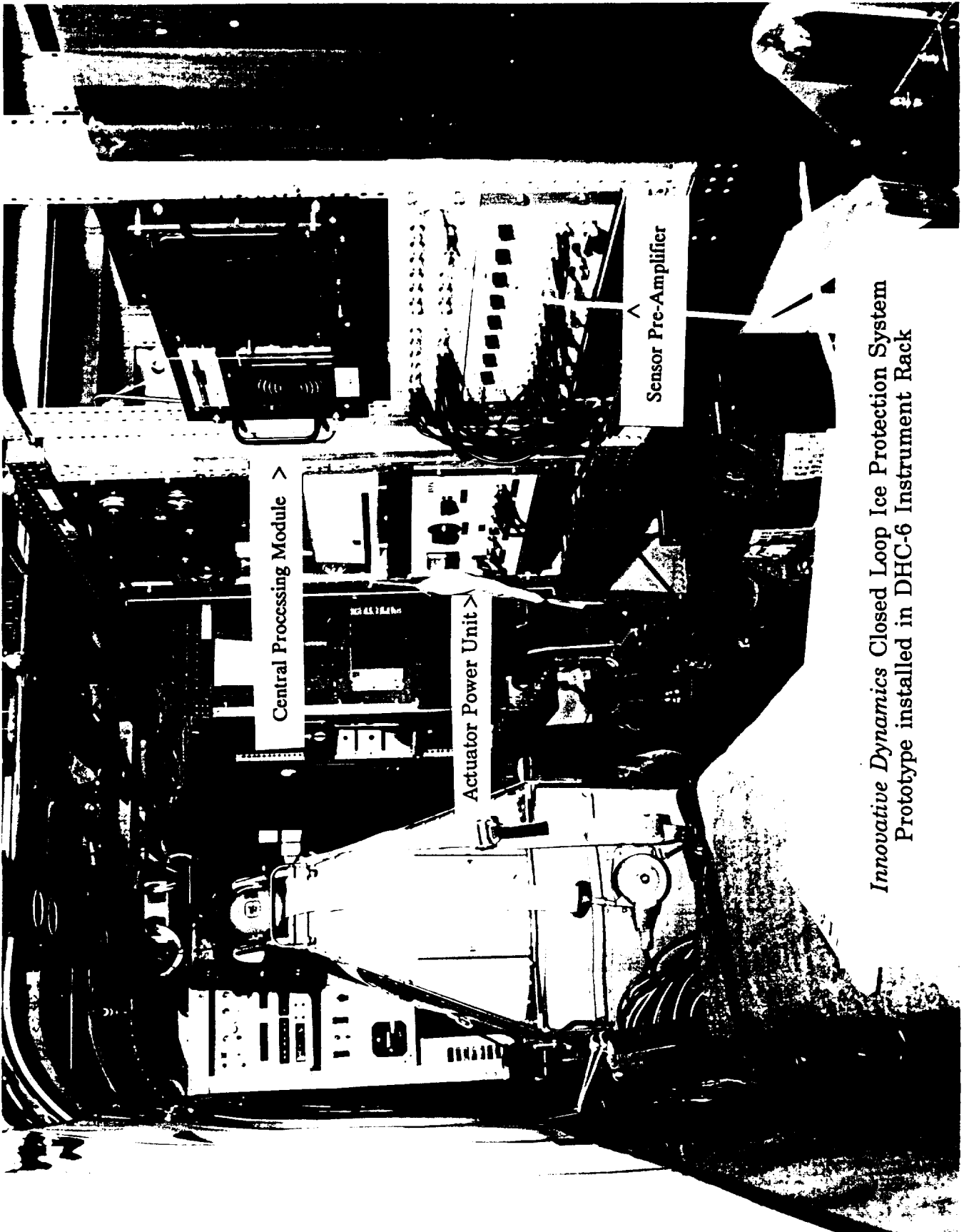


"Smart Structure" Leading Edge Wing Section (Black) installed in
NASA Lewis Icing Wind Tunnel (February 1990)



*Innovative Dynamics' "Smart Structure" Wing Cuff installed over
Conventional Pneumatic De-icing Boot on NASA's DHC-6 Icing Research Aircraft*

PHOTO 3



*Innovative Dynamics Closed Loop Ice Protection System
Prototype installed in DHC-6 Instrument Rack*

2 ISIPS SYSTEM DESCRIPTION

2.1 System Operation

The Icing Sensor & Ice Protection System (ISIPS) developed during the Phase II program combines electro-impulse deicing with piezoelectric ice accretion sensors to produce a fully automatic deicing system. Ice thickness is determined by mechanically exciting the aircraft structure with EIDI eddy-coils, and monitoring changes in the structural vibration response due to the mass of the accreted ice. The system is trained to recognize the vibration "signature" generated for a range of ice thicknesses. Pattern recognition techniques are used to classify the sensor signals and determine ice thickness.

A diagram of the ISIPS hardware configuration is shown in Figure 1. A 50 inch long wing cuff and an instrument rack contain the ISIPS equipment. The wing cuff has four bays, each of which contains a "band-aid" mount EIDI eddy-coil actuator. Two of the bays contain piezoelectric sensors. A temperature sensor is mounted in one of the remaining bays. The instrument rack contains a Digital Signal Processor (DSP), a signal conditioner, and a High Voltage (HV) power supply.

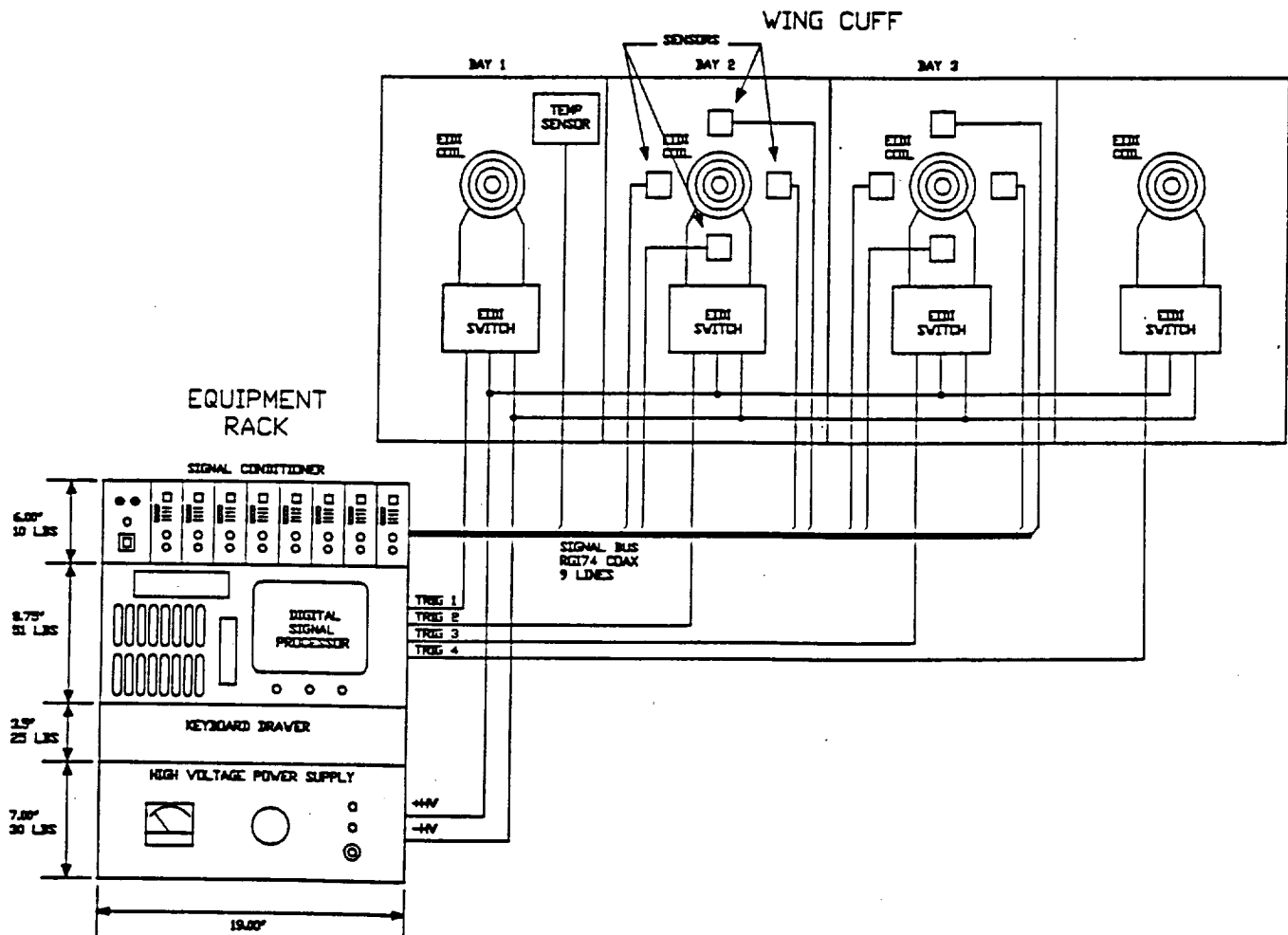


Figure 1. ISIPS hardware configuration.

The eddy-coils are mounted next to the inside surface of the metal skin at the bottom of the leading edge. When a pulse of current is sent through the coil, eddy currents are induced in the skin of the leading edge. The eddy currents produce a magnetic field that reacts with the magnetic field of the coil, creating a repelling force between the eddy-coil and the metal skin. The skin is deflected, mechanically exciting the leading edge.

Two distinct operations are performed by the ISIPS system: ice thickness measurement and deicing. During a measurement cycle the eddy-coil is pulsed with a relatively low voltage. Low voltage is used to minimize both system power consumption and mechanical stresses on the aircraft. If ice thickness exceeds a predetermined level, a deicing cycle is initiated. A much higher voltage is used to pulse the eddy-coils, resulting in the debonding and removal of the ice. The ISIPS system monitors ice thickness continually and performs deicing cycles only when necessary.

An ice thickness measurement is initiated by the DSP at intervals determined by an internal clock. The DSP sets the HV supply to its lower setting, then triggers the eddy-coils. The resulting mechanical excitation of the aircraft structure is detected by the sensors. The sensors detect changes in the structure due to ice buildup. Key pattern features of the sensor signals along with the average measured ice thickness are displayed on the CRT on-line. In addition, the time and frequency signals for each sensor can be monitored.

Once the critical ice thickness is detected, a deice signal flashes on the screen and the system goes into the automatic deicing mode to remove the ice buildup. The DSP sets the HV supply to maximum, then triggers the eddy-coils. This is repeated until all the ice has been removed. The DSP then resumes the normal measurement cycle. The DSP also sets the gain of the signal conditioners to an appropriate level during the measurement cycle. The gain varies due to differences in sensor sensitivity and position.

2.2 Hardware Configuration

Figure 2 is a block diagram of the ISIPS system. Each component is described briefly in this section. Section 3 contains more detailed circuit descriptions.

EIDI Coils. The EIDI eddy-coils convert electrical energy into mechanical energy. When a high current capacitive discharge pulse is fed into an eddy-coil it repels any conductive material in its vicinity. This results in a mechanical impulse excitation of the aircraft structure.

Ice Accretion Sensors. The sensors are made of a piezoelectric polymer film. They detect the mechanical excitation of the aircraft structure induced by the eddy-coils. The ice accretion sensors measure dynamic strain and detect changes in the signals caused by any ice build-up on the structure.

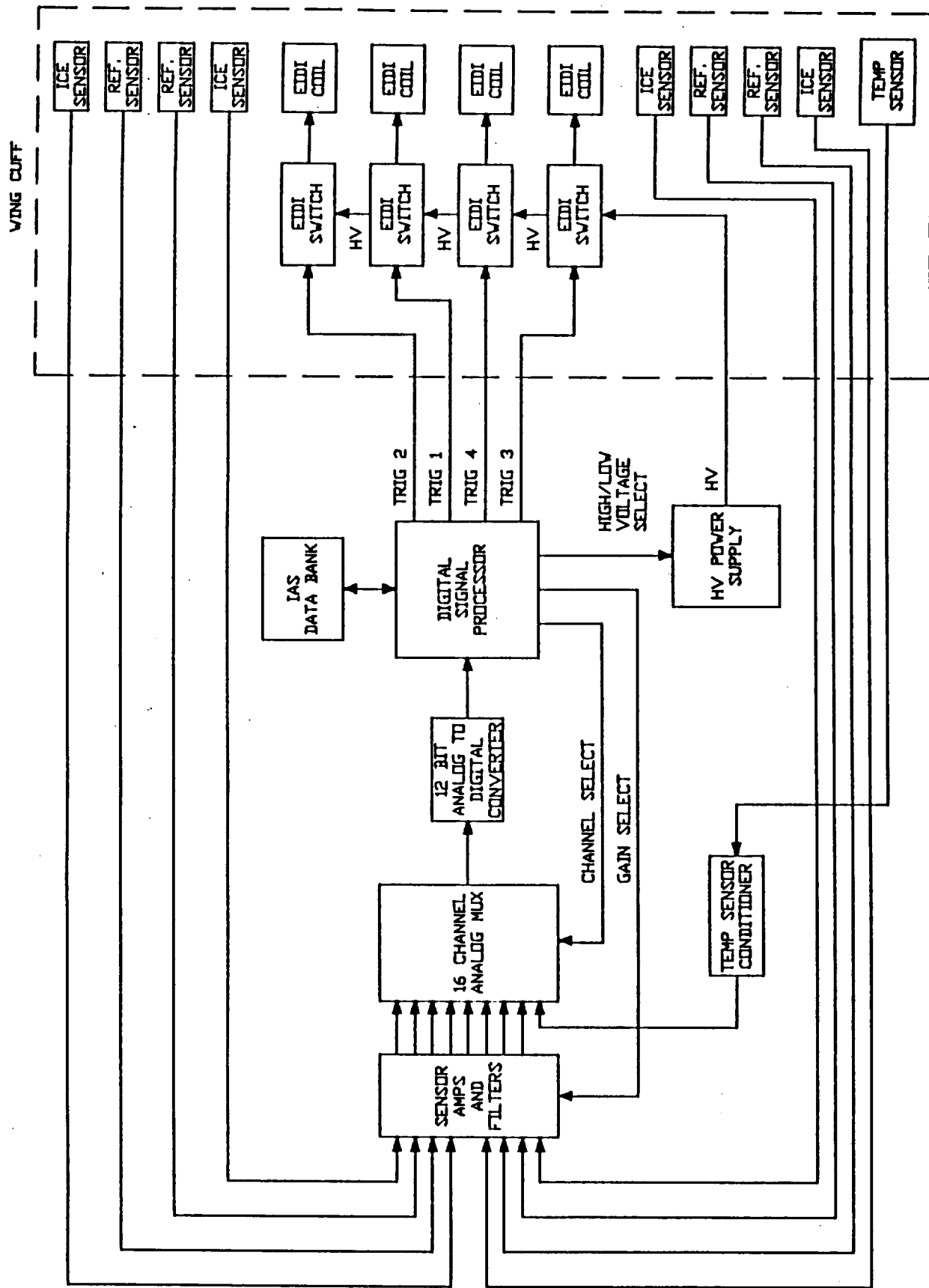


Figure 2. Block diagram of the ISIPS system.

Digital Signal Processor (DSP). The DSP performs all data analysis and control functions. It receives the digitized sensor signals from the analog to digital converter. The DSP has digital outputs which control the EIDI coil, trigger, coil voltage level, and the signal conditioner, and the analog multiplexer. A 9 inch CRT display is built into the DSP chassis to allow monitoring of system status. The IAS data bank contains the cumulative "wisdom" of the system's experience under differing conditions and it allows the DSP to correctly determine ice thickness and to take appropriate action.

Analog to Digital Converter (ADC). The ADC converts the amplified and conditioned signals from the sensors into 12 bit digital data.

Analog Multiplexer (MUX). The MUX selects one of 16 sensor signals and feeds it to the ADC. Channel selection is controlled by the DSP.

Signal Conditioner. The signal conditioner amplifies the sensor signals and filters out unwanted noise. The gain of the signal conditioner is controlled by the DSP.

High Voltage (HV) Supply. The HV supply contains a charger and a capacitor bank which provides the power for the EIDI coils. Two output voltage levels are available, one for sensing ice accretion, and the other for deicing. The DSP selects the voltage level.

EIDI Switch. Each EIDI switch is an electronic switch which rapidly connects the EIDI coil to the capacitor bank in the HV supply, discharging the stored energy into the EIDI coil. The switch is triggered by the DSP. The EIDI switches are mounted in the wing cuff adjacent to the eddy-coils.

Temperature Sensor and Conditioner. A thermocouple is used to sense the temperature of the leading edge. This allows the DSP to compensate for temperature dependent changes in the dynamics of the structure. The thermocouple signal is amplified by the conditioner and then sent to the DSP.

3 ELECTRONIC DESIGN

3.1 System Components

3.1.1 EIDI Coils

The band-aid mount EIDI eddy-coils were fabricated by Wichita State University. The eddy-coils are 40 turns of 0.140 by 0.02 inch copper ribbon wire, sealed in reinforced epoxy and polyurethane. Coil diameter is 2.1 inches. The total size of the coil and its mounting is 6.3 by 2.5 by .5 inches. A doubler made of 1100 aluminum, 2.5 by 2.5 by .05 inches, is bonded to the skin directly under the coil. Construction details of an EIDI coil are shown in Figure 3, and a typical installation in Figure 4. EIDI coils were wired in pairs to significantly reduce weight of HV wiring and firing circuitry. Deicing voltage levels are increased accordingly (to 1100 V for IRT test) when operating eddy coils in series.

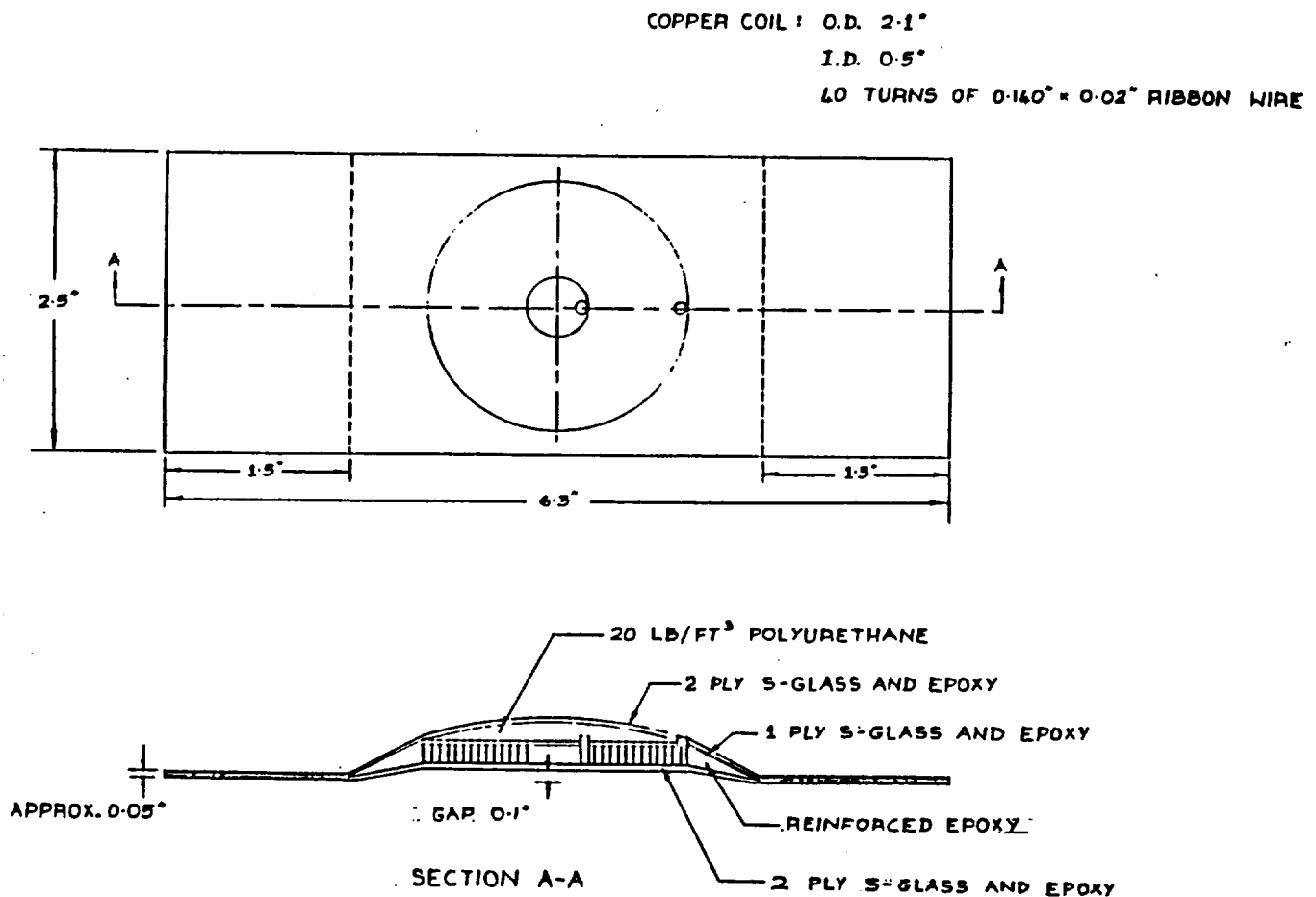


Figure 3. "Band-Aid" Mount EIDI Coil

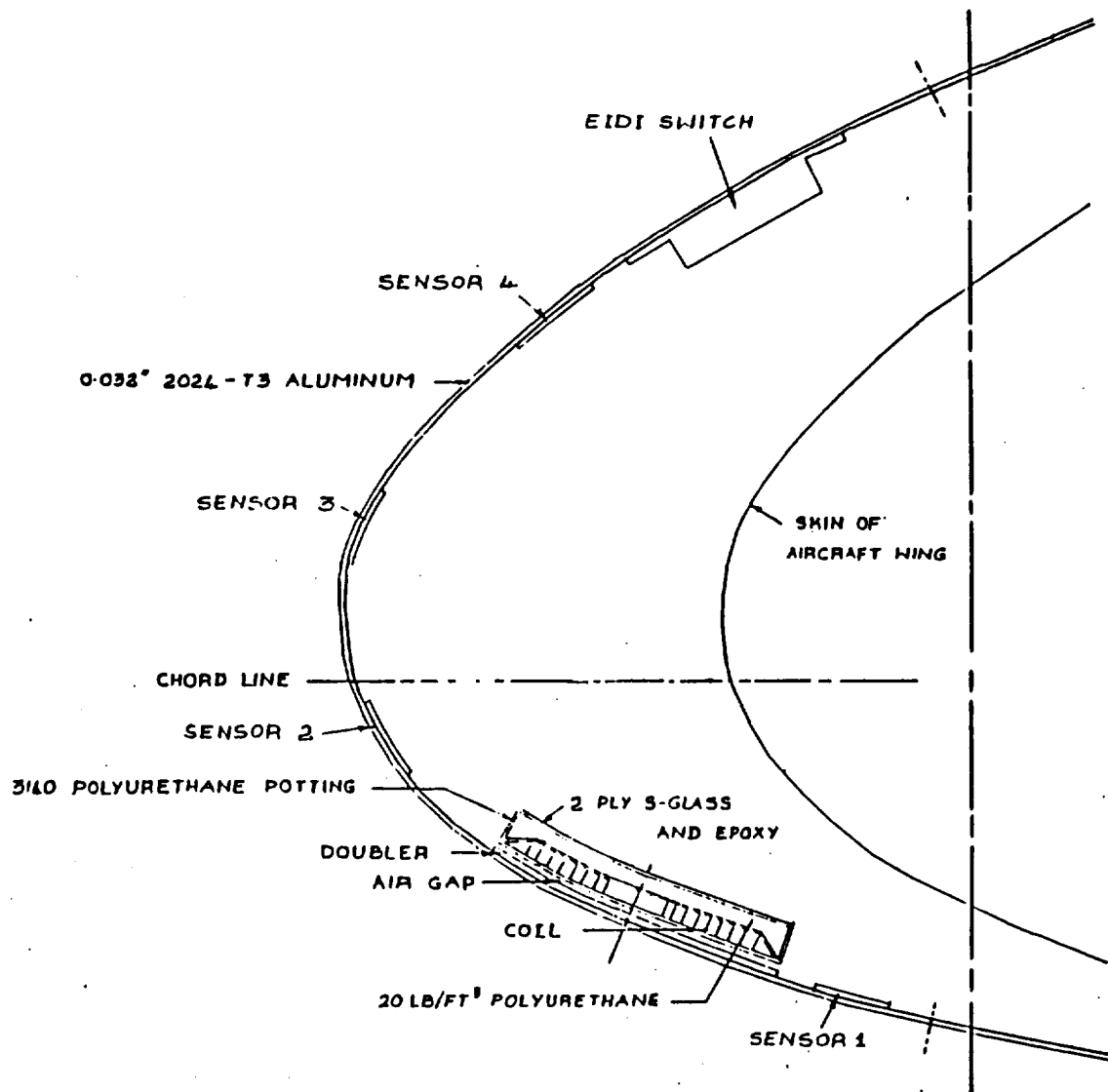


Figure 4. EIDI Coil Installation.

3.1.2 Ice Accretion Sensors

The ice accretion sensors were made from a piezoelectric polymer, polyvinylidene fluoride (PVDF) manufactured by Penwalt Corp, Valley Forge PA. The film is 28 micrometers thick and varies in size from 2" x 2" to 2" x 10.5". The sensors were bonded to the skin with epoxy and protectively sealed with urethane. Electrical contacts are made to the conductive plating on both sides of the PVDF using conductive silver epoxy.

3.1.3 Digital Signal Processor Hardware

The Digital Signal Processor (DSP) is a Recortec model RME194/286 (Recortec Inc.,

Sunnyvale CA). It contains an Intel 80286 microprocessor for general operations and an Intel 80287 math coprocessor for computation intensive work. The DSP has a 20 megabyte hard disk for program storage, as well as a 5.25 inch IBM compatible floppy disk. A 9 inch monochrome monitor is built into the DSP chassis. The DSP fits in a standard 19 inch equipment rack and is 20.2 inches deep and 8.75 inches tall. Weight is 51 pounds.

3.1.4 Analog to Digital Converter and Analog Multiplexer

Both the Analog to Digital Converter (ADC) and the Analog Multiplexer (MUX) are located on a Metrabyte (Marlboro MA) model Dash-16F card that plugs into the DSP backplane. The ADC and Mux receive their power from the RME194 power bus. Two DG508's select one of 16 analog inputs. The selected input is buffered and then converted to a 12 bit digital output by a Harris HA-774 analog to digital converter at a maximum sample rate of 100KHz.

3.1.5 Signal Conditioner

The signal conditioner was designed at ID. There are 8 identical channels in the signal conditioner, each with remotely selectable gains of 1, 10, 100, and 200. A jumper programmable low pass filter may be set to 1 kHz, 10Khz, or full bandwidth.

The schematic of one of the eight amplifier channels and its control circuitry is shown in Figure 5. The 2N2222's, Q6 through Q9, act as input protection diodes. The gain stage is an AMP-01 differential instrumentation amplifier with its gain selected by the JFETS Q1 through Q5. U7, an LF411, bootstraps the gates of Q1 through Q5 to reduce distortion. The amplified signal then goes to U8, another LF411 that is an active filter and output driver. U14 is a LM311 comparator and it provides an adjustable trigger pulse to the analog to digital converter. The remaining digital logic allows for either manual or automatic gain setting by the DSP. The eight signal conditioner channels and their support circuitry are contained in a 19 inch rack mounted chassis that is 6" tall and weighs 10 pounds.

Figure 6 is a schematic of the power supply for the signal conditioner. Input power is 120 Volts at 1 Amp. The LM317, LM301, and LM337 form a tracking positive and negative 15 volt power supply. Overvoltage protection is provided by SCR crowbar circuits. X10 is a positive 5 volt regulator for the digital logic.

3.1.6 High Voltage Power Supply

The schematic of the High Voltage (HV) Supply designed at ID is shown in Figure 7. T1 is a variable transformer (variac) which is used to set the low voltage level. The high

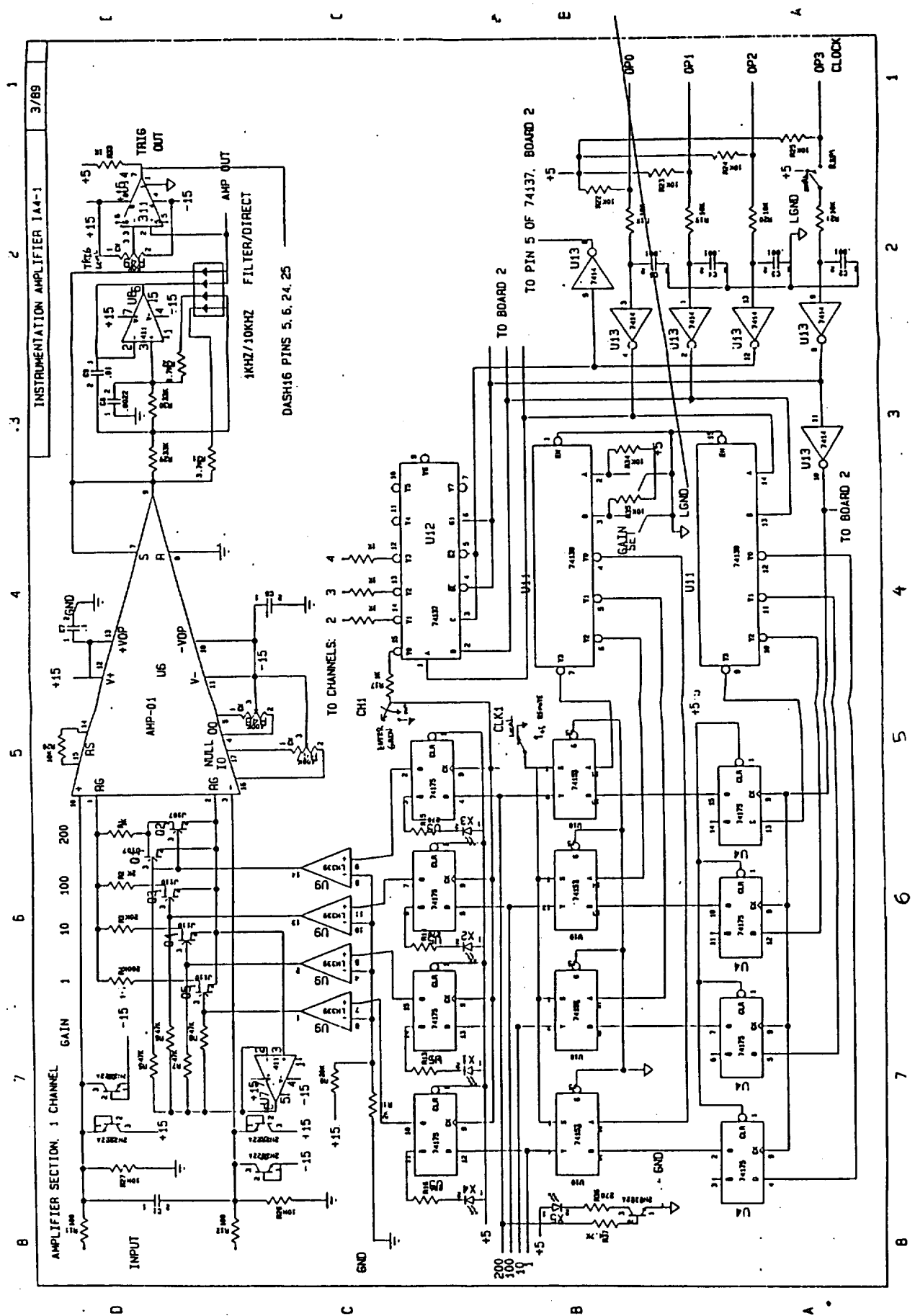


Figure 5. Schematic of Signal Conditioner

voltage deicing level is set by a stepping switch to select desired turn ratio of transformer T2 to provide 700, 800, 900, 1000, 1100 volts for deicing coils. K1 is a relay which selects the output voltage from either T1 or T2. D1 protects the DSP driver that controls K1. A bridge rectifier converts the AC into DC to charge the capacitor bank. C1 to C5 are the energy storage capacitors. R1 is the charging resistor and R2 is a bleeder resistor.

The energy storage capacity of the HV supply is $\frac{1}{2}CV^2$, where C is the total capacitance of the capacitor bank and V is the voltage to which the capacitor bank is charged. With a total capacitance of 400 μ F and a voltage of 800 V, the stored energy is 128 Joules.

The HV supply design is limited to 1100 V. The HV bleeder resistor has an RC time constant of 20 sec and discharges the capacitors to 50 V in one minute. An HV meter on the box displays the voltage across the capacitors. A cover is installed over the high/low switch to prevent accidentally selecting high voltage.

The HV supply box is 20 inches deep, 7 inches tall, and fits in a standard 19 inch equipment rack. Weight is 30 pounds.

3.1.7 EIDI Switch

Each EIDI switch unit is a high current/high voltage switch to discharge the HV supply capacitor bank into the EIDI coil. Figure 8 is the schematic of the EIDI switch. Q2 is an SCR that acts as the switch. D3 is a clamp diode that protects Q2. R5 is a current sensing resistor to allow monitoring of the EIDI coil current. The rest of the circuit is the trigger for Q2. R2, D2, and C1 form a simple 12 volt power supply. U1 optically isolates the trigger pulse from the DSP. When U1 conducts, Q1 receives base current and turns on. C1 is discharged into the gate of Q2. Q2 fires, discharging the capacitor bank into the EIDI coil.

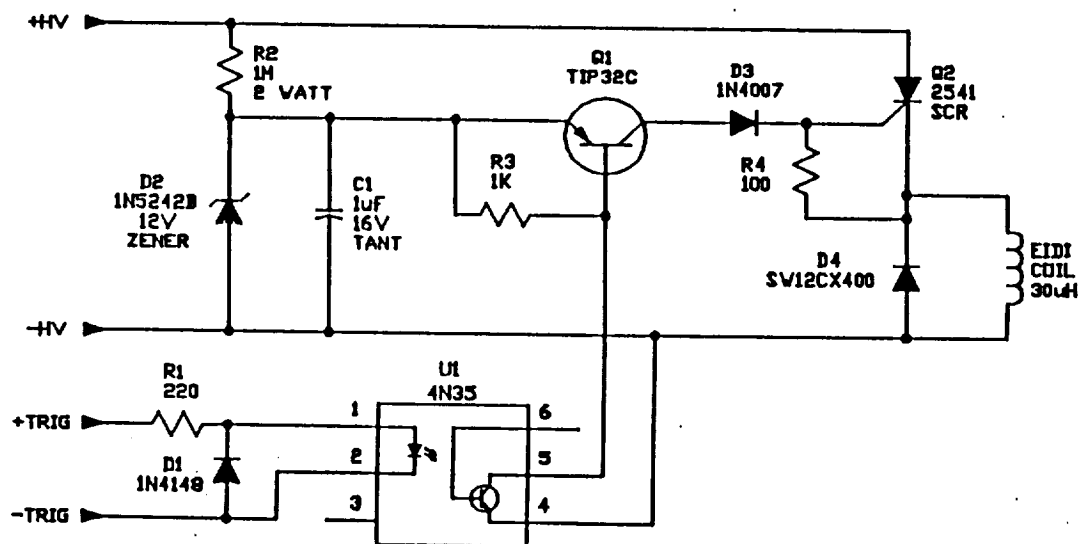


Figure 8. EIDI Switch

3.1.8 Temperature Sensor and Conditioner

A type K thermocouple is used to sense the temperature of the aircraft's leading edge. The thermocouple is mounted on an insulated pad 3/8" by 3/4". The pad is glued on the leading edge interior with epoxy. An Omega Model TX-52 thermocouple signal conditioner amplifies and linearizes the signal, as well as providing electrical isolation between the thermocouple and the other circuitry. The temperature conditioner is mounted within the signal conditioner chassis.

3.2 Wiring Specifications

Figure 9 is a wiring diagram of the instrumentation/cuff interface. The wire specifications are given below.

1) High Voltage line from equipment rack to wing cuff:

Wires - three 14 gauge (standard AN) stranded twisted pairs in a shielded cable, 3000 volt insulation. The 3 twisted pairs are braided together along their entire length. Max load is 1200 V at 2000 Amps peak.

Connectors - #10 eye terminals, crimped and soldered. Connectors are covered with a non-conductive shield.

2) EIDI coil lines from EIDI switch to coil:

Wires - 14 gauge stranded twisted pair, 3000 volt insulation. Minimal signal levels through the wires.

Connectors - #10 eye terminals, crimped and soldered. Connectors are covered with a non-conductive shield.

3) HV trigger and temp sensor lines from equipment rack to wing cuff:

Wires - 3 RG-58 A/U coaxial cables. Maximum load is 24 V at 14 Amp peak.

Connectors - BNC fittings at both ends.

4) Sensor lines from equipment rack to wing cuff:

Wires - 8 RG-174 coaxial cables, 1/8" diameter. Minimal signal level through cables.

Connectors - BNC fittings at both ends.

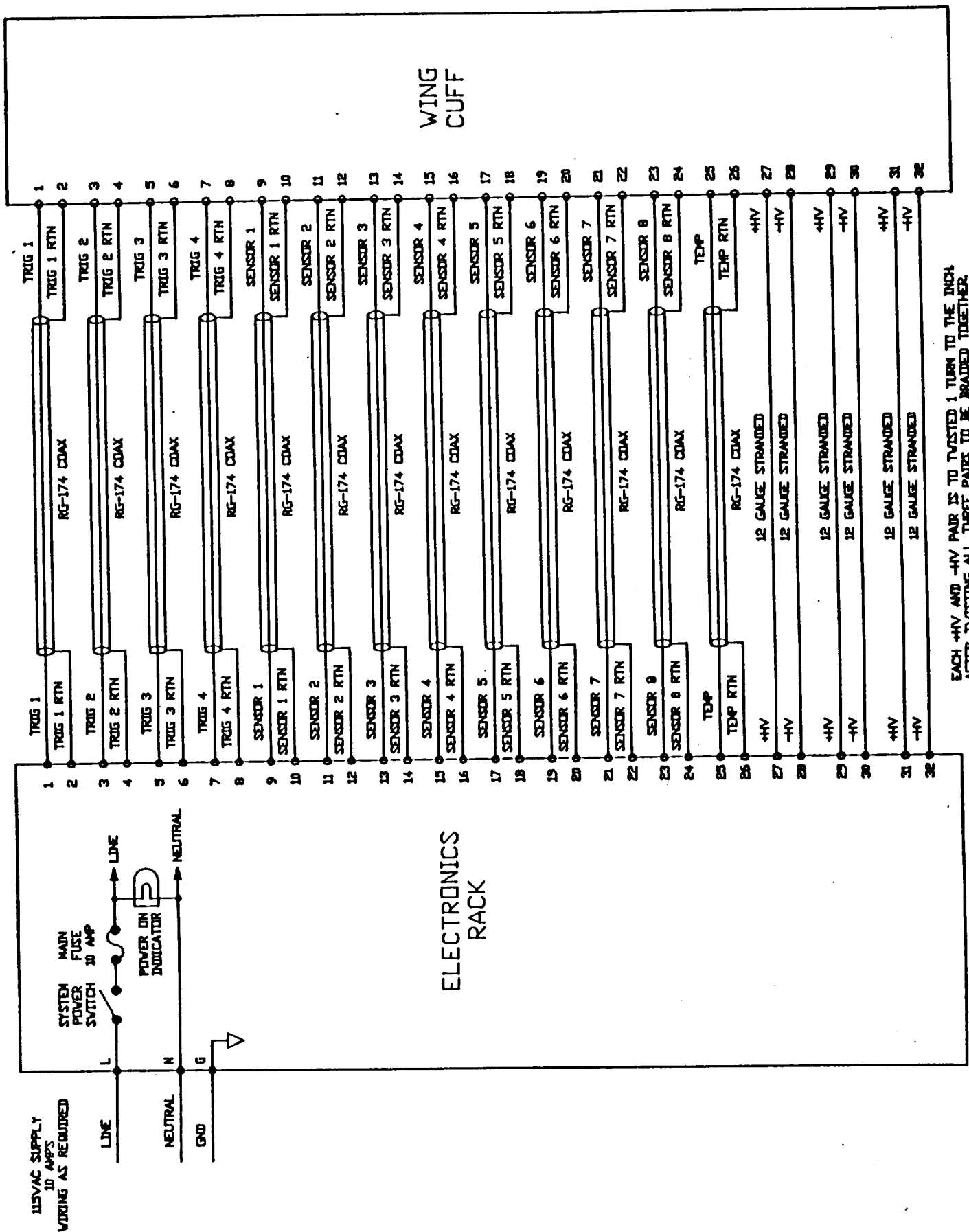


Figure 9. Wiring Diagram of the ISIPS System

3.3 Power Specifications

Power consumption of the EIDI high voltage power supply can be broken into two (2) parts, static and dynamic. Static is the normal power consumption when the HV supply is not being pulsed. Dynamic is the additional power used when the HV supply is pulsed.

a) Static Power Consumption

Static power consumption is $50 + (HV^2/50,000)$ watts, where HV is the high voltage the supply is set to.

b) Dynamic Power Consumption

Dynamic power consumption (300 uF capacitance bank) may be computed using the following formula:

$$\text{Power} = \frac{0.5 (3 \times 10^{-4} \text{ Watt-Sec/HV}^2) \text{ HV}^2}{\text{Time between pulses (Sec)}}$$

where:

$$\text{Power} = \text{Joules/Second} = 1/2 \text{ cV}^2/\text{sec}$$

c) Examples

$$\text{HV} = 1000 \text{ volts}$$

$$\text{Time} = 1 \text{ second between firing pulses.}$$

$$\text{Static Power} = 50 + \frac{(1 \times 10^6)}{50,000} = 70 \text{ Watts}$$

$$\text{Dynamic Power} = \frac{(3 \times 10^{-4}) \times (1 \times 10^3)^2}{2} = 150 \text{ Watts}$$

$$\text{Total Power Requirements} = 220 \text{ Watts}$$

The total power requirements of the ISIPS system is shown below:

Equipment	Average Power	Max Current
Signal Amplifier (120 V @ 500 mA)	60 Watts	0.5 Amps
Recortec Computer (120 V @ 2.0 Amp)	240 Watts	2.0 Amps
HV Power Supply (120 V @ 1.85 Amp) (1 KV, 1 sec charge/fire cycle)	220 Watts	4.0 Amps*
Total load:	520 Watts (Avg)	6.5 Amps(Max)

* Note: Line filter/surge protector required on grid to reduce power glitches caused by rapid HV charge/discharge spikes.

4 MECHANICAL DESIGN

4.1 Wing Cuff Mechanical Design

A 50 inch long cuff with EIDI eddy-coils was constructed for placement on the starboard wing of the Twin Otter IRA. The cuff has four 12.5 inch bays between five ribs. This cuff is very similar to one built by Wichita State University for tests performed during the 1983-1984 icing season where they demonstrated the deicing performance of the EIDI system. The previous cuff was built with the expectation of use for only a few flights, but has been successfully used for many flights over the past five years. The cuff was constructed with a leading edge shape identical to that of the Twin Otter wing. It is designed to fit over the aircraft wing, three inches forward of the original leading edge, with no changes to the aircraft wing except for the insertion of the screw fittings at the upper and lower rear edges of the cuff. Since the Twin Otter has de-icing boots installed, the cuff was made to be cantilevered for the forward 4 inches of chord. This leaves a 3/8 inch space at all points for the expansion of the boot. The cuff's inner surface was filled with rigid foam up to this forward section to enable a snug fit against the wing surface, transferring pressure (lifting) loads to the base wing surface. A spare wing was used in fitting the cuff.

Figures 10a and b show the wing cuff design. The top surface of the cuff is made of 0.032" 2024-T3 aluminum skin and the bottom surface is made of 0.040" 2024-T3 aluminum. A lap joint was made on both the top and bottom surfaces as indicated in the figures. The top and bottom surfaces are supported by four (4) ribs which are 1 inch wide and made from 40 lb polyurethane. The space in between the ribs is filled with 20 lb polyurethane. An epoxy bond primer is used on the inner surface of the aluminum to provide structural bond and corrosion protection. The polyurethane on the top and bottom surface of the cuff is covered with 0.020 inch and 0.010 inch thick layer of S-Glass epoxy, respectively.

The leading edge (nose) of the cuff is removable, being attached by AN509 #8 screws equally spaced every 0.89 inch rather than rivets. The leading edge of the cuff is made of 0.032" 2024-T3 aluminum and is supported by five (5) ribs made of 0.040" 2024-T4 aluminum spaced 12.5 inches apart. The aluminum skin is attached to the ribs by AN509 #8 screws and NAS 683 nutplates spaced every 0.95 inches. The inside surface of the leading edge and the ribs are corrosion primed and painted with a polyurethane paint.

Each end of the cuff is supported by a fence made of 0.100 inch aluminum. Each fence is attached to the cuff with seven (7) AN509 #8 screws.

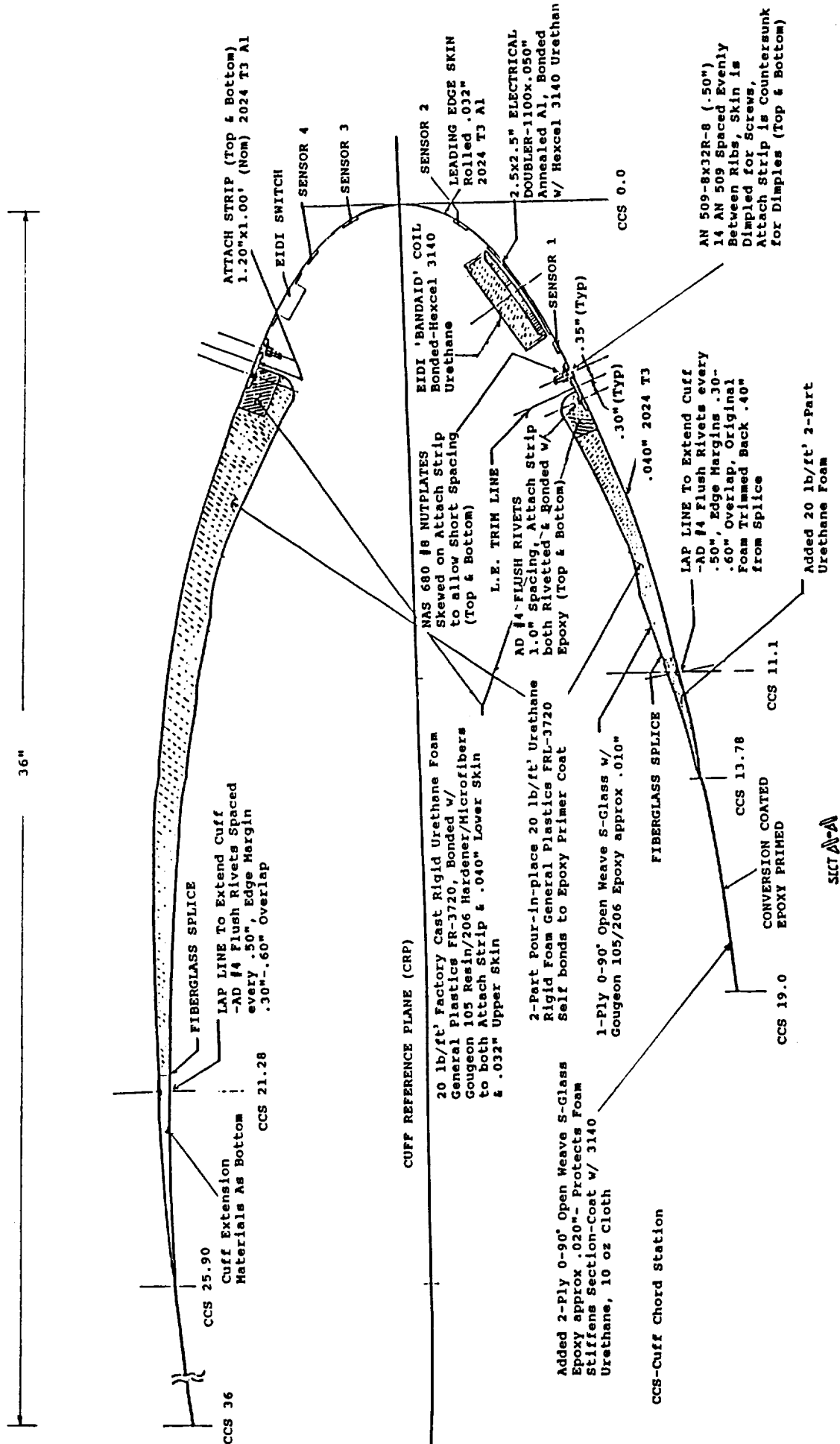


Figure 10a. Wing cuff cross-sectional view.

NOT TO SCALE

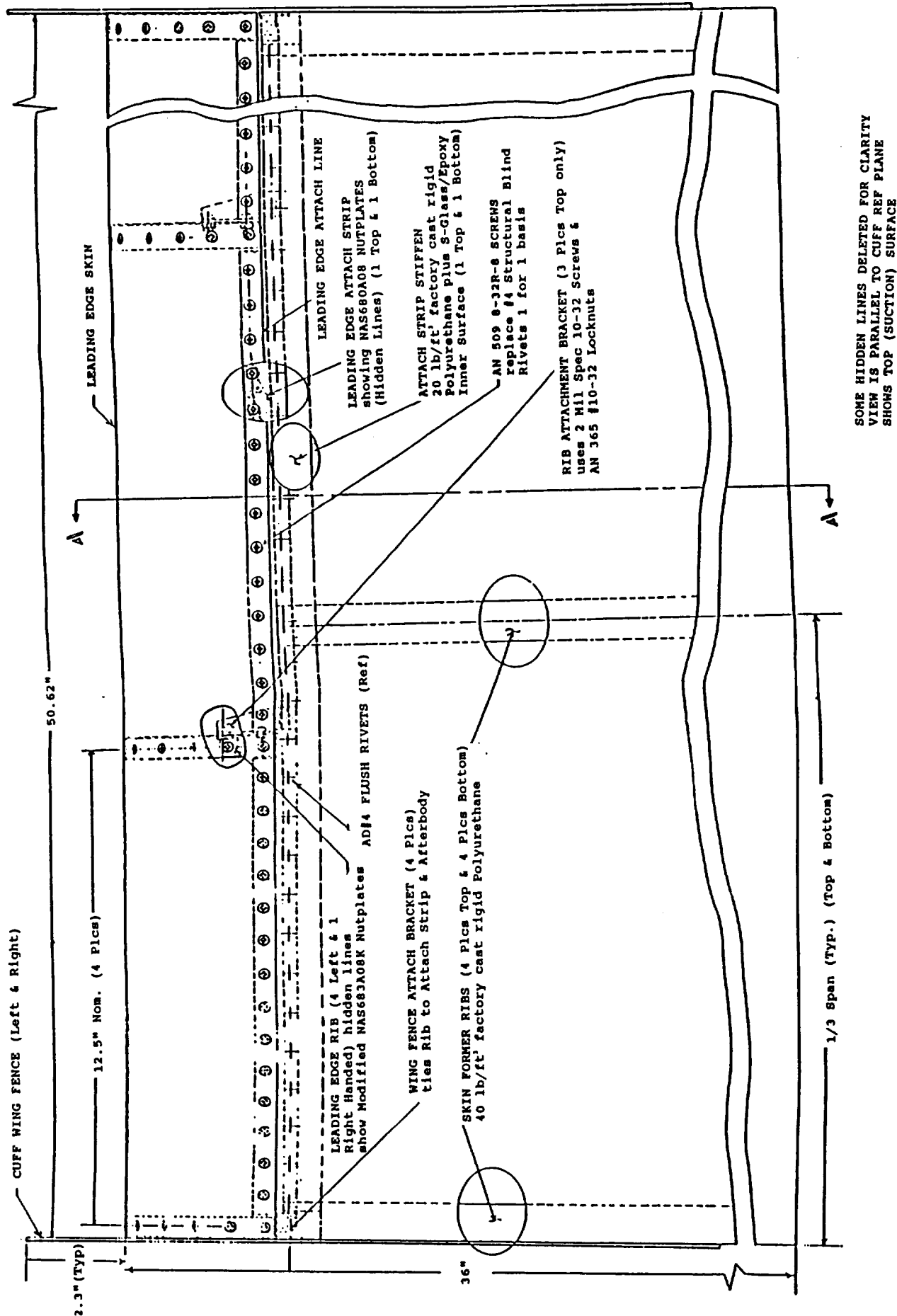


Figure 10b. Wing cuff spanwise view.

4.2 Wing Cuff Structural Analysis

A potential flow computation program was run for the original Twin Otter wing cuff built by WSU for tests in the Icing Research Tunnel and on the Twin Otter during 1983-84. The basic wing chord was 78 inches, and the augmented wing chord 81 inches. Typical pressure distributions are shown in Figure 11. Lift and pitch moment coefficients are shown in Figure 12. If sea level flight at 180 mph is used as an example, the computed pressure loads are shown in Table 4.

Figure 13 illustrates the normal forces computed for the cuff alone and for the cantilevered portion of the cuff. These are for the maximum flight speed at 8° angle of attack. The centers of lift are shown and values of lift forces per foot of span given. It should be noted that, for all cases computed, the lift center for the cuff lies in the foamed region. The forces are thus transferred to the skin and ribs of the base wing, with only minor forces transmitted to the screw fasteners.

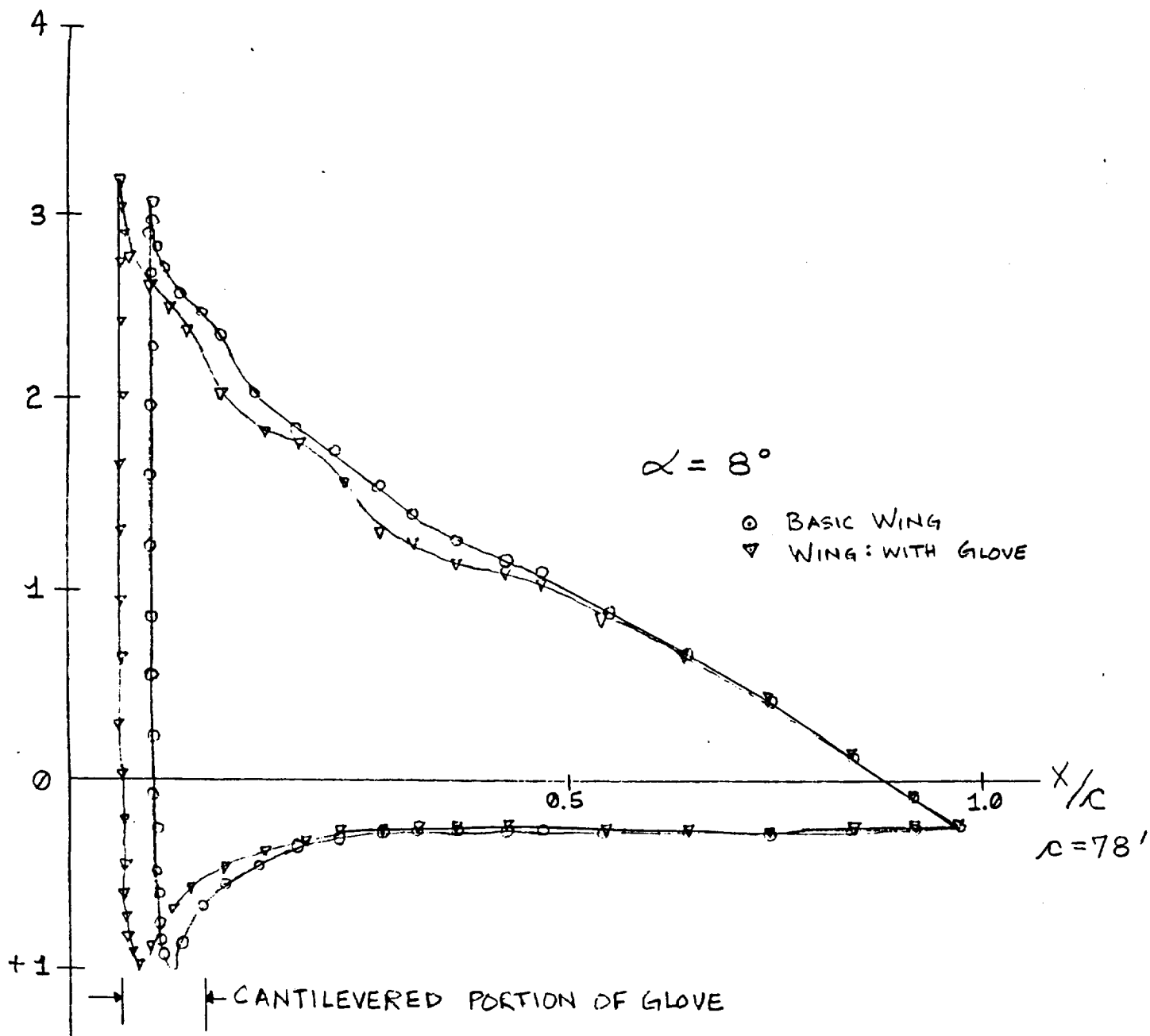


Figure 11. Pressure distributions predicted by potential flow computations for the Twin Otter airfoil with and without the EIDI cuff.

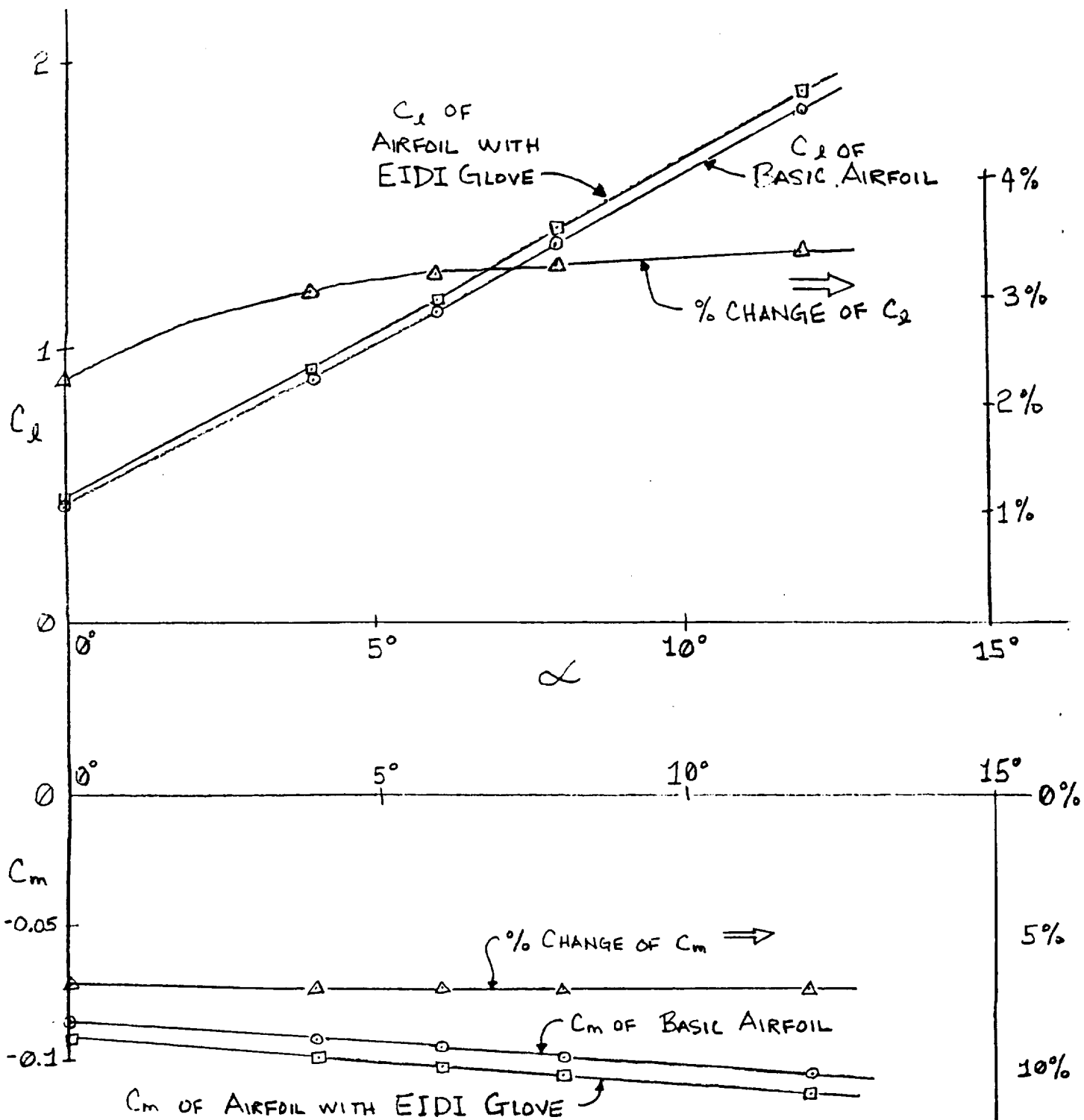


Figure 12. Effect of adding the EIDI wing cuff to the airfoil of the DHC-6 Twin Otter.

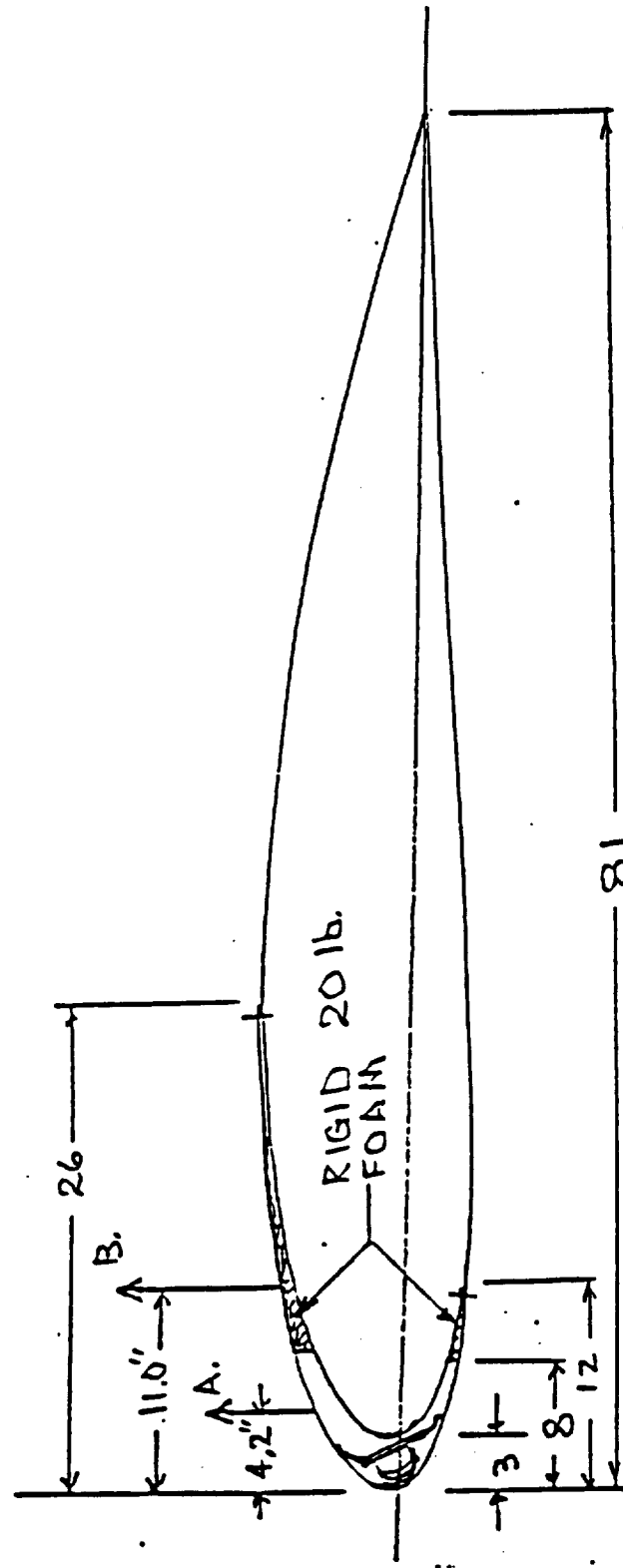


Figure 13. Values integrated from potential flow computations ($\alpha = 8^\circ$, IAS = 105 mph).

TABLE 4. Computed airfoil pressure lifting loads (180 mph, std. sea level atmosphere).

		<u>Original Wing</u>	<u>Cuffed Wing</u>
Airfoil Lift per Foot of Span	0°	229.3 lb	234.4 lb
	4°	286.5	501.2
	6°	614.3	633.8
	8°	741.4	765.6
	12°	992.7	1026.3
Added Lift for the 50 inch Cuff	0°		21.1 lb
	4°		61.2
	6°		81.1
	8°		100.8
	12°		140.0
Pitch Moment per Foot of Span	0°	-301.4ft-lb	-323.1 ft-lb
	4°	-318.4	-341.0
	6°	-327.1	-350.8
	8°	-336.8	-361.0
	12°	-357.2	-382.5
Center of Lift Locations from Leading Edge	0°	35.7 inches	37.2 inches
	4°	27.7	28.7
	6°	26.2	27.2
	8°	25.3	26.2
	12°	24.1	25.0
		Elastic Axis is at 27.6 in.	Elastic Axis is at 30.6 in.

5 PATTERN RECOGNITION SOFTWARE

5.1 Description

Pattern recognition software developed at ID is used to monitor changes in the vibration response of the structure caused by the presence of ice accretion and to determine the thickness of the ice. The general pattern classification procedure is indicated diagrammatically in Figure 14. The system from which given patterns arise is characterized numerically by some set of measurements. The raw data describing the system is referred to as the measurement space; that is, a sample of a pattern is represented by specific values of all the measurements, corresponding to a point in the measurement space. Feature selection (or preprocessing) is then performed whereby a sample in the measurement space is described by a finite and usually smaller set of numbers called features which become components of the pattern space. On the basis of a finite set of labeled samples, a decision rule is used to classify a point in the pattern space corresponding to an unlabeled sample.

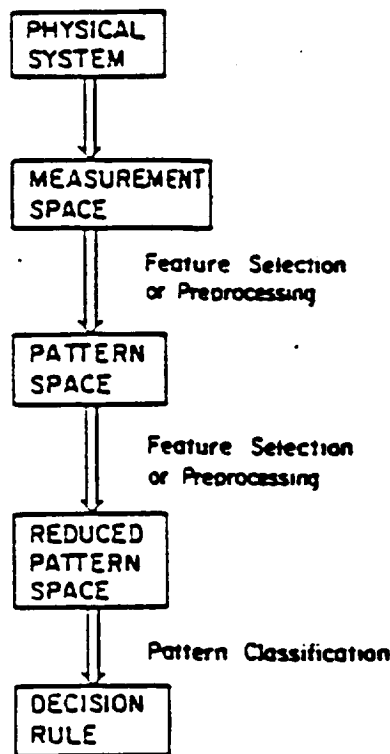


Figure 14. Stages in the pattern classification process.

The two major areas of pattern recognition which must be carefully applied with care to particular applications are feature extraction and classification. The specific approaches used here for the ice detection problem along with a description of the software code that was developed is discussed below.

5.2 Feature Extraction

A time signal or vibration waveform from the structure response usually contains too many data points to be directly stored in the computer. It is therefore necessary to convert the signal into a set of features. That feature set includes as much information as necessary to characterize the signal but usually requires much less storage than when comparing the signal itself. Let z represent the signal:

$$z = (z_1, z_2, \dots, z_n)$$

n --- Number of data points in the signal

and x represent the feature set of signal z :

$$x = (x_1, x_2, \dots, x_m)$$

m --- Number of features of the signal.

The characteristics or features of each signal are determined by mapping z to x :

$$x = f(z)$$

where x can be used to represent z . The dimension of x is usually, however, much smaller than that of z .

After the features are extracted from the signals, they must be normalized in order to reduce scaling and dimensional effects. The normalization of a feature is:

$$X_{ij} = \{ (x_{ij} - x_{i\bar{a}}) / S_{xi} \}$$

Where: $x_{i\bar{a}}$ --- Mean value of x_i in Class i ,
 S_{xi} --- Standard deviation of x_i in Class i ,
 x_{ij} --- Feature j in Class i .

A good feature set should characterize the signal or waveform. It should also be able to distinguish changes of the signal due to changes of the structural properties caused by the presence of ice accretion of the structure. Twenty-six features have been identified as the primary pattern space for ice discrimination as indicated in Table 5. These features can be

classified into the following four categories:

- a. Time domain
- b. Frequency domain
- c. General properties and shape factors
- d. Transfer Function

TABLE 5. Features Extracted From Piezoelectric Sensor Signals

Feature	Description
1	1st local damping
2	2nd local damping
3	3rd local damping
4	4th local damping
5	5th local damping
6	6th local damping
7	7th local damping
8	8th local damping
9	one half of the modulation signal period
10	standard deviation of signal
11	kurtosis of signal
12	skewness of signal
13	time at 90% decay
14	amplitude ratio of two biggest peak values
15	frequency of the biggest peak value
16	frequency difference of two biggest peaks
17	partial power in frequency band 0.700 - 1.15 kHz
18	partial power in frequency band 1.15 - 1.8 kHz
19	partial power in frequency band 1.8 - 3.0 kHz
20	ratio of smallest & largest partial power
21	number of peaks exceeding a given threshold
22	frequency at which 25% of accumulated power was observed
23	frequency at which 50% of accumulated power was observed
24	frequency at which 75% of accumulated power was observed
25	transfer function 1 - ratio of partial power in frequency band 0.700 - 1.15 kHz
26	transfer function 2 - ratio of partial power in frequency band 1.15 - 1.8 kHz

5.2.1 Time Domain

Figure 15a is a typical time trace of the vibration response of the wing cuff detected with the piezoelectric sensors for several ice thickness measurements acquired during training in the IRT. Ten features in the time domain have been identified based on these types of signals. Eight of them are so called local damping. The ninth is one half of the demodulation period. The tenth feature is the time at which the magnitude of the signal decays by 90%.

It is interesting to note that the 0.25 inch ice trace is more similar to the 0.5 inch ice case than to the signal with no ice. The main reason of this phenomenon is that the stiffness of the structure changes rapidly when the ice initially starts building up. When the ice increases to a certain level, it does not affect the stiffness of the structure as much as it used to. It can, therefore, be predicted that the thicker the ice is on the structure, the more difficult it will be to distinguish the ice thickness.

- (1) The eight local damping numbers are defined as:

$$\delta_i = \ln(P_i / P_{i+1}) \quad i = 1, \dots, 8$$

$$\zeta_i = \frac{\delta_i}{(4\pi^2 + \delta_i^2)^{1/2}} \quad i = 1, \dots, 8$$

Where

- δ_i --- The i th logarithmic decrement, the natural logarithm of the ratio of two successive amplitudes, unitless;
- P_i --- The i th peak amplitude, Volt;
- P_{i+1} --- The $(i+1)$ th peak amplitude, Volt;
- ζ --- Damping factor, unitless.

The local damping factor is affected by both decay of the signals and modulation caused by superposition of different resonant modes of the structure. As ice accumulates on the surface of the structure surface, it becomes stiffer and the spring constant of the system increases. In general the damping of the system increases as the thickness of the ice increases. Also, the number of modes of the structure is reduced. These changes of the mechanical characteristics of the local structure can be detected by the local damping factors.

- (2) One half of the demodulation period. This feature comes from the fact that there are two distributed forces in the EIDI actuator mechanism which excites the structure. The dominant mode forms a waveform which displays the modulation. When the ice accumulates on the structure surface, actuator force distribution is changed, causing modulation of the input signal. Therefore, the demodulation period can be used to differentiate the ice thickness.

- (3) The time of 90% decay of the signal. Unlike the local damping which measures only the local variation of the signal, this parameter measures the response of the overall system. The larger the damping, the shorter the decay period will be. When the modes of the system increase, care must be taken to insure that this parameter is computed correctly.

5.2.2 Frequency Domain

The basic consideration for using the frequency domain information is that as the ice thickness changes, the frequency response of the structure will change. Figure 15b shows the power spectral density of the structure for several ice thicknesses. As seen by examining the time traces, the frequency traces also show that the signal representing 0.25 inch ice is more similar to the 0.5 inch signal than the signal without ice. Eleven features have been identified in the frequency domain.

- (1) Amplitude Ratio (Ar) is defined as the ratio of the second largest amplitude to the largest amplitude of the peak in power spectrum. This feature measures the relative changes of the two dominant modes as a function of ice thickness.

$$A_r = P_2 / P_1$$

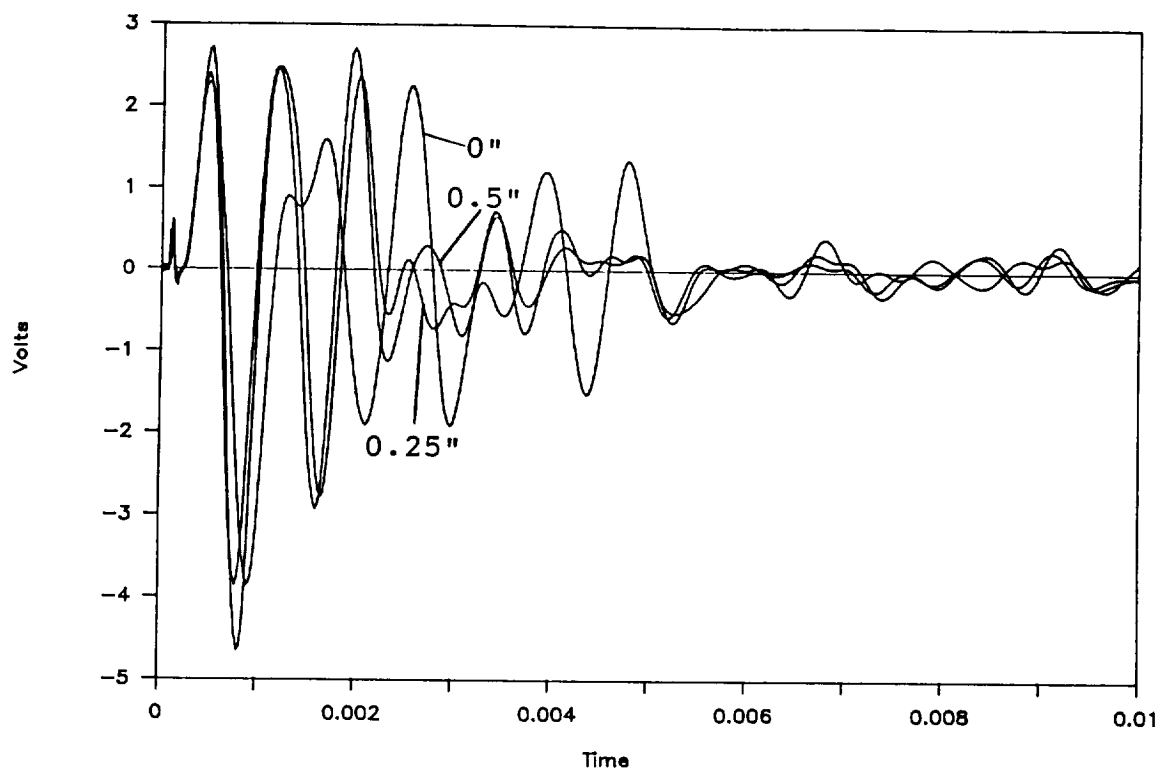
Where P_1 --- Power of the largest peak;
 P_2 --- Power of the second largest peak.

- (2) The frequency of the largest peak. This feature mainly measures the frequency shift of the dominant mode as the ice thickness changes. But when this feature is used, one must be aware that other modes may become dominant for different ice thicknesses. If that is the case, the frequency shifting concept is no longer valid because the mode having the largest peak in one case may have the smallest peak value in another case.
- (3) The frequency difference of the first and second largest peaks. This feature detects the relative frequency shift of the two most dominant modes. Caution must be taken as mentioned in Point (2).

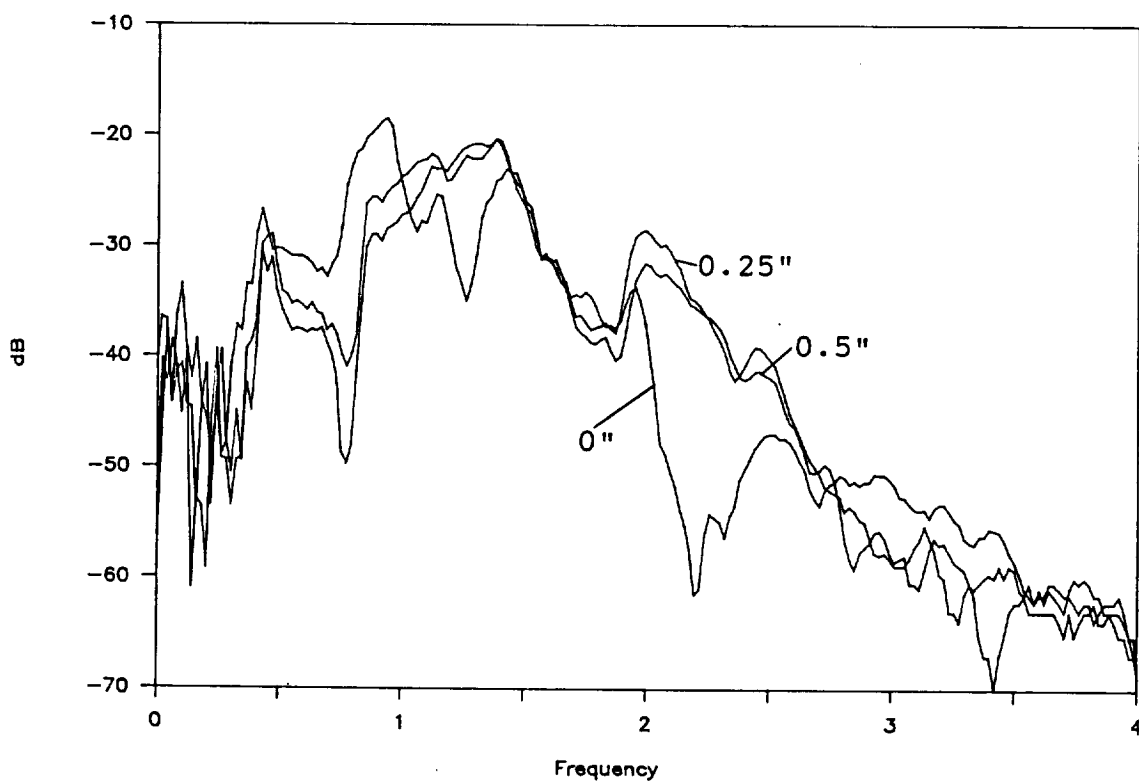
- (4) Partial energy in frequency band 0.7 -- 1.15 KHz. Partial energy from frequency f1 to f2 is defined as:

$$\Delta E = \int_{\omega_1}^{\omega_2} \frac{1}{2} \pi |F(\omega)|^2 d\omega$$

- (5) Partial energy in frequency band 1.15 -- 1.80 KHz
- (6) Partial energy in frequency band 1.80 -- 3.00 KHz



(a) Time trace.



(b) Frequency trace.

Figure 15. Typical sensor signals acquired during the IRT training for three different ice cases: 0, 0.25, and 0.5 inch.

- (7) Ratio of the smallest and largest partial energy above
- (8) Number of peaks exceeding a given threshold
- (9) Frequency at which 25% of total energy occurs. Total energy is defined as

$$E = \frac{1}{2} \pi \int_{-\infty}^{\infty} |F(\omega)|^2 d\omega$$

- (10) Frequency at which 50% of total energy occurs.
- (11) Frequency at which 75% of total energy occurs.

Features number (4) to (11) detect the energy distribution in certain frequency bands. As the ice accumulates, resonant modes of the structure will change. Therefore the energy concentration will change. In structures which have a large number of modes, such as a thin plate with rigid boundaries, these features are particularly useful for classifying the ice thickness.

5.2.3 General Properties and Curve Shape

Three features lie in this category: standard deviation, skewness rate, and kurtosis. Standard deviation is an indication of the variation of the signal from its mean value. Skewness rate is the measurement of the curve shape, and the degree of asymmetry of a distribution around its mean. If the curve leans to the left for a given curve, for example a normal function curve, the skewness rate in this case is smaller than if it leans to the right. Skewness is a nondimensional number which characterizes only the shape of the distribution. The kurtosis, on the other hand, emphasizes more the variation of the tail of the signal, and the relative peakedness or flatness of a distribution. It is also a nondimensional number.

- (1) Standard deviation of the signal, σ , can be defined as:

$$\sigma(x_1, \dots, x_n) = \sqrt{\text{Var}(X_1 \dots X_n)}$$

where
$$\text{Var}(x_1, \dots, x_n) = \frac{1}{N-1} \sum_{j=1}^N (x_j - \bar{x})^2$$

- (2) Kurtosis of the signal K_u . K_u is the ratio of the fourth moment to the square the second moment or

$$K_u = \frac{M_4}{M_2^2} \quad \text{where} \quad M_n = \int_0^{\infty} t^n f(t) dt$$

- (3) Skewness of the signal, S_k . S_k is the ratio of the third moment to 1.5 power of the second moment, or

$$S_k = M_3/(M_2)^{1.5}$$

5.2.4 Transfer Function

If more than one sensor signal is available, a ratio of two of them can be used to generate another feature called the transfer function. The transfer function takes into account the geometric effects to the system response due to the ice presence. It also isolates pyroelectric effects caused by the temperature dependent piezoelectric constants. There are two features in this category used in the deicing application. Each examines the power spectrum of the transfer function in two different frequency bands.

5.3 Classification

The features for each signal are stored by the computer during the training process. After the learning process, the computer classifies the signal to determine which group of predetermined categories the signal belongs to. For example, for the study here we want to classify ice on the structure ranging from 0 to 0.5 inch thick, in 0.05 inch increments. The signals that represent a specified ice thickness are therefore divided into eleven classes, or groups, each of which is in increments of 0.05 inch (ie. 0, 0.05, 0.10, etc). When a measured signal is classified, it is assigned into one of these eleven classes according to its characteristics.

The classification used here is based on the Euclidean distance:

$$d(x,y) = [\sum (x_i - y_i)^2]^{1/2}$$

where $d(x,y)$ --- distance of two vectors or signals x and y ,
 y_i --- the i th feature of signal y .

The y signal belongs to the subgroup of x if d is the smallest. If the Euclidean distance is used, linear discriminant functions

$$p_i(y) = \sum y_k x_{ik} - 0.5 \sum x_{ik}^2$$

will suffice. The class determination is based on the evaluation of the class function:

$$c_i(y) = i \quad \text{if } p_i(y) > p_j(y) \text{ for all } j \text{ not equal to } i$$

This classification method is called prototype classification. The basic assumption is that a measurement x_i is a "perfect" example of each class S_i , and every member of S_i is a distortion of that prototype. The prototype value for a given class can be replaced by the mean value of a set of measurements under the same icing condition and ice thickness. If the sample standard deviation is very small such that the same feature in two neighbor classes can still be differentiated, one can expect the classification is acceptable. If the feature values of two neighbor classes from the same feature are in three standard deviations, the confidence level can be more than 99% in a normal distribution population.

In preliminary icing tunnel tests, it was found that temperature has a very strong influence on the type and distribution of the ice formation. Temperature, therefore, is used to group the signals. The classification is performed in a particular group of signals according to their temperature range.

5.4 Detailed Program Structure

The program structure is shown in Figure 16. The software consists of a main program which calls 4 subroutines: 1) TRAIN, 2) PATRN, 3) CLASS, and 4) DECIDE. The procedure consists of a training stage and a testing stage. Input to the training stage is a representative sample of signals describing the system. The training subroutine, TRAIN, extracts the feature vector and builds up the statistics which describe each signal. An identity of the signal is tagged to each of the feature vectors. In other words, each digitized sensor signal is represented by a vector with user-defined features and the physical properties which define the signal (ie. ice thickness, temperature, etc). All the physical properties and features of the training signals are stored in the matrix [PHYS] and [PTN], respectively.

Once the system is trained, the MAIN program calls PATRN which acquires N signal measurements and calculates the features for each signal. These features are stored in the feature matrix [SPTN]. The CLASS subroutine classifies these incoming signals. The features derived from the training samples, [PTN], are compared with their unknown counterparts extracted from the incoming signals, [SPTN]. By analyzing their differences and similarities, the system identifies the input signals and stores the physical property vectors into the matrix [SPHYS]. The DECIDE subroutine then determines the present ice thickness and displays on-line the ice thickness on the computer monitor. If the ice thickness reaches a pre-defined threshold, the deicing actuator sequence is turned on to remove the ice.

A description of the program routines is given below:

MAIN - This is the main program of the pattern recognition software package and controls the information flow among the subroutines (see Figure 17).

- TRAIN -** This routine calculates the feature vector and builds up the statistics which describe each training signal. The physical property and feature matrix of the training signals, [PHYS] and [PTN], respectively, are stored in the data file ICE.DAT (see Figure 18).
- PATRN -** This routine acquires N signal measurements and calculates the feature vector of each sensor signal. These features are stored in the feature matrix [SPTN] (see Figure 19).
- SIGNAL -** Subroutine SIGNAL acquires the sensor signal measurements through the Data Acquisition Board.
- FTIME -** This routine computes the time domain signal features (see Figure 20).
- STATIS -** This routine calculates the following statistical values of the given signal:
1. Average value
 2. Variance
 3. Standard deviation
 4. Skewness rate
 5. Kurtosis number
- PEAK -** Subroutine PEAK selects all the peak values above a threshold of a given function.
- AREA -** This routine integrates a given function over the region from N1 to N2.
- ENDPNT -** This routine calculates the endpoint of the integration, N2, given by the partial integration value and the total integration value.
- FFT -** This routine performs the fast Fourier transfer function for a given time signal.
- FFREQ -** This routine computes the frequency domain signal features (see Figure 21).
- CLASS -** This is a signal classification routine. It performs the assignment of physical properties to the incoming signal according to the Nearest Neighbor Decision Rule. The features derived from the training samples, [PTN], are compared with their unknown counterparts extracted from the incoming signals, [SPTN]. By analyzing their similarities and differences, the system identifies the unknown signal. It assigns the physical property vector of the closest training signal to the unknown signal and stores the vector for each signal in [SPHYS] (see Figure 22). The algorithm used is the Euclidean Distance

Equation with weighting functions:

$$D_j = \{ K_{Pi} * [K_{Di} * (X_{Si} - X_{Tij})] \}$$

where

D_j -- The distance of the incoming signal with the j th training signal.
 K_{Di} -- Dimension weighting function of the i th feature.
 K_{Pi} -- Preference weighting function of the i th feature.
 X_{Si} -- The i th feature of the incoming signal.
 X_{Tij} -- The i th feature of the j th training signal.
 NF -- Number of features used to characterize a signal.

- DLIB - This routine is the decision library which selects a sub-set of the training feature matrix [PTN] based on the temperature sensor and determines the weighting function for the signal features. In addition, it weights the sensor signals (see Figure 23).
- CURVE - Subroutine CURVE displays the average ice thickness and key features on the computer monitor.
- CNTRL - This routine controls the High Voltage (HV) power supply settings. During the measurement cycle, it sets the HV supply to its lower setting and triggers the EIDI coils. If a deicing cycle is necessary, it sets the HV supply to maximum and triggers the EIDI coils.
- DECIDE - This routine determines the present ice thickness and displays on-line the ice thickness versus measurement time on the computer monitor. If the ice thickness reaches a pre-defined threshold, the deicing actuator sequence is turned on to remove the ice (see Figure 24).

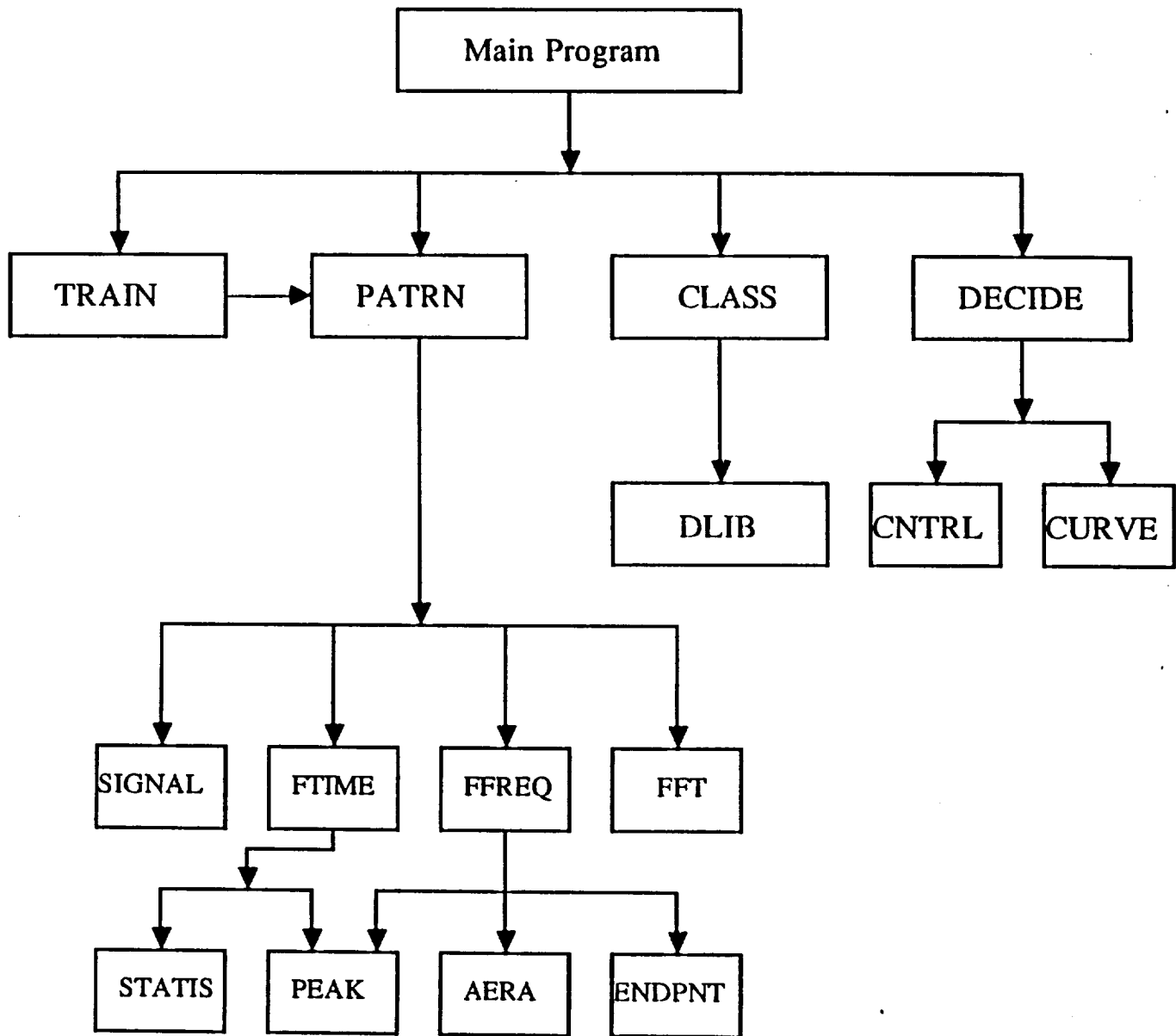


Figure 16. Program Structure -- Main Program and Subroutines

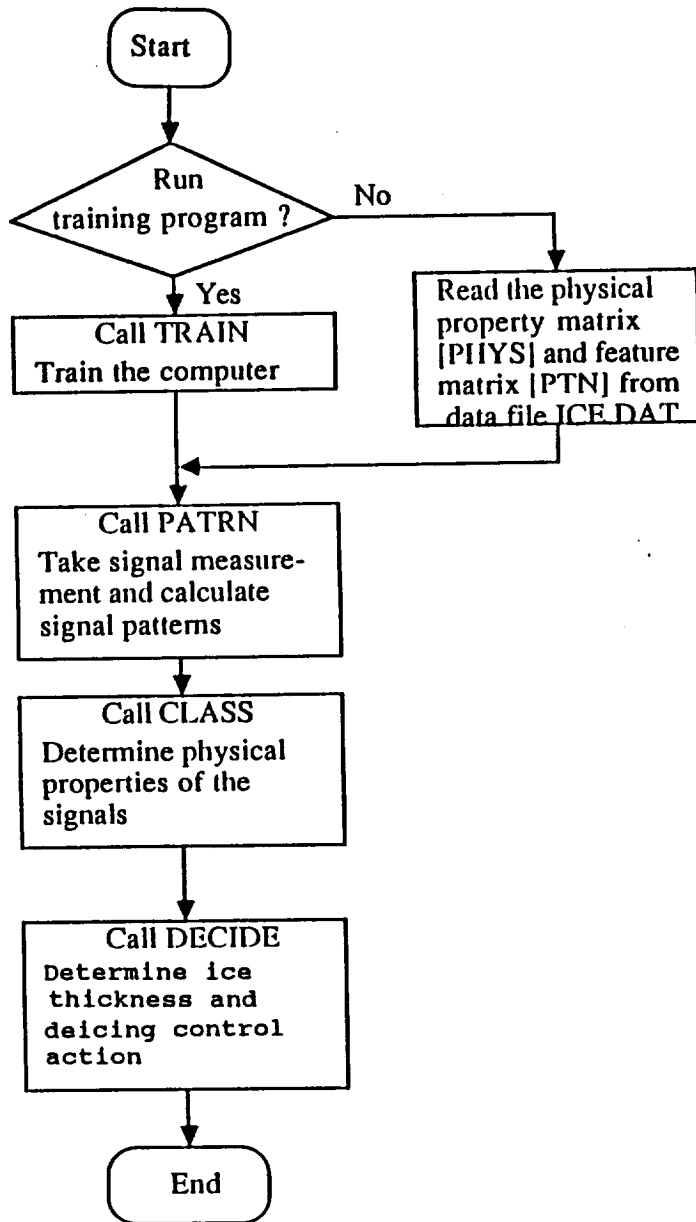


Figure 17. MAIN Program

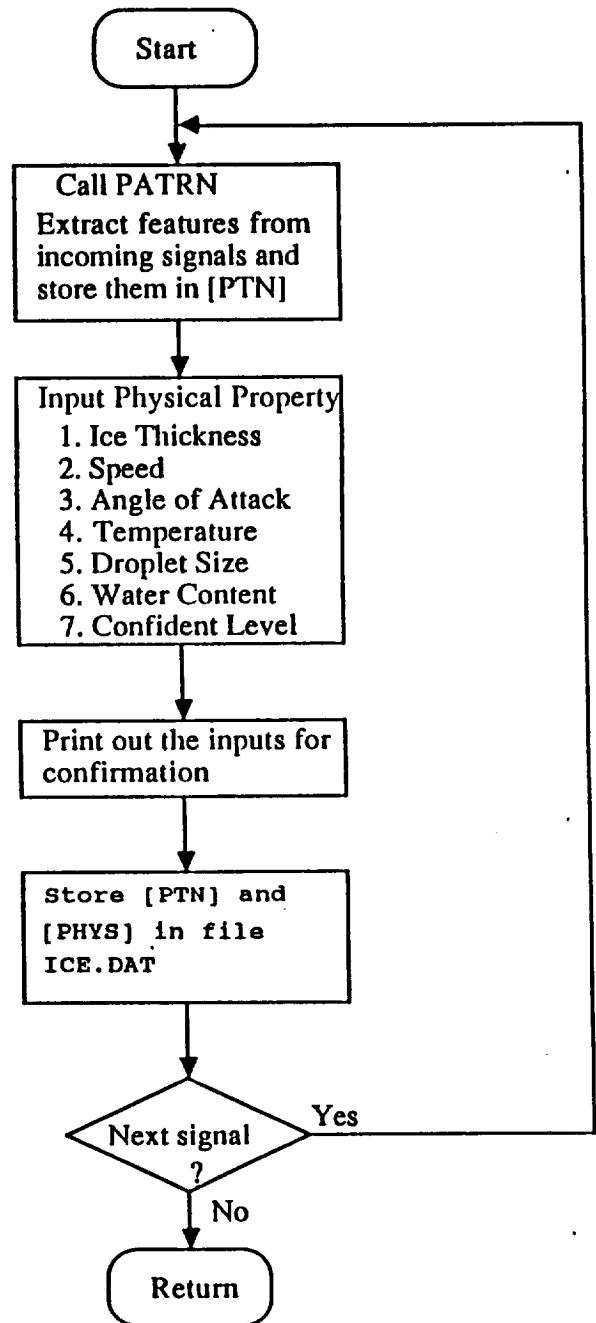


Figure 18. Subroutine TRAIN

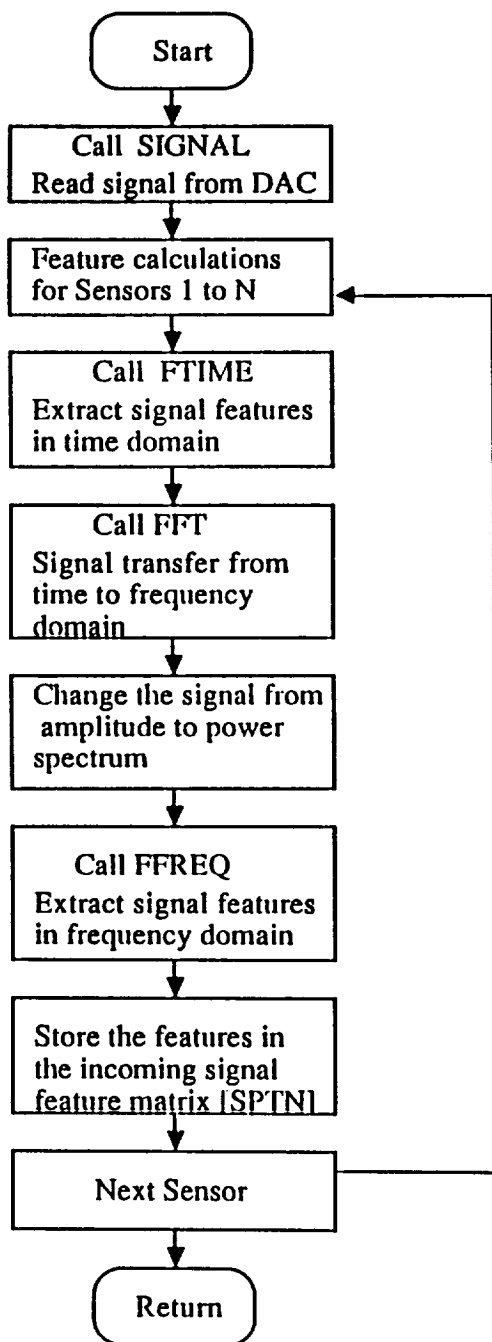


Figure 19. Subroutine PATRN

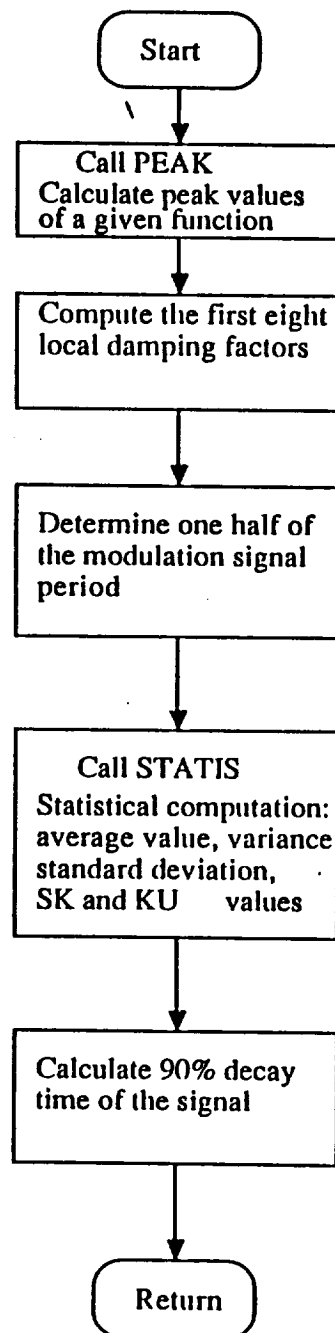


Figure 20. Subroutine FTIME

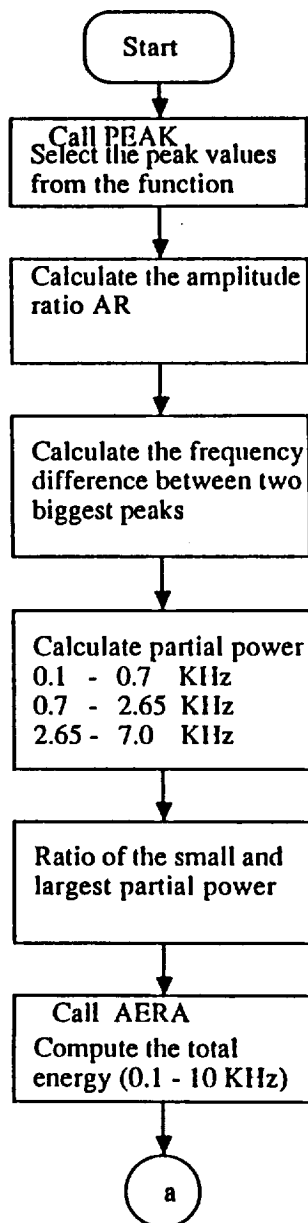


Figure 21. Subroutine FFREQ

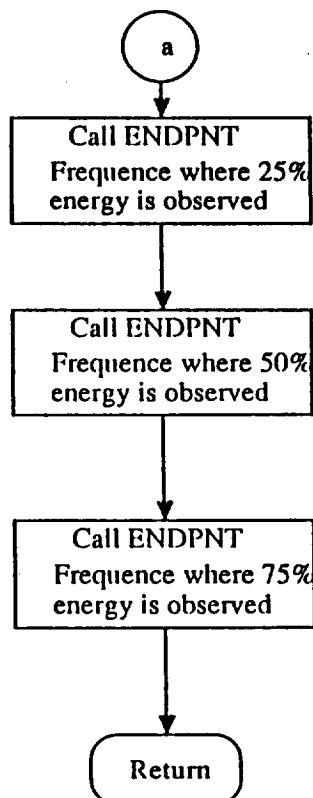
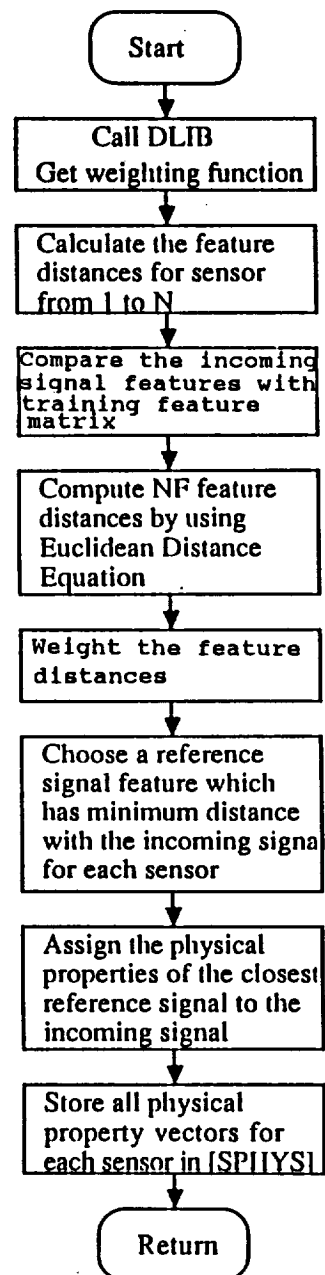


Figure 22. Subroutine CLASS



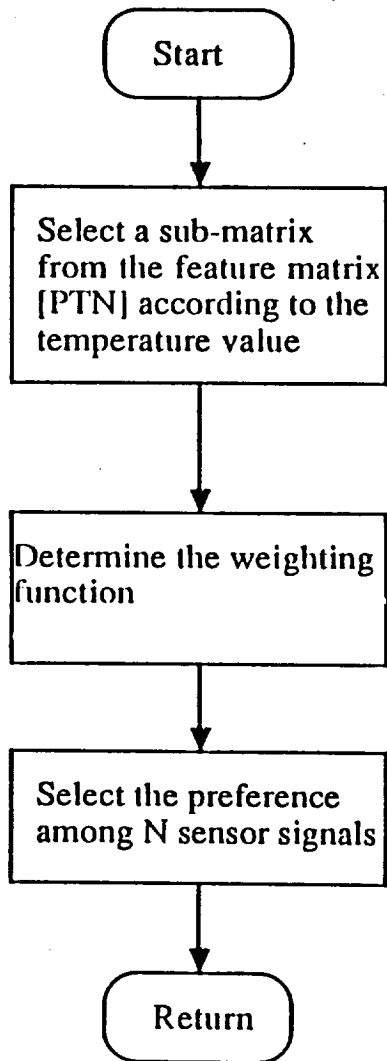


Figure 23. Subroutine DLIB

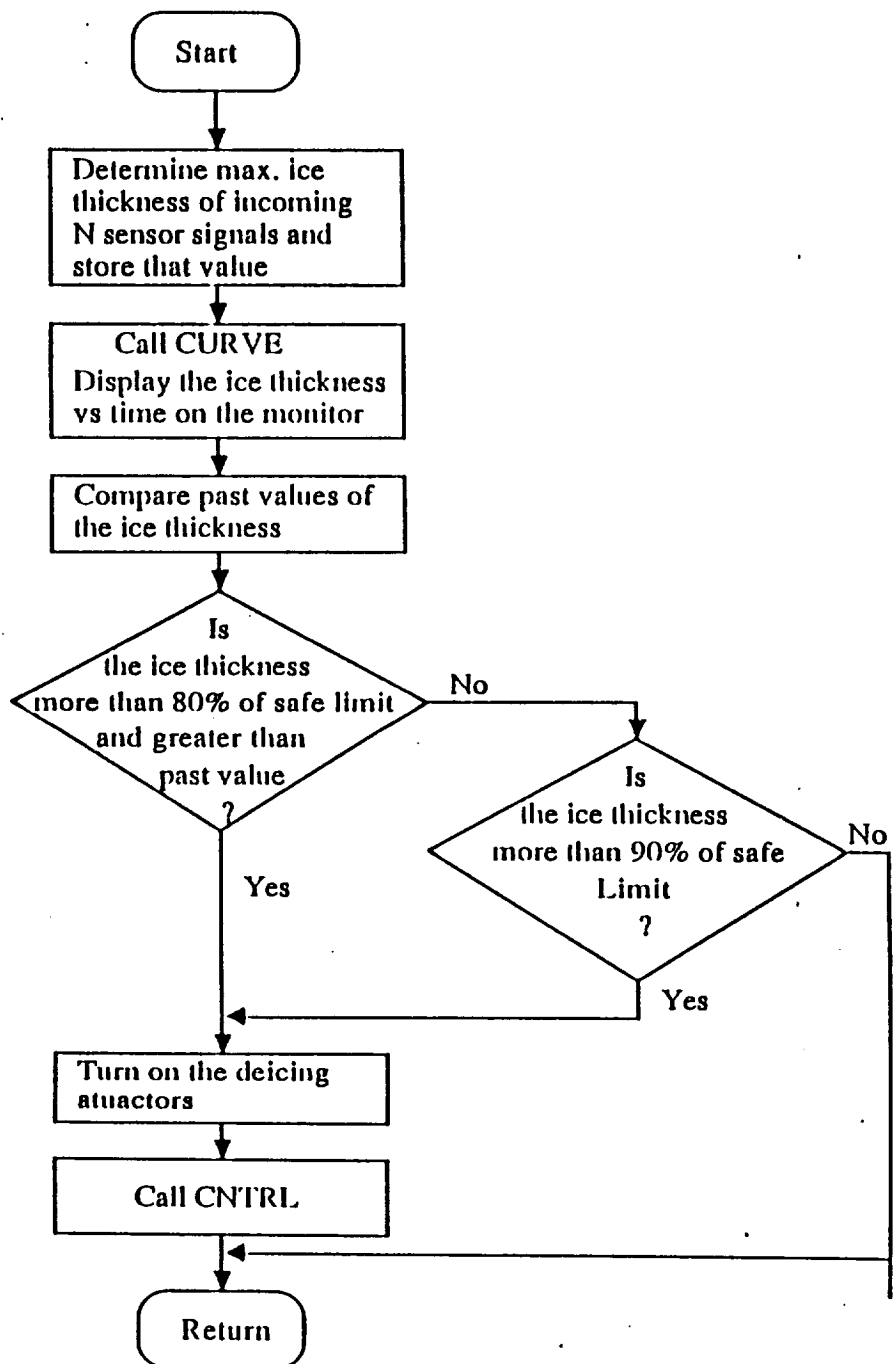


Figure 24. Subroutine DECIDE

6 ICING TUNNEL TESTS

An essential part of developing the ISIPS system was testing in the NASA Icing Research Tunnel (IRT) at the Lewis Research Center in Cleveland, Ohio. The test section of 2 by 3 meters permits full-scale testing of many aircraft components such as wing sections, engine inlets and tail sections. Airspeeds over 250 mph and temperatures below -10°F can be obtained. The spray system provides a range of subcooled water droplets with median volume diameters from 10 to 40 microns and a range of liquid water content values.

Preliminary open-loop ice sensor tests were performed in July 1989. Sensor response to varying ice thicknesses for a range of icing conditions was evaluated. These tests resulted in the decision to use pattern recognition techniques to aid in the analysis of the sensor data. A series of tests in the IRT was then performed in 1990 during the week of January 22-26, to demonstrate full closed-loop system performance. The procedures and results of this test are summarized below.

6.1 Test Procedures

The wing cuff along with associated electronics was installed in the IRT (see Photos 1-3). Initial icing tests were performed in the IRT to determine the preferred sensor configuration, system gain settings, and EIDI impulse voltage level required to excite the sensors. A total of 4 piezoelectric sensors positioned inside the leading edge surface of the wing cuff near the stagnation line (SL) were used during the training:

Sensor	Size (inch)	Capacitance (μ F)	Position
1	2 x 10.5	48	Spanwise along SL, Bay #3
2	2 x 4	15	Chordwise about SL, Bay #3
3	2 x 10.5	48	Spanwise along SL, Bay #2
4	2 x 2	10	Chordwise along SL, Bay #2

EIDI eddy-coils located in bays 1 and 3 were pulsed at 250 V in series during the sensing mode. At this voltage level, a sensor gain of x10 was required to produce an adequate signal level between 1-4 V. During the deicing cycle, the eddy-coils were pulsed two at a time (bays 1 and 3, and bays 2 and 4) at 1100 V. A representative sample of signals for a range of ice cases were used to generate the ice database. Tests were performed at the following conditions:

Temperature	28°F, 15°F and -10°F
Velocity	100 and 150 mph
AOA (angle of attack)	0° and 6.3°
LWC (liquid water content)	0.5, 0.7, 1.0 g/cm ³
DIA (droplet size)	14, 20, 40 μ m

The maximum velocity that would usually be experienced on the Twin Otter at a given AOA was tested. For the AOA setting of 0° and for 6.3° , the tunnel was run at 150 mph and at 100 mph, respectively.

During a test run, the ice was allowed to build up continuously on the cuff and the ice thickness was visually estimated. The system was trained in increments of 0.05 inch of ice. Once a maximum thickness of 0.5 inch of ice was reached, the ice was removed with the EIDI eddy-coils before the start of the next test. Remaining ice on the cuff was manually removed using scrapers. Six physical parameters were used to define each training signal: ice thickness, temperature, velocity, AOA, LWC, and DIA.

It was observed that the baseline case (no ice) varied from day to day. This variation was probably due to water from the IRT leaking into the wing cuff and freezing, causing the structure vibration signature to change. To alleviate this problem, a baseline measurement was taken and added to the database before the beginning of each test run.

As the ice database was increased during the training session, the system was periodically tested to determine if the classifier could correctly identify the ice thickness. Once the system was trained, tests were performed for similar icing conditions used during the training to determine which group of features is the best in characterizing the sensor signals. Post-analysis of the feature set was performed in order to optimize the sensor recognition rate.

6.2 Results

6.2.1 IRT Tests

During the training session, 11 test runs were conducted in the icing tunnel. A total of 118 measurements were acquired and stored in the ice database. Various feature sets were tested in the IRT for a range of icing conditions once the computer was trained. Without any feature set optimization, the pattern recognition software worked well for ice thickness ranging from 0 to 0.3 inch. Above 0.3 inch, the recognition rate tended to decrease. This can be explained by looking at plots of the pattern features (see following section). Above 0.3 inch, several of the features tended to flatten out, providing no useful information.

Once a critical ice thickness was detected, the system successfully initiated the deicing sequence to automatically remove the ice accretion. The loss of one capacitor just before the test, however, reduced the deicing energy level by approximately 20%; therefore, it took a greater number of hits to deice the wing, between 10-20 hits.

6.2.2 Feature Set Analysis/Optimization

Post-analysis of the ice database was performed to determine the optimal feature set. The

feature space which was extracted from the measurement space, was carefully examined in order to ensure that the features selected are meaningful and required for proper signal classification. The twenty-six features extracted from the measurement space formed the original feature set.

Note that it was assumed that ice thickness is mainly a function of temperature, AOA, DIA, and LWC. Since the training procedure is time consuming and test time was limited, only one measurement was taken for each test condition. Ideally, a very large number of test points should be taken to ensure the correct population distribution. Here, it was assumed that each measurement in the test is a normal distributed function and the variation of the population in each class is very small. Therefore, each measurement can be regarded as one subclass and all measurements representing the same ice thickness can be clustered as one class.

Histogram Analysis

The feature selection is based on histogram analysis. All the features are plotted as a function of ice thickness for a given class. This gives a graphical means to examine the characteristics of each feature. If a feature plotted against ice thickness gives a smooth curve, it is considered reasonable from simple structural dynamic considerations. If the curve of the feature is relatively flat, then this particular feature is considered meaningless since it can not provide any useful information for pattern classification.

Based on the twenty-six features identified, all features as a function of ice thickness are evaluated within the same temperature range. Plots of these features for all of the test runs performed in the IRT are shown in Appendix C. Note that all the features are shown for sensor 1 for the 30°F test runs. However, several of these features proved to be very poor and are therefore not included in the rest of the test cases. Some typical features of sensor 1 are shown in Figure 25 for the following four test runs at -10°F:

- | | | | | | | | | |
|----|------|-----|------|------|------|------|------|-----|
| 1) | DIA= | 20, | AOA= | 6.3, | TAS= | 100, | LWC= | 1 |
| 2) | " | | 0 | | 150 | | | 1 |
| 3) | " | | 0 | | 150 | | | 0.7 |
| 4) | " | | 6.3 | | 100 | | | 0.7 |

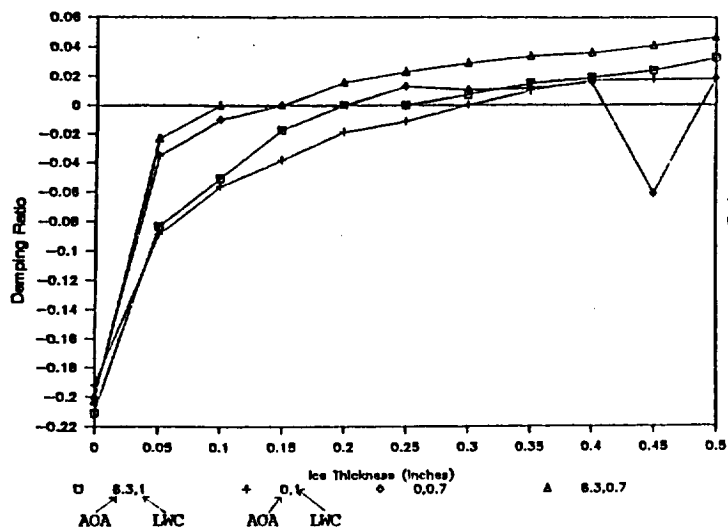
Figure 25a shows the first local damping factor. This feature increases as the ice thickness increases. Figures b and c show the second and the third local damping under the same tests conditions, respectively. The second local damping initially drops for thin amounts of ice and then increases as the ice increases. The ice has an opposite effect on the third local damping feature. It first increases and then decreases. The features describing the amount of energy present in three different frequency bands are shown in Figures d, e and f: 1) 700 - 1150 Hz, 2) 1150 - 1800 Hz, and 3) 1800 - 3000 Hz. In order to eliminate the effect of structure vibration noise, the energy calculation begins at 700 Hz instead of 0

Hz. Energy in the first frequency band tends to decrease with ice thickness and increase in the second frequency band. Not much change occurs in the higher frequency band. The frequency at which 25%, 50%, and 75% of accumulated energy is observed is shown in Figures g - i. The first two features tend to increase with ice thickness, while the third feature decreases. Figure j shows the effect of ice on the second transfer function feature (ratio of the energy in the second frequency band of sensor 1 and sensor 2). This feature decreases with ice thickness.

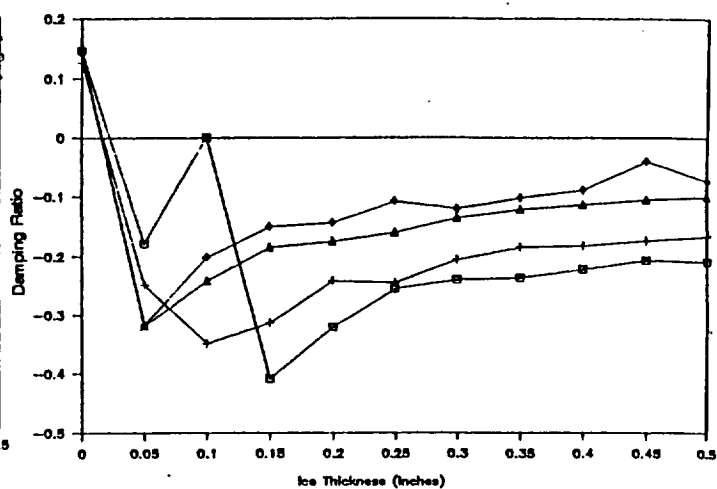
In general, these curves indicate that the features tend to initially change a lot with small amounts of ice and tend to level out and not change much with thicker ice accretions. For the different temperature ranges tested, the feature patterns varied a lot. This variation is mainly due to the dominant effect that temperature has in the ice formation process. That is, glaze ice normally occurred at temperatures near freezing (or high LWC). Rime ice growth usually occurred at colder temperatures where there was sufficient cooling to freeze the droplets on impact. The different ice distributions that formed tended to have a dominant effect on the vibration response. Additionally, temperature changes greater than 10° caused a noticeable change in the baseline structural vibration signature. A thermocouple was used to compensate for this baseline variation over the three temperature ranges tested.

In order to determine the best feature set, the features for each sensor were then classified into three categories: good, fair, and poor. The definition of "good" is that the feature is smooth (does not jump around a lot) and the slope of the curve is not zero. A large curvature means that this feature can provide very clear information for use in discriminating the sensor signal. The definition of "fair" is that the feature curve may have a few sporadic points out of the general trend of a smooth curve. Also, the curvature of the curve exists, but may not be very large. The definition of "poor" is that the feature curve varies randomly, or the curve is completely flat. Note that irregular variations of data points from a generally smooth curve may be caused by a poor measurement (such as variation in the sensor excitation pulse) or by actual variations caused by irregularities of the ice formation itself. It may also be caused by the complicated nonlinear structure response. To help determine the actual effect, further testing should be performed using averaging.

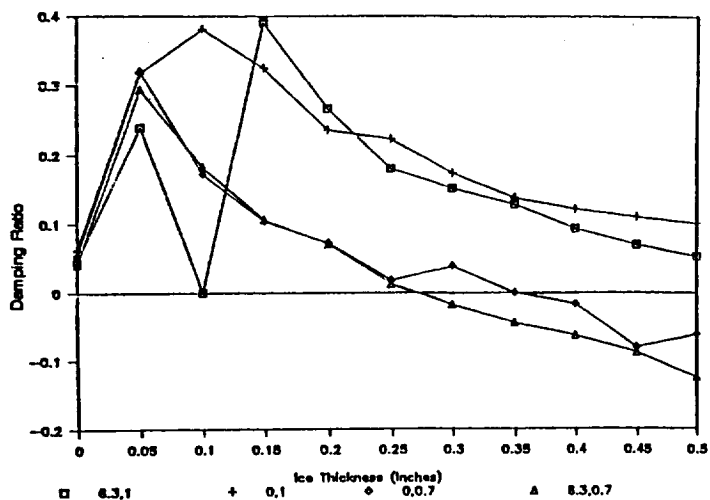
The resulting categories of each feature for all four sensors are given in Table 6. Since some of the features were very poor, they have not been included in the table. It is obvious by looking at the table that features 15, 23 and 24 have a smaller number of "good" curves and larger number of "poor" curves. They have therefore been dropped out the feature set. Only features 1, 14, 16, 17, 18, 19, 20, 22, 25, and 26 are selected. Table 6 lists the percentages of "good" and "poor" features before and after the feature set reduction. The percentage of "good" curves is increased from 60% to 68% and the percentage of "poor" curves is reduced from 29% to 20%.



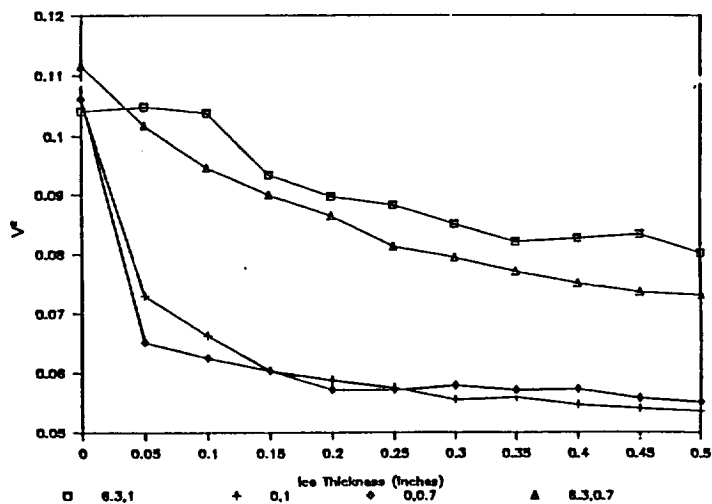
(a) First local damping



(b) Second local damping



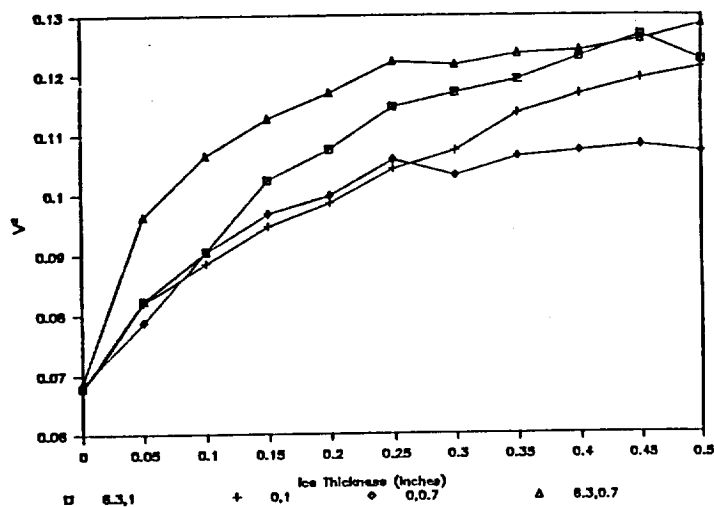
(c) Third local damping



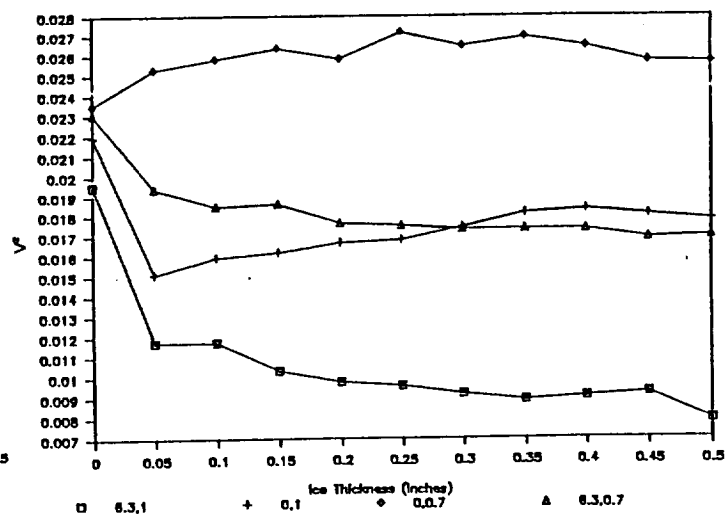
(d) Accumulated power in freq band 700 - 1150 kHz

Figure 25. Sensor 1 feature plots vs ice thickness. (IRT test conditions: -10°F, DIA 20, variable AOA and LWC)

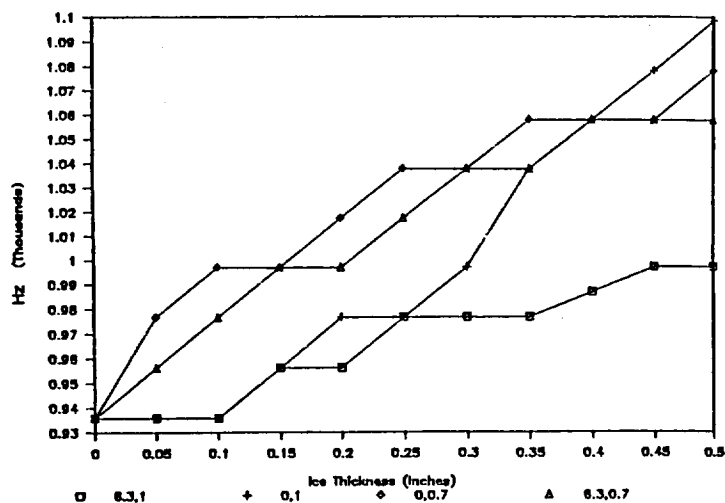
Figure 25 (Continued)



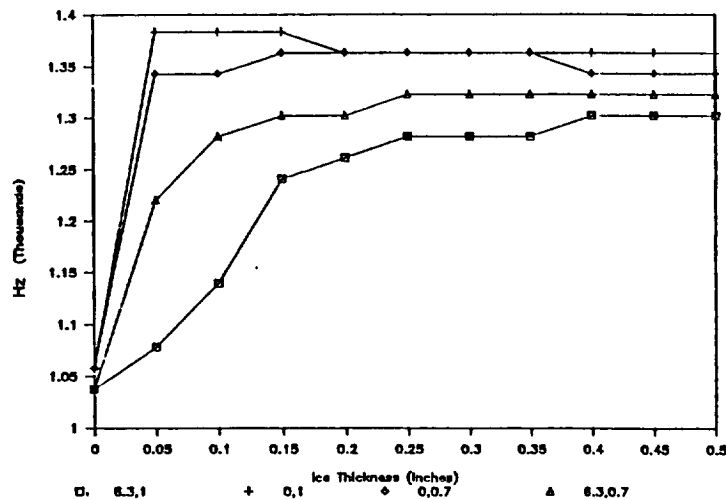
(e) Accumulated power in freq band
1150 - 1800 kHz



(f) Accumulated power in freq band
1800 - 3000 kHz

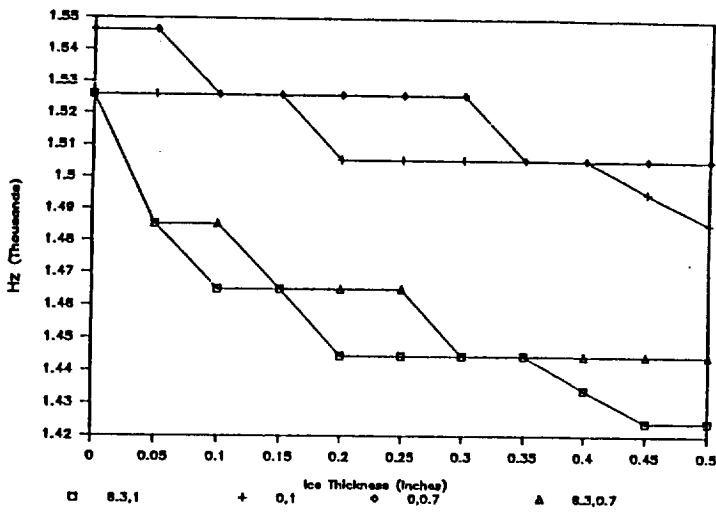


(g) Frequency at which 25% of
accumulated power was observed

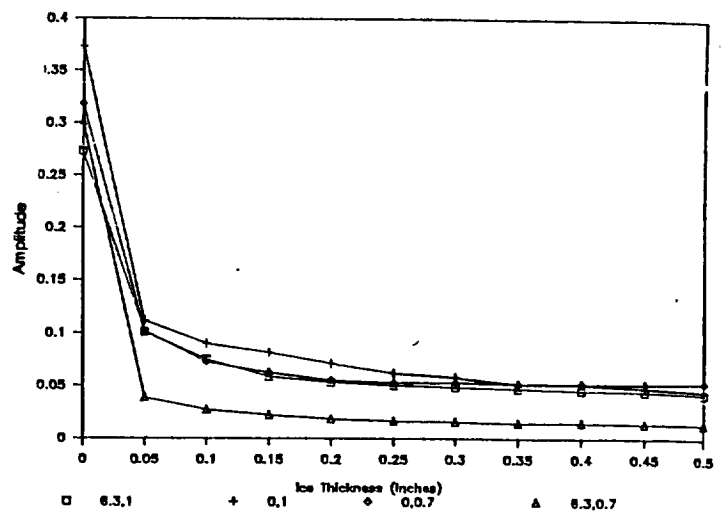


(h) Frequency at which 50% of
accumulated power was observed

Figure 25 (Concluded)



(i) Frequency at which 75% of accumulated power was observed



(j) Transfer Function 2

Table 6. Feature classification for each sensor.

CATEGORY FEATURE	SENSOR 1			SENSOR 2			SENSOR 3			SENSOR 4			SUM		
	GOOD	FAIR	POOR	GOOD	FAIR	POOR	GOOD	FAIR	POOR	GOOD	FAIR	POOR	GOOD	FAIR	POOR
1	10	0	1	0	2	9	10	0	1	5	1	5	25	3	16
14	6	4	1	5	5	1	7	3	1	7	0	4	25	12	7
15	2	0	9	3	0	8	2	0	9	0	0	11	7	0	37
16	6	4	1	7	1	3	3	5	3	9	0	2	25	10	9
17	9	0	2	7	4	0	8	1	2	9	0	2	33	5	6
18	11	0	0	7	3	1	11	0	0	9	0	2	38	3	3
19	9	1	1	4	2	5	8	0	3	8	0	3	29	3	12
20	7	0	4	6	3	2	7	2	2	5	2	4	25	7	12
22	6	4	1	5	1	5	7	3	1	8	0	3	26	8	10
23	7	2	2	4	1	6	4	0	7	3	0	8	18	3	23
24	4	1	6	7	0	4	4	1	6	4	0	7	19	2	23
25	6	3	2	6	3	2	10	0	1	10	0	1	32	6	6
26	11	0	0	11	0	0	9	0	2	9	0	2	40	0	4
SUM (ALL SELECTED)	94	19	30	72	25	46	90	15	38	96	3	54	342	62	168
SUM (PARTIAL SELECTED)*	81	16	13	58	24	28	79	14	17	79	3	28	297	57	86
*Only Features 1, 14, 16, 17, 18, 19, 20, 22, 25, and 26 are selected.															

Correlation Analysis

Although histogram analysis is very useful in selecting the good features, it does not guarantee that all of them are useful in the application of the pattern recognition algorithm. If some of them are highly correlated, they are not suitable for use. A highly correlated feature will generally increase the weighting of that particular feature, and therefore reduce the merits of others.

A correlation analysis was performed for all 11 test runs and for each sensor. It is very interesting to note that some features are highly correlated in one run but not in another run for a given sensor. Or some features are highly correlated for one sensor but not for

another sensor in one particular run but not another. In general in this particular application, it appears that it is very difficult to determine features using this correlation technique. This phenomenon leads to the conclusion that the features selected by histogram analysis should be valid for inclusion in the pattern recognition system.

6.2.3 Simulation Tests

In order to test the recognition rate of the model and different feature sets, thirty samples were randomly selected from the ice database which was previously acquired in the IRT. The thirty samples should give a good estimation of the system performance. The test strategy was to remove one of the thirty samples from the database, one at a time, and test the system response using this test sample. Note that if the test sample is not removed from the data base, the recognition rate should be 100%.

Table 7 lists the recognition rate for various feature sets. Shown is the recognition rate of each sensor as well as the rate of the overall system. When all twenty-six features are used (Feature Set 1), the recognition rate of the system is 63.3% with a resolution of 0.05 inch. Sensor 3 gives the highest recognition rate (70%) and Sensor 2 gives the lowest (43%). If the reduced feature set is used (Feature Set 2), the system recognition rate is increased to 93.3%. Sensor 3 again demonstrates the best performance -- 90% recognition rate. Sensor 2 still has the poorest performance -- 60% recognition rate. It can be seen that performance of all sensors, however, can be significantly improved by proper feature selection. Using Feature Set 2, a recognition rate of 100% can be achieved with a resolution of 0.075 inch.

The recognition rates of Sensor 1 and 3 are very high among all four sensors. It is obvious that Sensor 2 gives the lowest recognition rate. This poor performance was probably due to a loose sensor lead which occurred during testing. The recognition rate of Sensor 4 is also far below Sensors 1 and 3. Sensors 1 and 3 have the highest recognition rates. Note that these sensors were positioned on the leading edge along the stagnation line where generally the ice tended to be centered. These results indicate that proper sensor position is important to achieving good signal classification.

The high recognition rate of the system provides a reliable technique for ice detection. Based on the present recognition rate of 93.3%, let's determine what the chance is that the computer will miss a critical ice thickness condition. Assume that ice is building up on the wing and that the critical ice level has been reached. An ice measurement is taken. The chance that the computer will classify the signal wrong and give a smaller ice thickness reading is 6.7%. The deicing actuator will therefore not be activated and the ice will keep building up. The sensor will then take another measurement. The probability that the computer will misclassify the signal a second time is now 0.45% ($P_2 = 6.7\% \times 6.7\%$). If the computer again makes a wrong decision, the ice will continually build and another measurement is taken. This time the probability of misclassifying the signal is

now only 0.03% ($P_3 = 6.7\% \times 6.7\% \times 6.7\%$). Therefore, if the speed of the recognition operation is faster than the speed of ice build up during three measurements, the deicing system should be extremely reliable.

Table 7. Performance comparison of different feature groups.

RECOGNITION RATE		
	TEST SET	
	FEATURE SET 1 (ALL FEATURES SELECTED)	FEATURE SET 2*
SENSOR 1	66.7%	86.7%
SENSOR 2	43.3%	60%
SENSOR 3	70%	90%
SENSOR 4	56.7%	70%
SYSTEM	63.3%	93.3%

* Features 1, 14, 16, 17, 18, 19, 20, 22, 25, 26 are selected.

7 FLIGHT TESTS

To evaluate system performance in the flight environment, a series of flight tests were completed in the well-instrumented NASA Lewis Icing Research Aircraft, a DeHavilland DHC-6 Twin Otter. An initial flight test was performed in July 1989 to measure the background vibration noise level to ensure adequate sensor signal to noise ratio. Piezoelectric film sensors (1 inch square) were installed in the inside surface of the leading edge wing and vibration measurements were taken for a range of airspeeds and power settings. A maximum noise level of -40 dB was measured at approximately 100 Hz and then rolled off below -70 dB after 1 kHz. Based on tests in the lab, it was predicted that an EIDI excitation pulse of at least 250 V (2 coils in series) should be sufficient to produce an adequate signal to noise ratio.

Due to the relatively low vibration noise levels measured on the aircraft, and the successful demonstration of ISIPS hardware and software in the IRT, it was now feasible to evaluate performance of the system in the flight environment. A four week flight test program of the closed loop ISIPS system installed on the Twin Otter aircraft was performed in March 1990. These icing tests on the IRA are summarized below.

7.1 Test Procedure

The system was installed on the NASA DHC-6 as depicted in Figure 26 (also see Photos 1-3). Initial flight tests were performed over a range of airspeeds (100 - 150 knots) and power settings (75 - 95%) to check out the equipment and determine EIDI impulse voltage excitation levels and sensor gain settings. The four sensors used in the IRT tests were used in the flight tests. A voltage setting of 250 V was used during the measurement cycle. At this voltage setting, a sensor gain of x10 was used.

Due to differences in the boundary conditions of the cuff on the Twin Otter wing than on the tunnel test fixture, the structural response of the cuff was significantly altered so that the data base generated in the tunnel could not be used. Therefore, the system had to be retrained on the aircraft. However, only a few natural icing tests were flown due to the environmental conditions at the time of testing. Therefore, further tests were performed using simulated ice. The ice consisted of 0.005" thick layers of 3 inch wide aluminum tape attached to the leading edge of the wing cuff. The tape was positioned at the stagnation line and ran the spanwise length of the entire cuff. The system was trained on the ground for up to 4 layers of tape and then tested, both on the ground and in-flight, to determine the performance of the sensor.

In addition to these simulated ice tests performed using the eddy-coil as the impulse, tests were performed using natural in-flight engine and aerodynamic vibration noise as the excitation source. This technique would be advantageous for application in a passive health monitoring system. For these tests, the sensor gain was increased to x100.

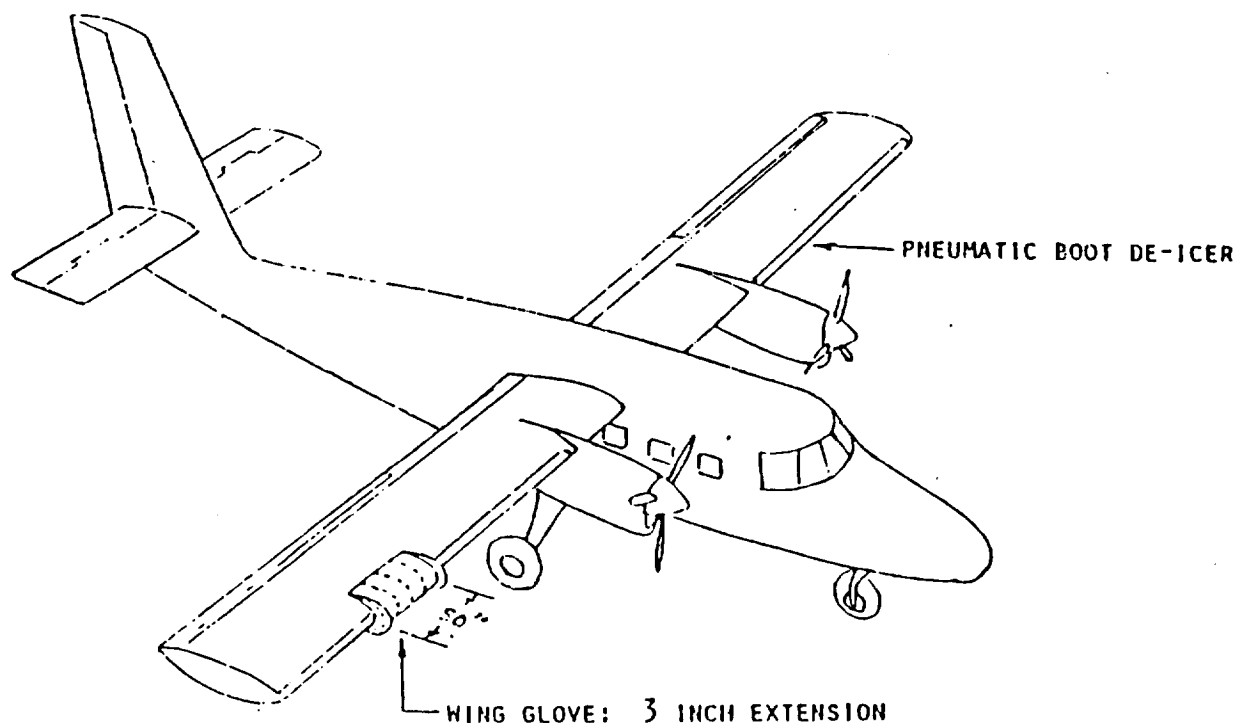


Figure 26. Wing cuff installed on Twin Otter aircraft.

7.2 Results

A comparison of the in-flight vibration signature of the wing cuff measured with sensor 1 for a range of EIDI voltage settings is shown in Figure 27. For the lower voltage setting of 150V, an adequate signal to noise ratio of 40 dB at frequencies above 1 kHz could still be attained. Therefore, the sensor eddy-coil could be pulsed at least 100 V lower than the voltage setting used during the tests and still have an adequate signal to noise ratio. It was observed that over the range of airspeeds and power settings, the vibration response did not vary significantly and therefore the system did not have to be retrained at different flight conditions.

Because only limited icing conditions were available, a comprehensive ice data base could not be generated. However, for the ice cases that the system was trained to recognize, it worked well. Several features of sensor 4 are depicted in Figure 28 for the following flight test condition: 100 knots, 5000' altitude, -6°C , average LWC of 0.15. It is seen that as the ice thickness increases, the power increases in frequency band 0.7 - 1.15 kHz and decreases in frequency band 1.8 - 3.0 kHz. The power ratio of the two peak frequencies also increases as a function of ice thickness.

The flight tests demonstrated sensitivity of the sensor to be at least 0.005" to aluminum tape. The system was first trained on the ground. Figures 29a and b depict the variation of the structural response of the wing cuff for various layers of tape measured on the ground and in-flight, respectively. It is seen that in certain frequency bands the amplitude of the signal increases as the thickness of the simulated ice increases and decreases in other bands. This shift in energy was used to reliably detect the various simulated ice layers (100% recognition rate).

Figure 30 depicts the vibration response of the wing cuff for various simulated ice thicknesses using only the engine and aerodynamic noise as the excitation source. The power spectral data of the sensor signals indicate that it may be possible to identify ice accretion if the pattern features are optimized for this specific application. It can be seen that as the thickness of the ice increases, the energy in the higher frequency bands from 5 - 10 kHz decreases. Further study should be performed to determine system sensitivity and reliability using this passive detection approach.

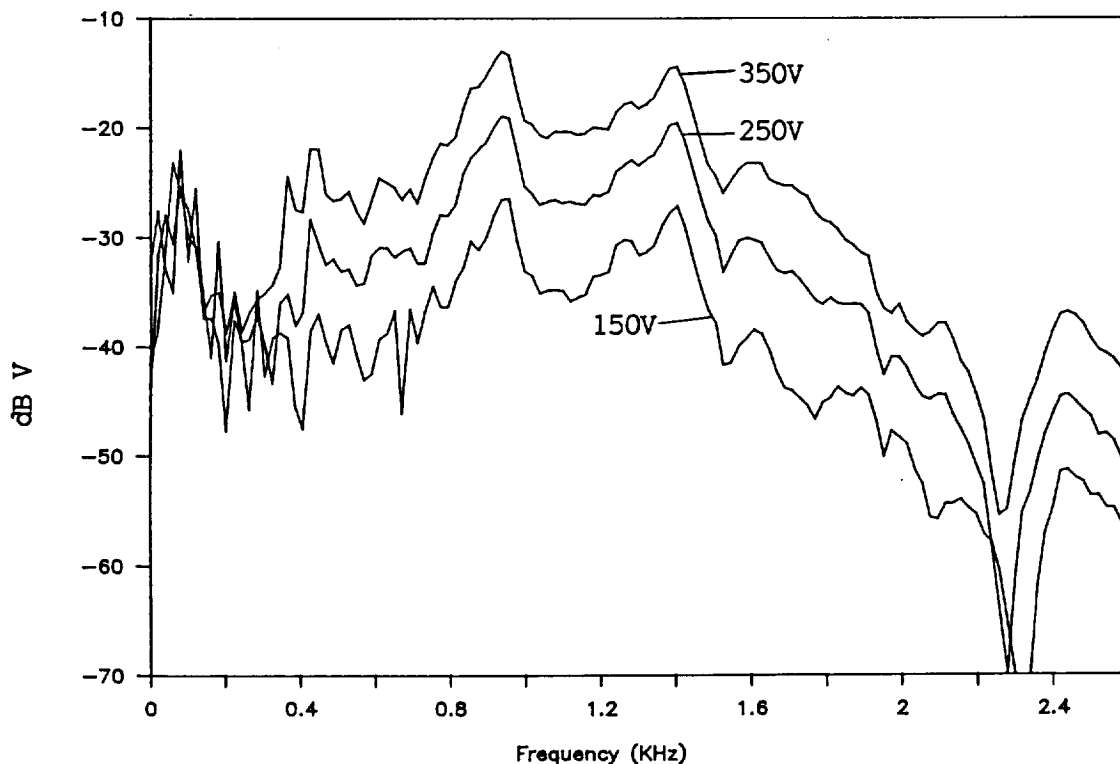
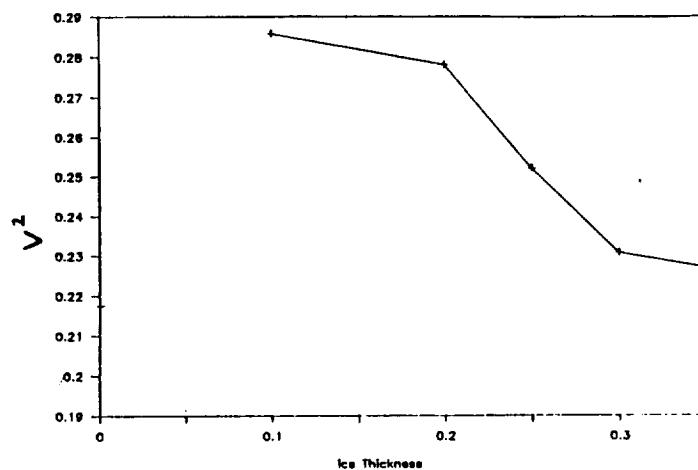
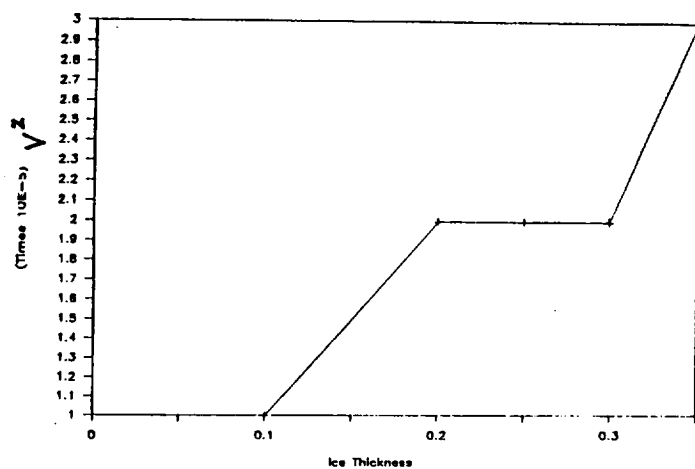
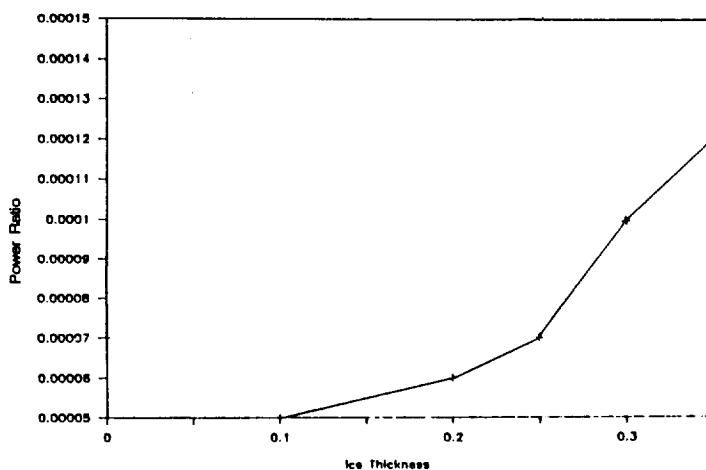


Figure 27. Sensor 1 baseline PSDs for various EIDI excitation voltages acquired during IRA flight tests (no ice).



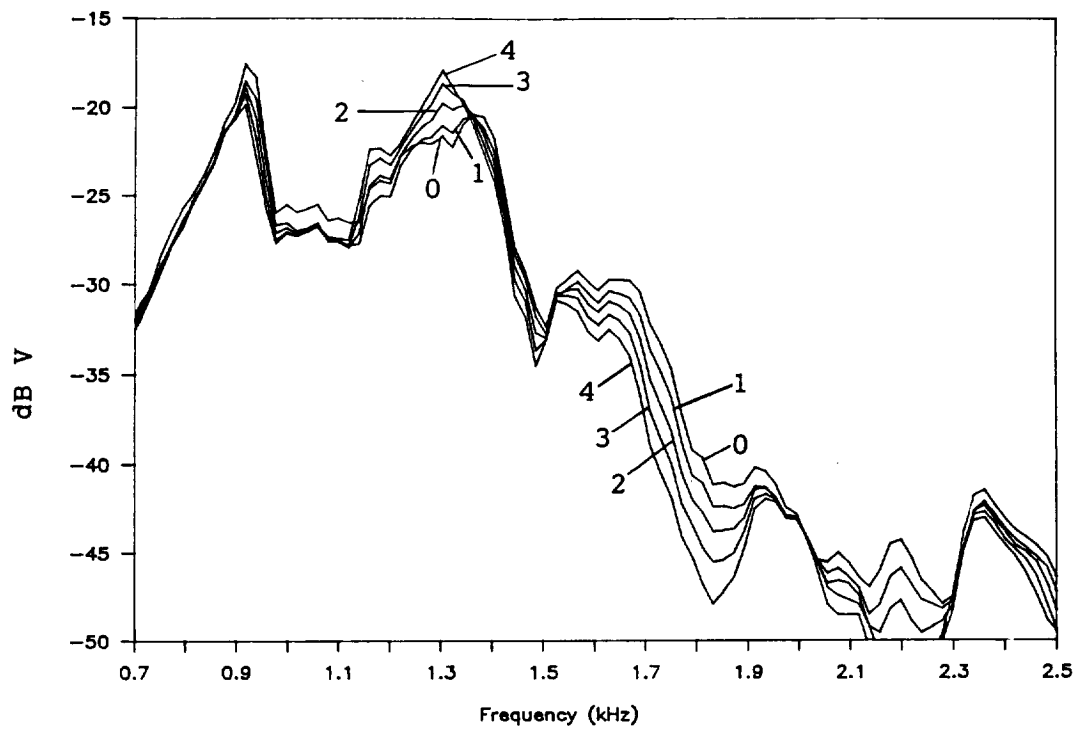
(a) Power in frequency band 0.7 - 1.15 kHz

(b) Power in frequency band 1.8 - 3.0 kHz

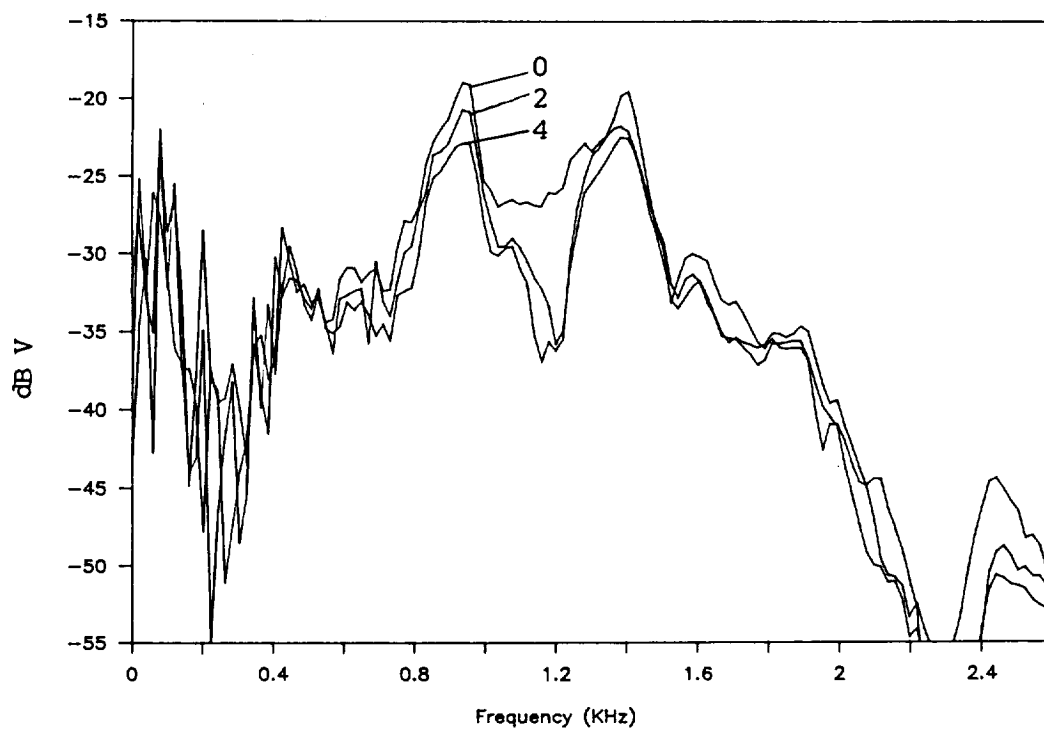


(c) Power ratio.

Figure 28. Selected sensor 4 features vs ice thickness acquired during actual icing flight tests (Test conditions: 100 knots, 5,000' altitude, -6°C, average LWC 0.15).



(a) Ground test.



(b) In-flight test.

Figure 29. Sensor 1 PSD response for simulated leading edge ice using EIDI excitation 250 V.

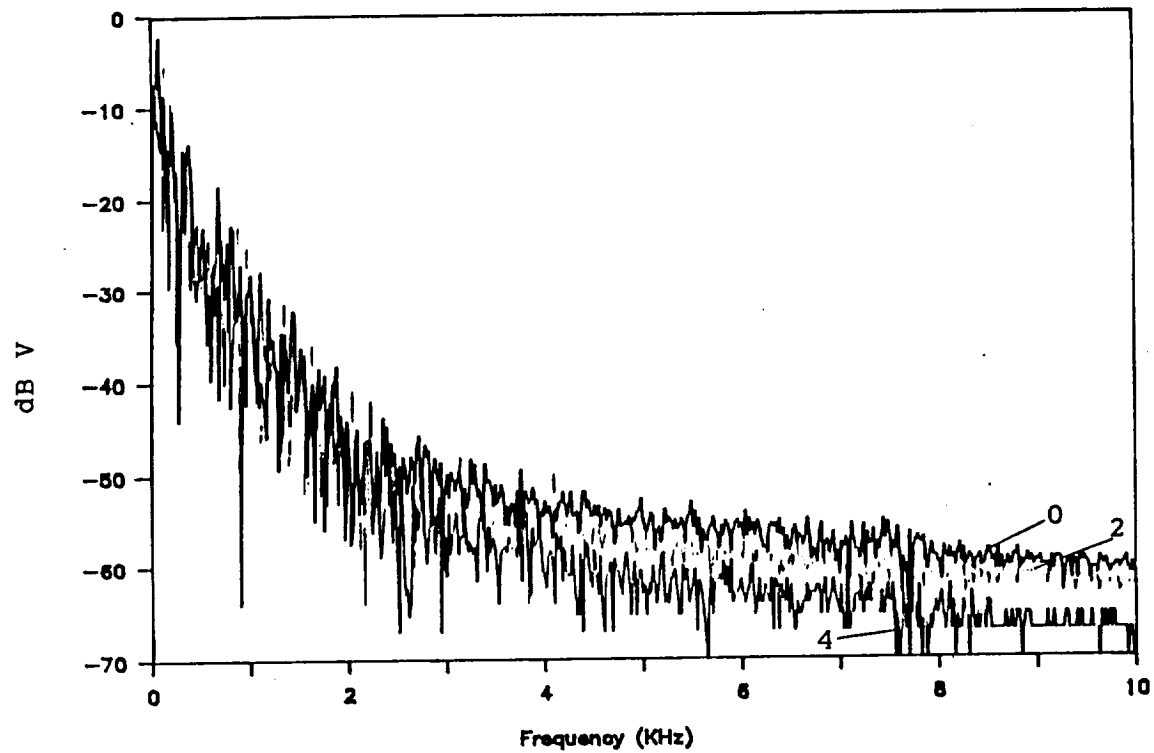


Figure 30. Sensor 1 PSD response for simulated leading edge ice acquired during IRA flight tests (engine vibration excitation: 0, 2, and 4 layers of 0.005 inch aluminum tape).

8 CONCLUSIONS

8.1 System Performance

Initial icing training tests in the IRT showed the system to perform very well using conventional minimum distance pattern recognition algorithms. The system performance was also demonstrated in-flight using simulated leading edge ice accretion. It is expected that refinement of both hardware and software could produce a detector that reliably determines ice thickness and distribution. This system has application as an overall health monitor to indicate the presence of damage within a structure. Several key conclusions were presented:

1. Pattern recognition is a suitable means to measure the ice thickness by detecting the change of the mechanical characteristics of the local structure.
2. The mechanical characteristics of the local structure change significantly with the presence of ice on the leading edge wing structure. The major effects are changes in the system stiffness and shifts in the modal energy distribution.
3. When using the reduced feature set determined by histogram analysis, the sensor demonstrates a 93.3% recognition rate in the IRT for a range of ice thickness from 0.05 to 0.5 inch. The sensor demonstrates a 100% recognition rate during flight tests when trained to recognize 0.005 inch layers of aluminum tape positioned on the leading edge.
4. When the sensor is used in a closed-loop ice protection system, the probability of not activating the deicer when a threshold thickness has been reached is only 0.03% after three measurements.
5. Wide area sensing was shown to be feasible.
6. Electro-expulsive boot is the most practical embodiment of this type of sensor because the boot is external and not as sensitive to changes in the wing structure.

8.2 Future Development

Based on results of the wind tunnel and flight tests, several key areas need to be addressed to enable future development of a practical operational system:

1. Advanced Training Procedure - currently, extensive training is required to teach the pattern recognition software ice thickness signatures over a range of icing conditions. The question arises as to whether the system could be trained by only some

representative patterns, while the missing information could be substituted algorithmically by a proper inter-or extrapolation procedure.

2. Repeatability - the sensor is very sensitive to boundary condition changes. Frequency at which the database must be updated will need to be evaluated. If the system from which the measurements are taken varies with time, a procedure which modifies the decision rule frequently, giving more weight to recent samples, is justified.
3. Reliability - further testing in a wide range of icing conditions is required to determine system reliability. The generation of a large ice database will enable the optimization of the feature set and decision procedure to reduce software processing overhead.
4. False alarms - since the sensor is sensitive to changes of the structure itself, a way of determining whether or not a variation is caused by ice accretion or due to another cause such as a structural fault needs to be determined.

REFERENCES

- (1) Zumwalt, G.W., R.L. Schrag, W.D. Bernhart, and R.A. Friedberg, 1988. "Electro-Impulse De-Icing Testing Analysis and Design," NASA Contractor Report 4175.
- (2) Gerardi, J.J. and P. Dahl, 1986. "Icing Sensor & Ice Protection System," NASA LERC Final Report, Contract #NAS3-24852.
- (3) Gerardi, J.J. and G.A. Hickman, 1989. "Distributed Ice Accretion Sensor for Smart Aircraft Structures," AIAA 27th Aerospace Science Meeting, Reno, Nevada.
- (4) Meisel, W.S., 1972. Computer-Oriented Approaches to Pattern Recognition, Academic Press, New York and London.

APPENDIX A. Fatigue Analysis

Finite Element Model Development - Stress Predictions

A finite element analysis of one bay of the wing cuff with various actuators was performed to study the bending stresses in the aluminum. The following actuators were evaluated: Kimco coil, spar mount eddy-coil and bandaid mount eddy-coil. Based on the results, fatigue life predictions were made. Table 1 is a description of the model parameters. The following assumptions were used in the model:

- Constraints:
- 1) 4 corners fixed (have no degrees of freedom)
 - 2) all other nodes in the boundaries are hinged (have 3 rotational degrees of freedom).
 - 3) all remaining nodes are free (have 3 translational & 3 rotational degrees of freedom).
 - 4) number of nodes: 256.

The eddy coil force input used in the FEM model was derived from data obtained by Wichita State University¹. Skin pressure footprints were analytically obtained for several values of time at various radii for an 800 V impulse using eddy current calculations. The total normal force at the point of application of the eddy coil impulse to the bay was then obtained by finite interval integration as shown in Figure 1. In the Kimco case, because the force time history was not known, displacement data measured from the experimental model was used as input to the FEM model.

Table 1. FEM model of one bay of the wing cuff.

Item	Type of Element	# of Element	Material	Young's Modulus lb/in ²	Poisson's Ratio	Density lb/in ³	Skin Thickness in.
Bay	Shell 4	225	Aluminum	10.5E6	0.3	0.1	0.032
Doubler (EIDI)	Shell 4	9	Aluminum	10.5E6	0.3	0.1	0.05
Doubler (Kimco)	Shell 4	3	Fiberglass	7.0E6	0.3	0.04	0.25

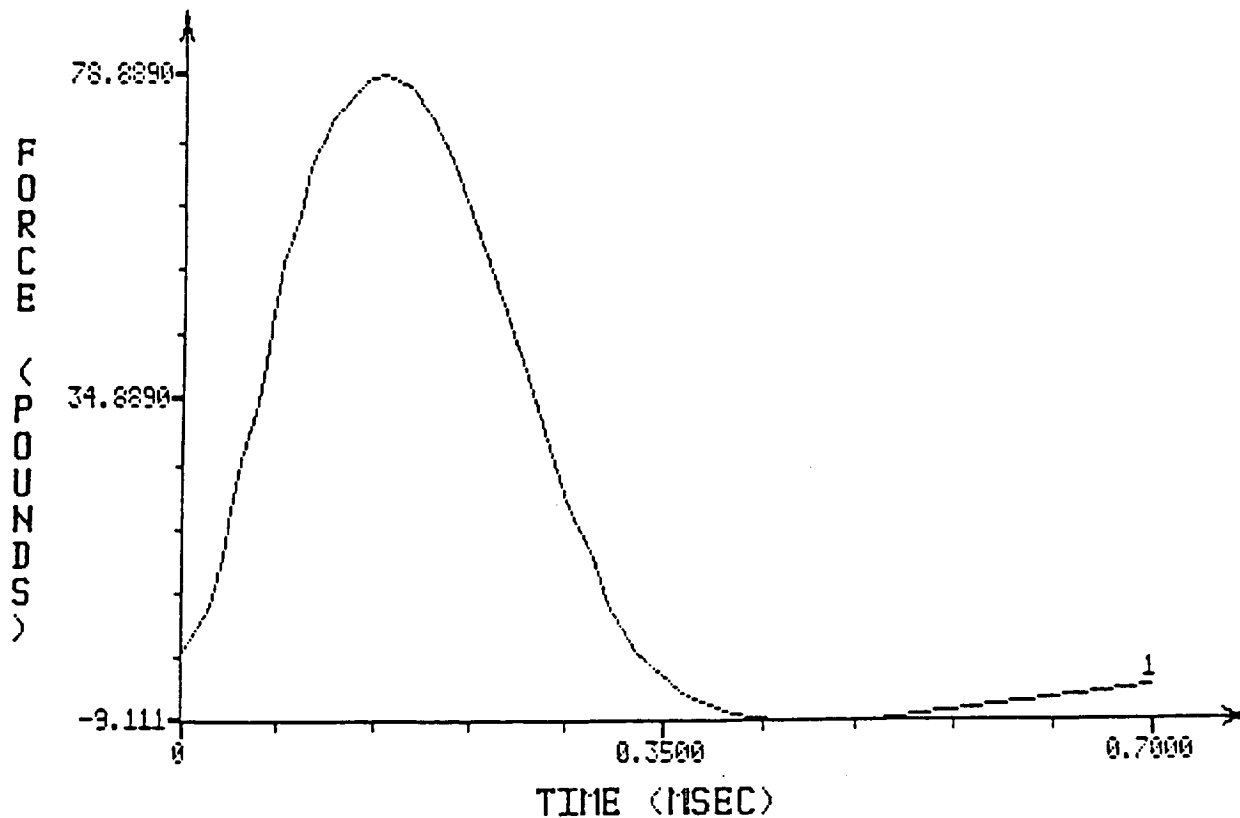


Figure 1. Eddy-coil force at 400 V.

A modal time-history analysis was conducted for a single bay and the normal stresses were studied for each of these actuators. A summary of the results are shown in Table 2 along with results from experimental measurements. The chordwise and spanwise normal stresses at the maximum displacement for the Kimco coil, spar mount eddy-coil, and bandaid mount eddy-coil are shown in Figures 2, 3, and 4, respectively.

Experimental Development - Stress Measurements

A stress survey of the various actuators was made using strain gages placed on the 12.5 inch bay model at the point of application of the input force. To relate strain (ϵ) to stress (σ) the following equations are used

$$\epsilon = 4V_0/V_{BB}GK$$

$$\epsilon_s = \sigma_s/E - \delta\sigma_s/E$$

$$\epsilon_c = \sigma_c/E - \delta\sigma_c/E$$

where

V_{BB} = Bridge voltage = 10 V
 G = Gain = 100
 K = 2.08
 δ = Poisson Ratio = 0.3 for Al
 E = Young's Modulus = 10×10^6 psi for Al
 s = spanwise direction
 c = chordwise direction

The following assumptions were used in the analysis:

- 1) Strain gages aligned with primary axis
- 2) Spanwise and chordwise max strains co-located
- 3) ϵ_s and ϵ_c in phase

The AC Kimco had high stress levels at resonance (129 Hz). The pulsed Kimco (250 Volts/1250 uF) had lower stress levels and slower response time (milliseconds instead of microseconds) as compared to the EIDI actuator, and thus lower acceleration. This may be an important factor in deicing efficiency. The experimental stress results compare well with the analytical predictions.

Model Description	Maximum Displacement (inches)	Normal Stress Spanwise (kpsi)	Normal Stress Chordwise (kpsi)	Life Prediction (10^6 cyc)*
Kimco Coil (AC)	0.12/0.12	25/26	44/40	0.03
Kimco Coil (Pulsed)	- /0.07	- /14	- /18	10
Eddy Coil (Span Mount)	0.09/0.10	18/20	36/35	0.13
Eddy Coil (Bandaidd Mount)	0.04/ -	7/10	12/14	42

* Endurance Stress Level (AL) = 20,000 psi at 5×10^6 cycles

TABLE 2. Analytical/experimental stress comparisons.

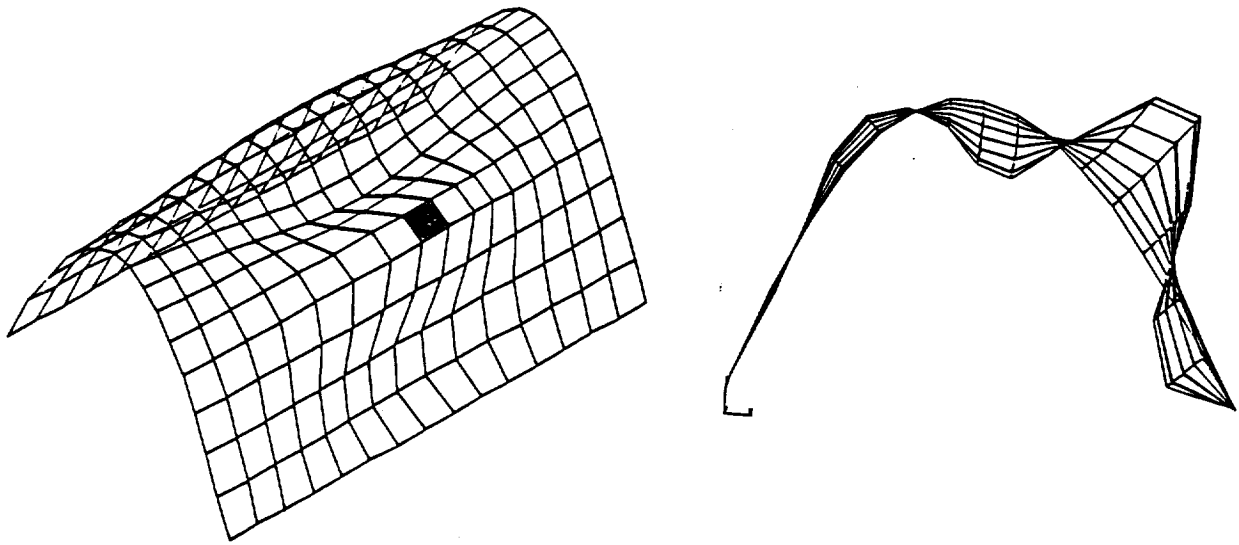


Figure 2. (a) Kimco Coil - Deformed shape - maximum displacement = 0.12 inch.

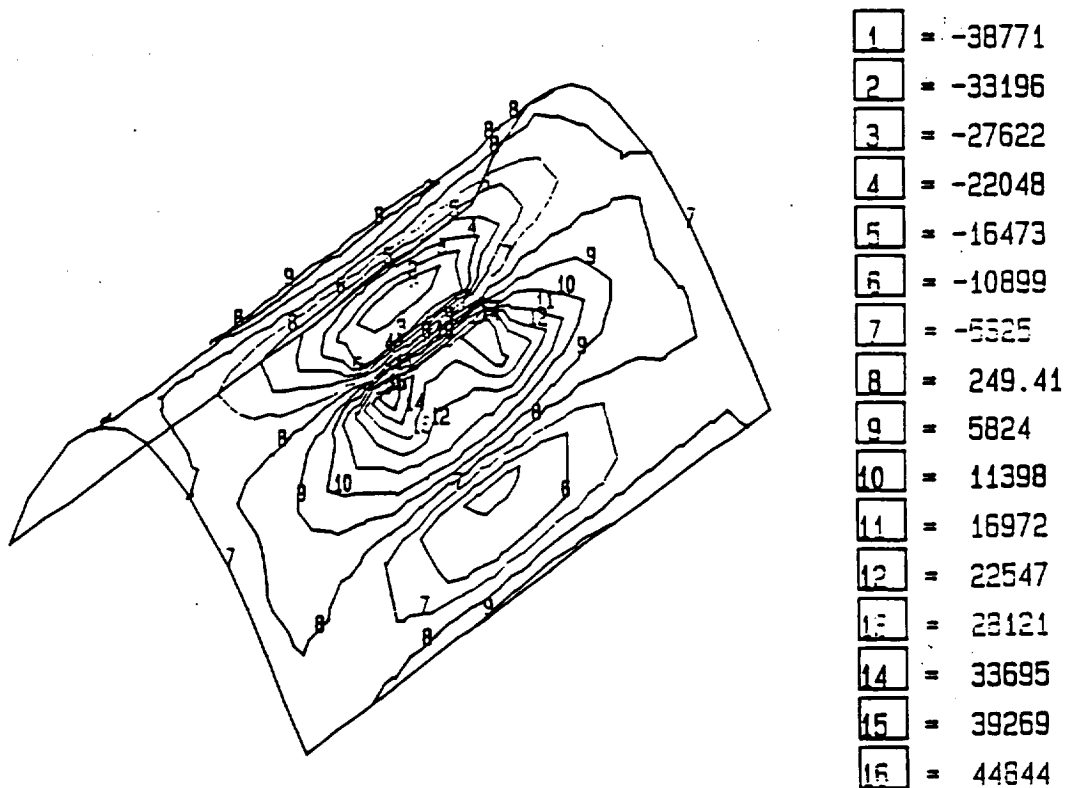


Figure 2. (b) Kimco Coil - Chordwise normal stress induced in one bay of the wing cuff.

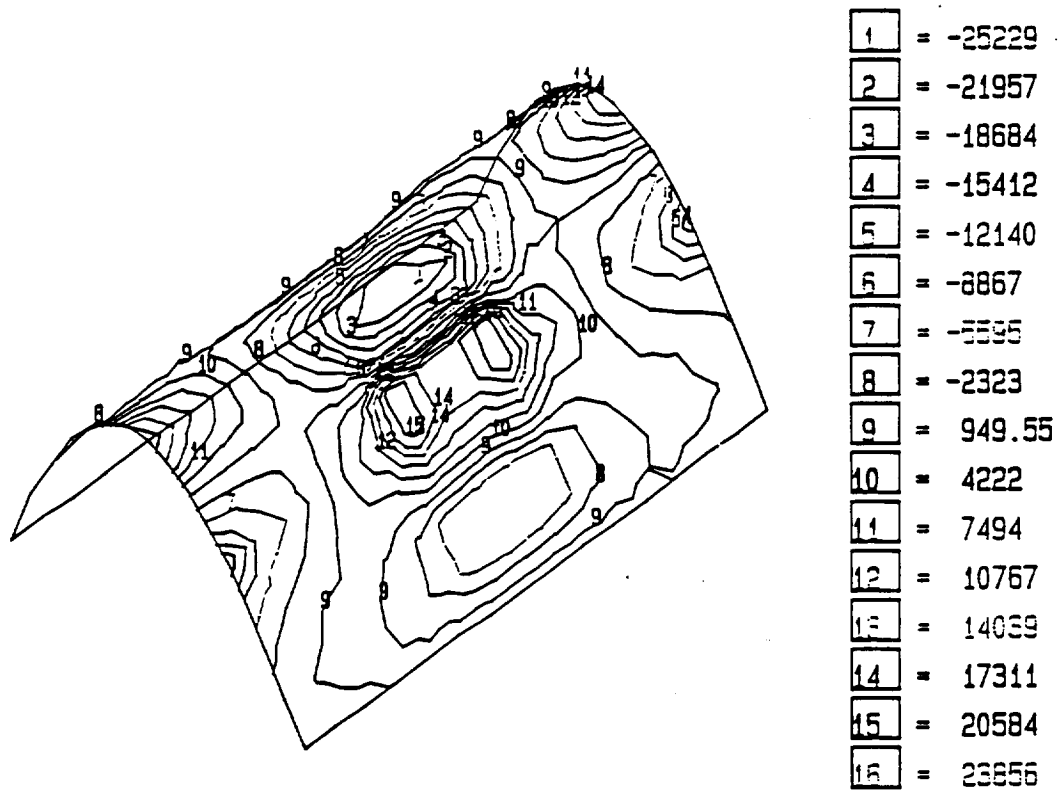


Figure 2. (c) Kimco Coil - Spanwise normal stress induced in one bay of the wing cuff.

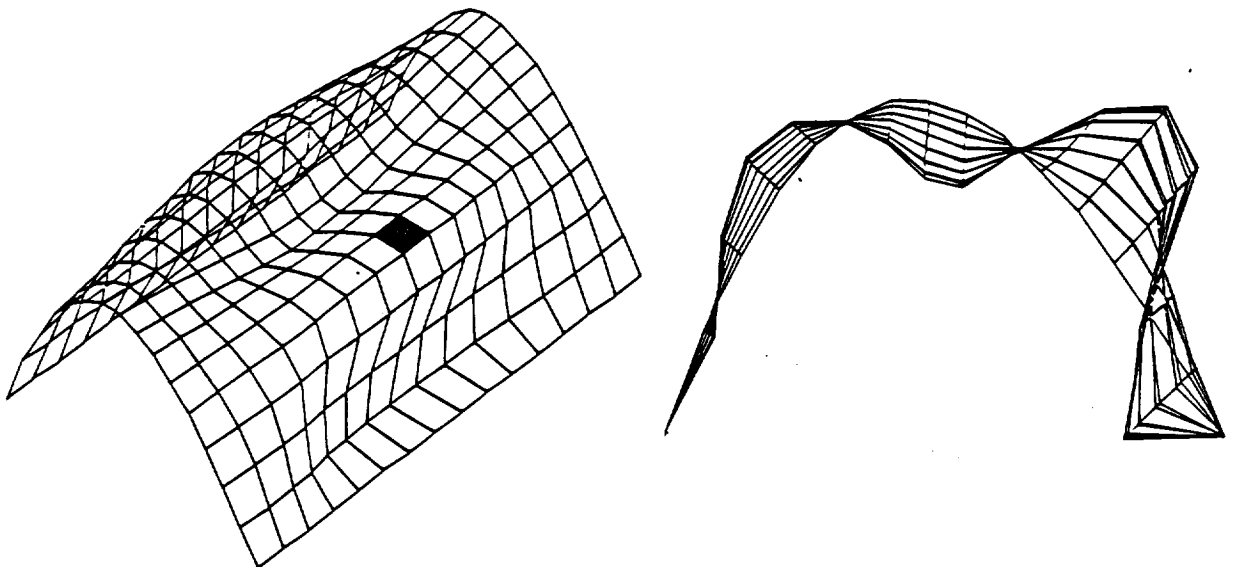


Figure 3. (a) Eddy-Coil (Spar Mount) - Deformed shape - maximum displacement = 0.09 inch.

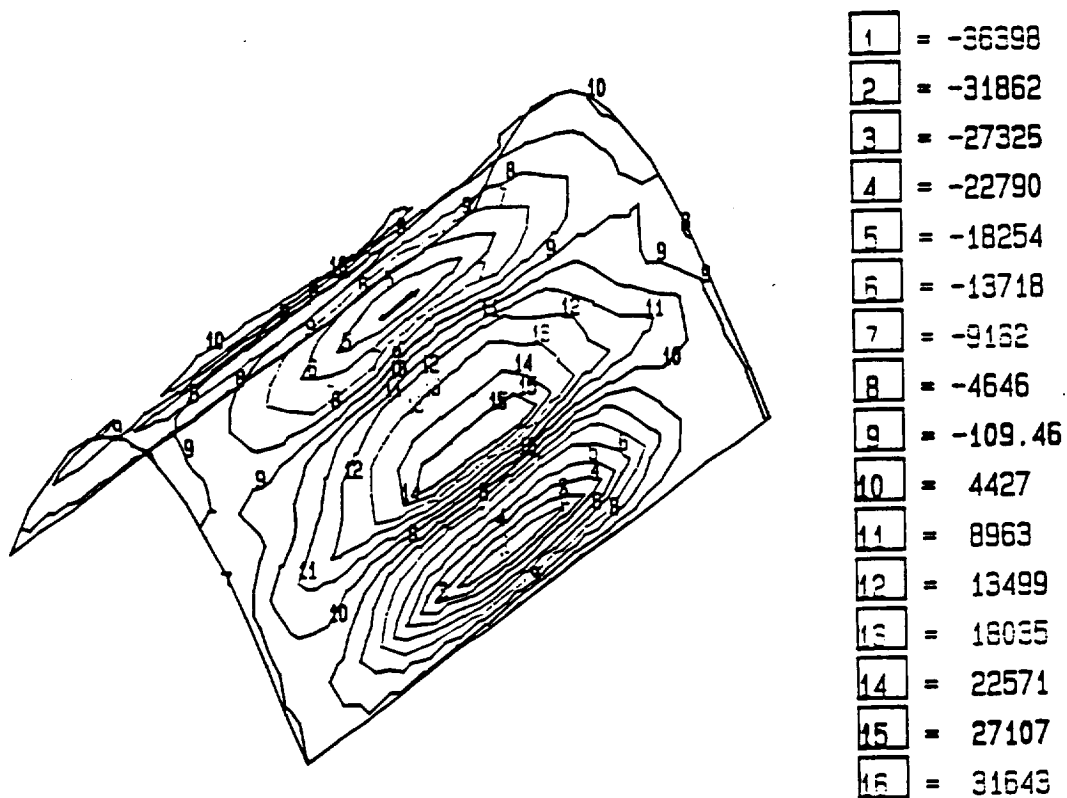


Figure 3. (b) Eddy-Coil (Spar Mount) - Chordwise normal stress induced in one bay of the wing cuff.

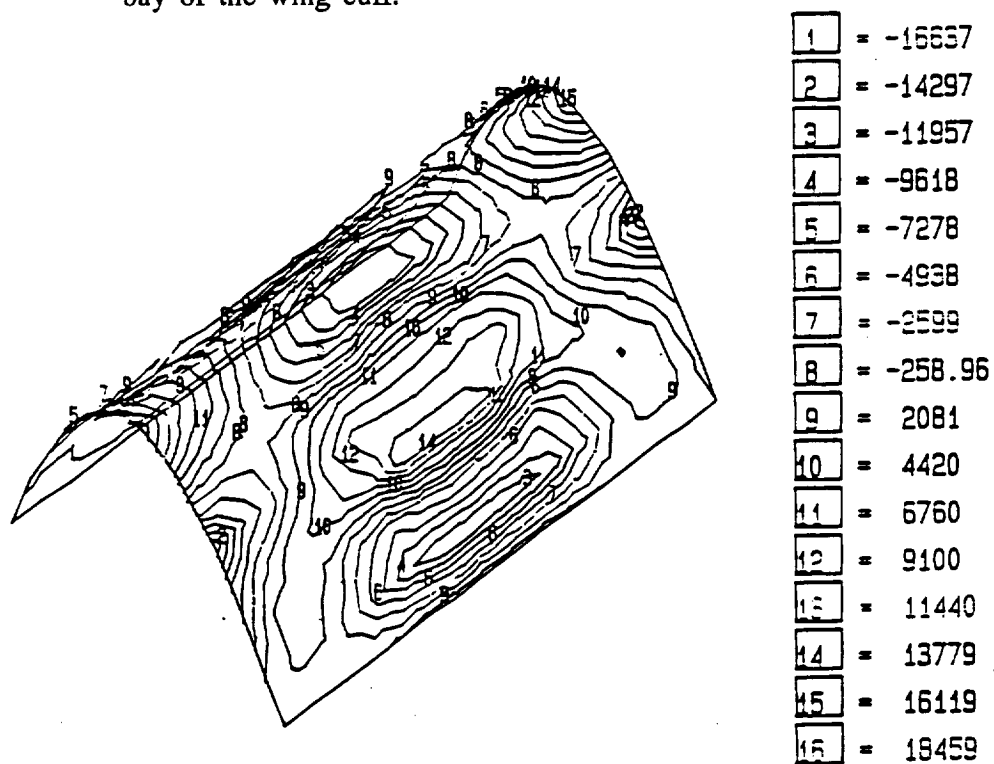


Figure 3. (c) Eddy-Coil (Spar Mount) - Spanwise normal stress induced in one bay of the wing cuff.

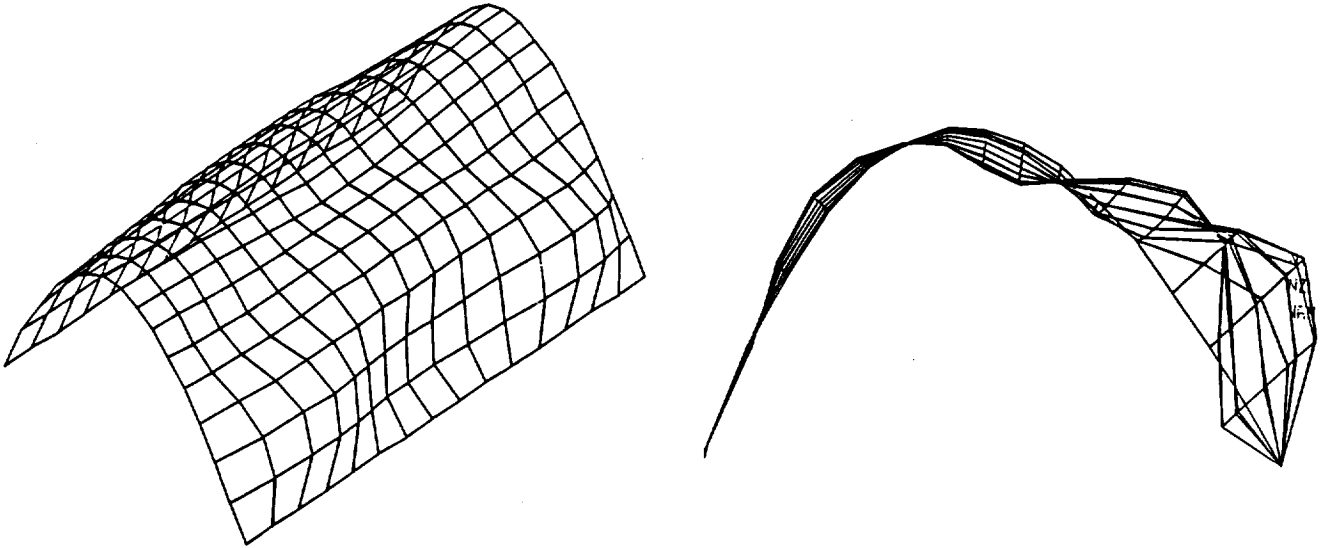
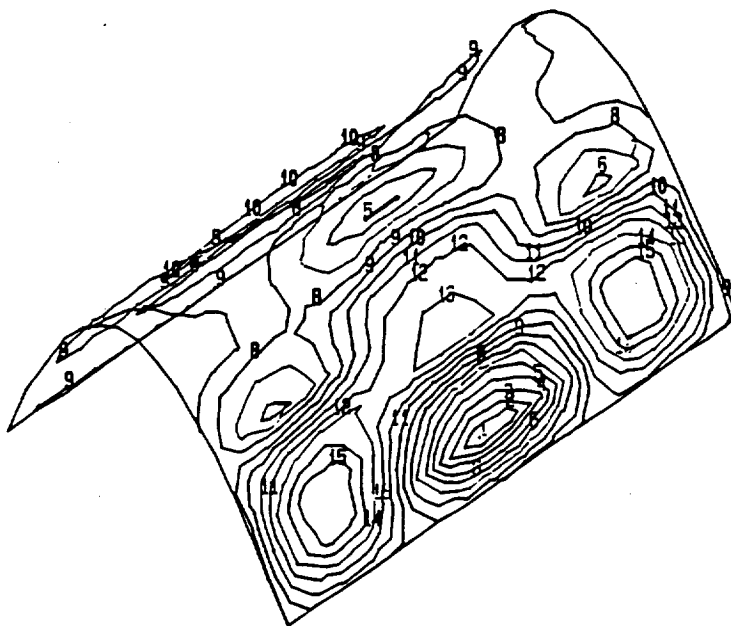


Figure 4. (a) Eddy-Coil (Bandaidd Mount) - Deformed shape - maximum displacement = 0.036 inch.



1	= -12186
2	= -10656
3	= -9125
4	= -7594
5	= -6064
6	= -4533
7	= -3003
8	= -1472
9	= 58.448
10	= 1589
11	= 3120
12	= 4650
13	= 6181
14	= 7711
15	= 9242
16	= 10772

Figure 4. (b) Eddy-Coil (Bandaidd Mount) Chordwise normal stress induced in one bay of the wing cuff.

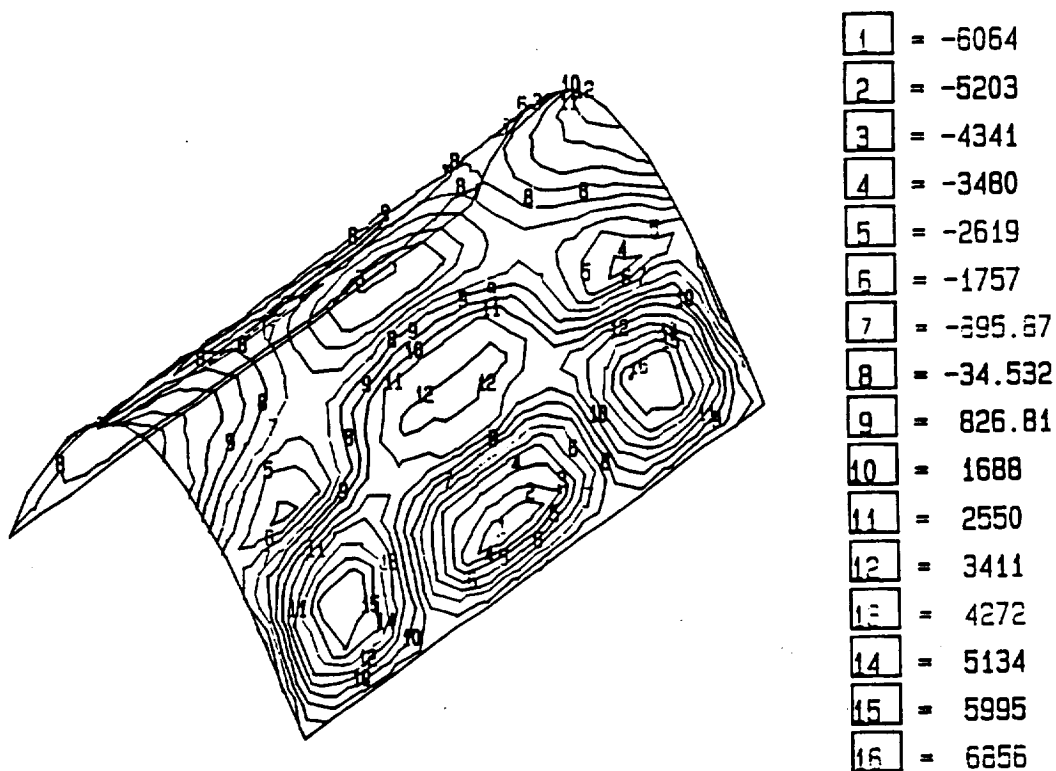


Figure 4. (c) Eddy-Coil (Bandaaid Mount) Spanwise normal stress induced in one bay of the wing cuff.

Fatigue Life Calculations

Fatigue life predictions were made based on Marin's cumulative damage theory,

$$n_2/n_1 = (S_1/S_2)^y$$

where

n_2 = # of cycles of operations at reference stress S_2 to produce damage equivalent to n_1 cycle at stress level S_1 .

n_1 = actual # of cycles of operation at stress level S_1 .

S_1 = actual operating stress level at which damage is produced.

S_2 = endurance limit for aluminum.

y = material constant.

- 1) Endurance limit for Al 2024-T3 is 20,000 psi for 5×10^6 cycles.
- 2) Material constant for Al 2024-T3 is 6.
- 3) Principal stress directions coincide with spanwise and chordwise normal stress direction.

The life predictions were made using the maximum stress values obtained from the FEM analysis and the experimental test results. Table 1 is a tabulation of the results. As can be seen, the bandaid mount eddy coil as compared to the other actuators has the longest predicted life.

APPENDIX B. Structural Dynamic Studies

Finite Element Analysis

The overall objective of this analysis was to obtain a realistic model of the leading edge of the DHC-6 wing as a function of ice buildup in order to augment experimental test results. The model was used to determine the optimal sensor/EIDI coil configuration and to determine the effects of ice accretion on the structural vibration response. A modal analysis was performed to extract the natural frequencies of one bay of the leading edge wing cuff. Analytical results were then compared to experimental results.

Figure 1 shows the finite element grid structure of one bay of the wing cuff. The bay was modeled using 225 (15 rows of elements chordwise by 15 rows of elements spanwise) SHELL4 elements. These are 4 noded quadrilateral thin shell elements with membrane and bending capabilities for the analysis of three dimensional structural modes. Six degrees of freedom (3 translational and 3 rotational) were considered for each node. The ice was modeled using eight noded three dimensional SOLID elements. Three translational degrees of freedom were considered for each node. The doubler was modeled using 9 (3 chordwise by 3 spanwise) SHELL4 elements. The 4 oz of coil weight were evenly distributed over the 16 grid points at the center of the coil mounting and the 1 oz fiber glass weight was distributed uniformly over 32 grid points over the doubler area.

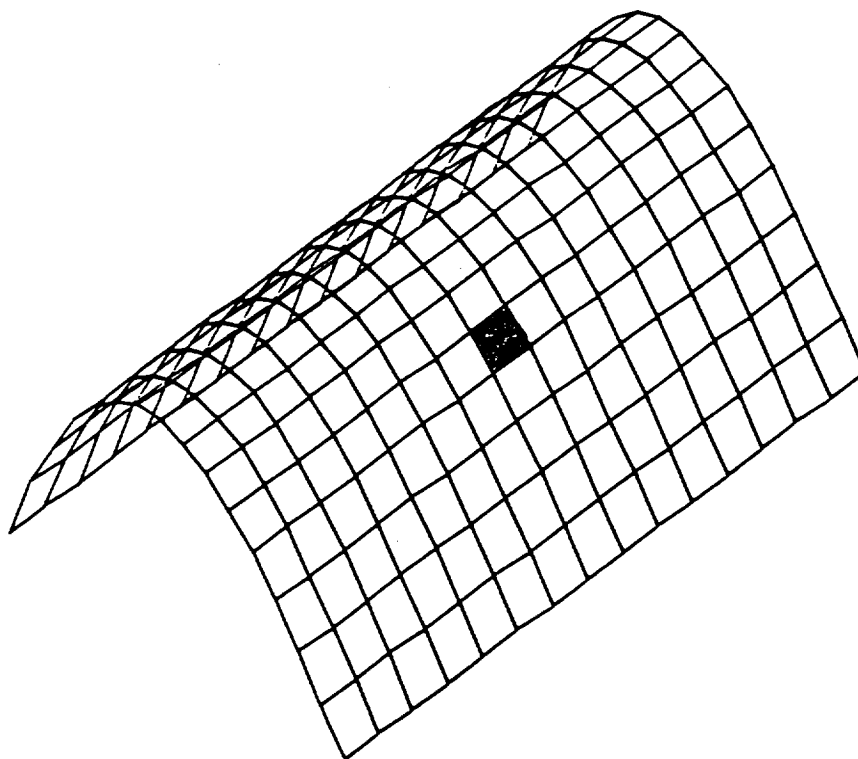


Figure 1. Finite element grid of single bay of the wing.

A pinned/hinged boundary condition with clamped corners was used. Thus, all the nodes at the boundary except the four corners, representing the aluminum bay, had three rotational degrees of freedom. The four corners were totally constrained. The mass inertia effect was neglected in the rotational x direction. This boundary condition gave a best match of the first five modes of the actual wing cuff. Table 1 is a description of the model parameters.

The COSMOS/M finite element program was used to conduct a normal modes vibration analysis on a PC 80286 computer. Typical execution times were 2-3 hours per run.

The first five frequencies were extracted for five cases which corresponded to ice thicknesses of 0, 1/4, 1/2, and 1 inches of ice. These frequencies are given in Table 2. From the table of frequencies, it is seen that the primary effect of adding the ice was to stiffen up the shell and thus raise the vibratory frequencies.

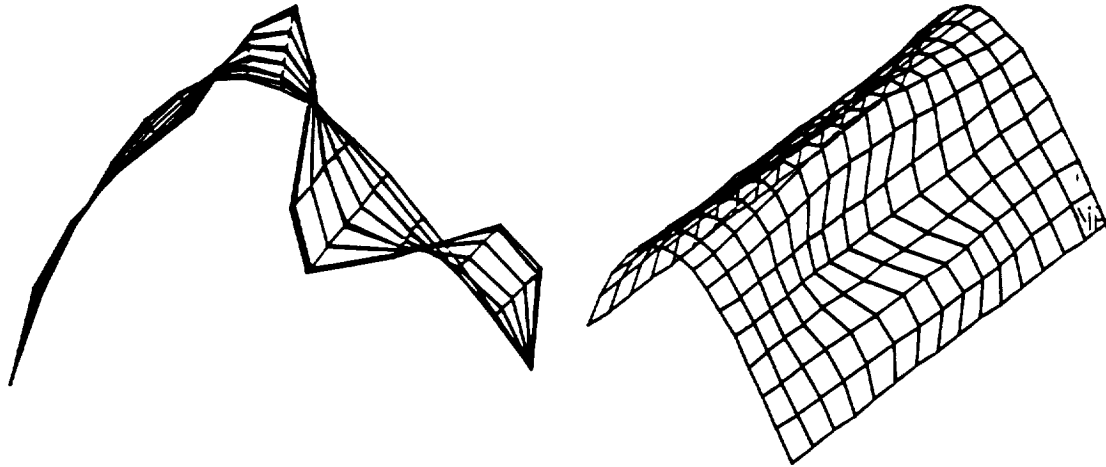
TABLE 1. FEM model of one bay of the wing cuff.

Item	Type of Element	# of Element	Material	Young's Modulus lb/in ²	Poisson's Ratio	Density lb/in ³	Skin Thickness in.
Bay	Shell 4	225	Aluminum	10.5E6	0.3	0.1	0.032
Doubler (EIDI)	Shell 4	9	Aluminum	10.5E6	0.3	0.1	0.05
Ice	Solid	60	Ice	1.0E6	0.3	0.036	0 - 1

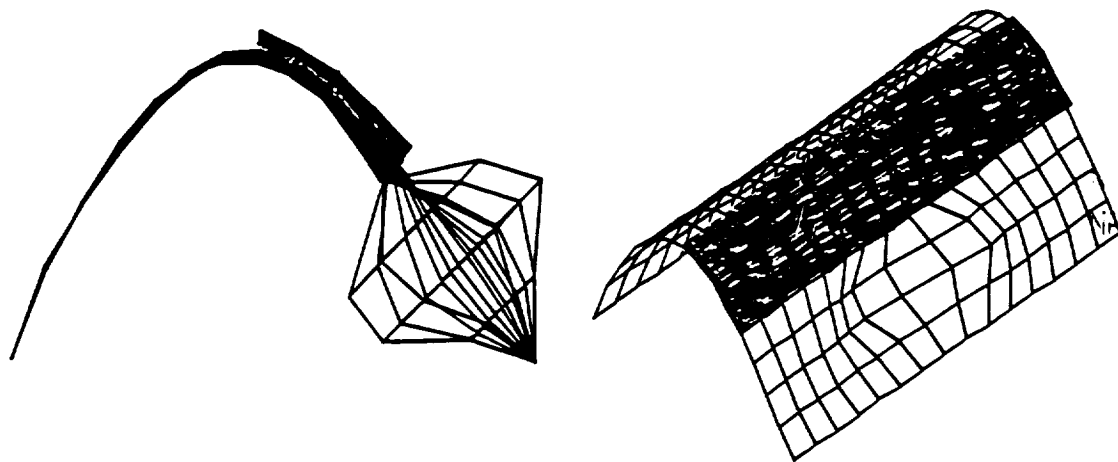
TABLE 2. Effect of ice accretion on the mode frequencies of a single bay of the wing cuff.

	Ice (in)	Mode#1 (Hz)	Mode#2 (Hz)	Mode#3 (Hz)	Mode#4 (Hz)	Mode#5 (Hz)
Analytical	0.0	207	266	323	381	393
	0.25	276	354	369	415	447
	0.5	281	359	410	444	456
	1.0	290	362	412	447	458
Experimental	0.0	215	271	327	378	430

Mode shape plots were done of each case with a plan view and three dimensional view for each ice condition. The coil and doubler were not plotted since they tend to obscure the picture, however it is obvious from the shape of the deformed shell that the coil mounting is acting almost as a rigid body while the doubler tends to stiffen the leading edge locally. Typical mode shape plots are shown in Figure 2 for the no ice and 1/4 inch ice case.



(a) No ice



(b) 0.25 inch ice

Figure 2. Mode shape plot of bay with band-aid coil mount.

Experimental Tests

Experimental studies were carried out to verify the analytical model. A block diagram of the experimental setup is shown in Figure 3. A model of one bay of the wing cuff was fabricated from 0.032 inch thick 2024 aluminum. The boundaries were rigidly bolted to a support aircraft structure. A single band-aid mount EIDI eddy coil located mid-length on the stagnation line provided the sensor excitation source. The coil was pulsed with 150 volts at a frequency of 0.5 Hz. The sensor used in the study was a single strip of 0.28 μm thick Kynar PVDF film, 12.5 inches in length and 1 inch wide. It was bonded to the surface of the test model, spanwise along the stagnation line, under the location of the ice buildup. The signal was fed into an impedance match circuit and then into the dynamic signal analyzer. Because the signal to noise ratio in the lab environment was greater than 50, no amplification was required.

The modal survey of the wing cuff leading edge is shown in Figure 4. The first five natural frequencies (215 to 430 Hertz) were in agreement with the finite element solution with an error of less than 9%, indicating the equivalence of the model and test article.

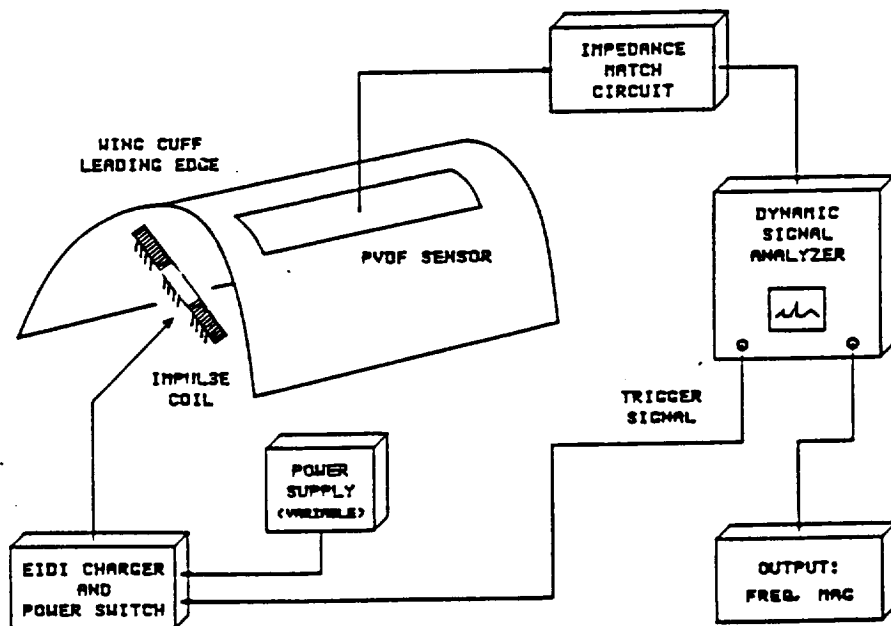


Figure 3. Experimental test set-up.

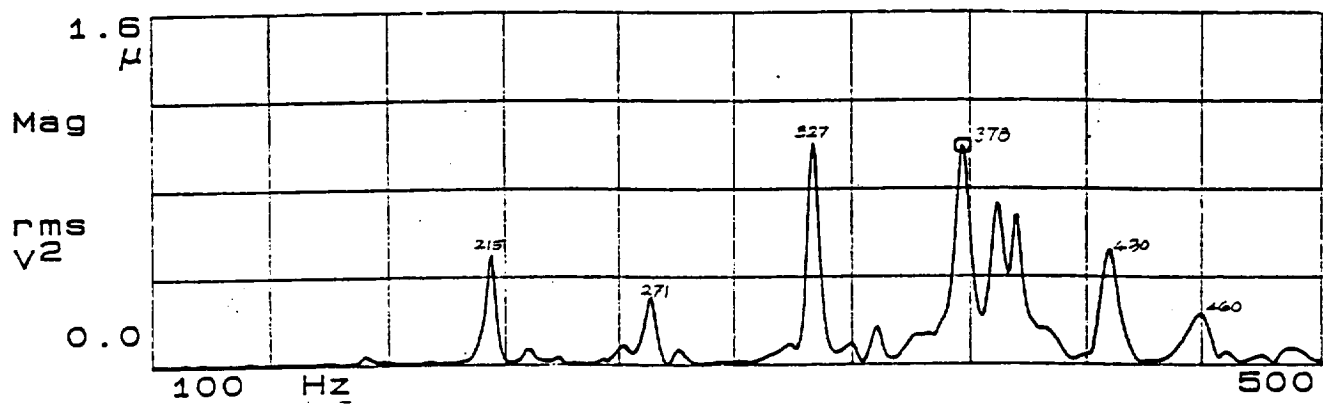
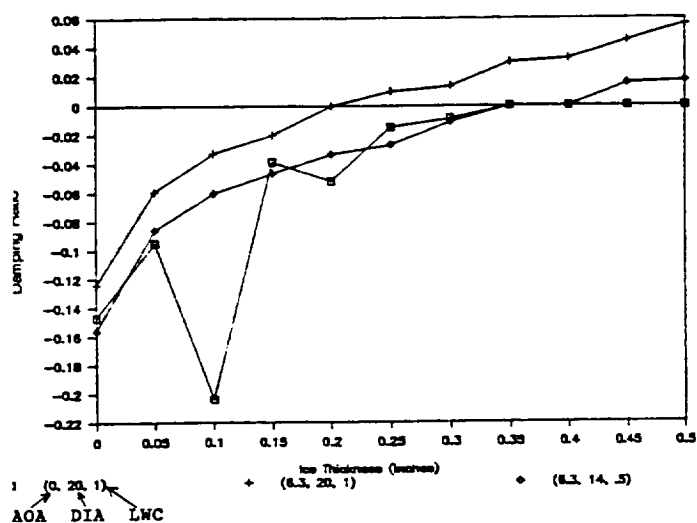
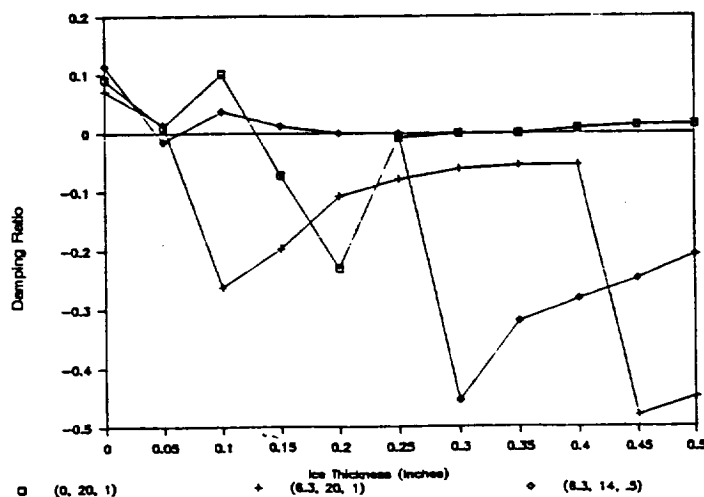


Figure 4. Modal Survey of Wing Cuff Leading Edge

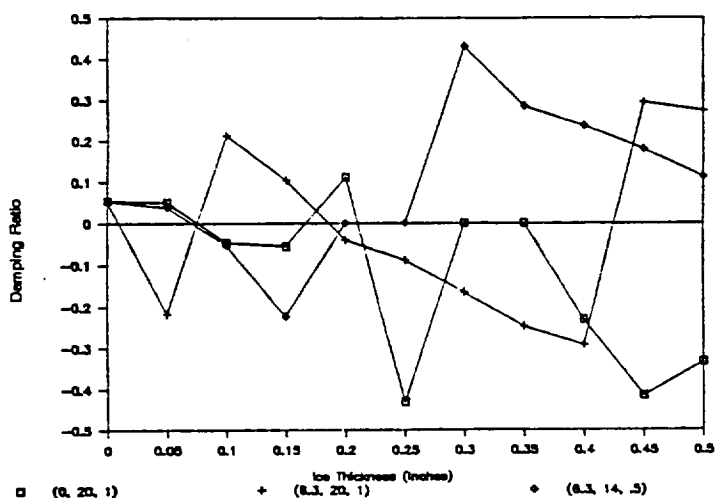
APPENDIX C: Features Generated During the IRT Tests



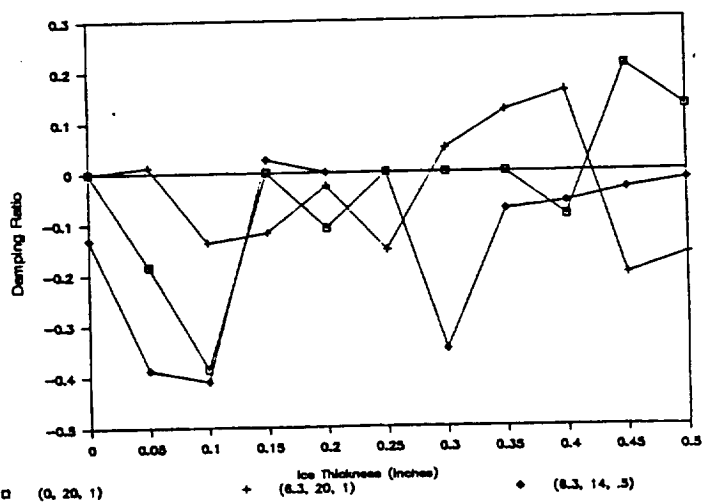
(a) First Local Damping



(b) Second Local Damping



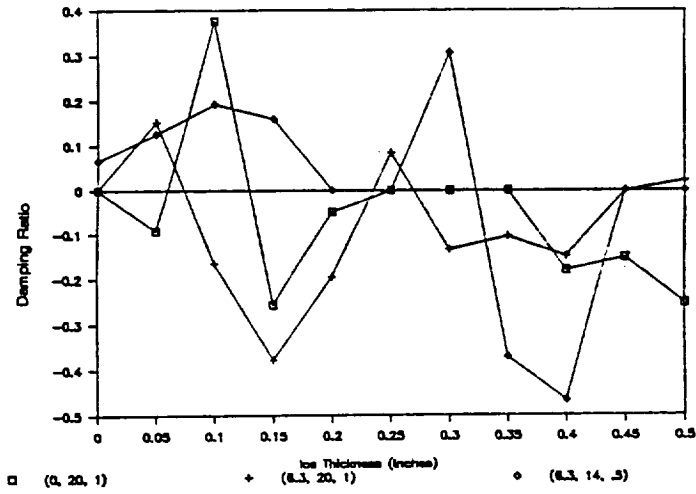
(c) Third Local Damping



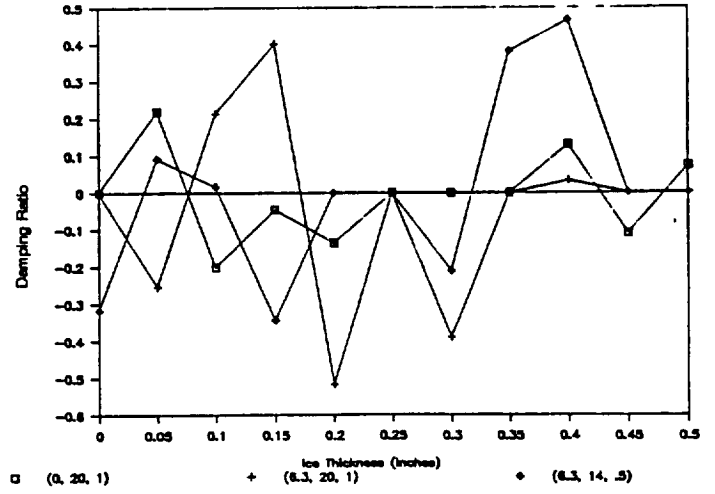
(d) Fourth Local Damping

Figure 1 - Sensor 1 Test Conditions: -1°C , variable AOA, DIA, & LWC

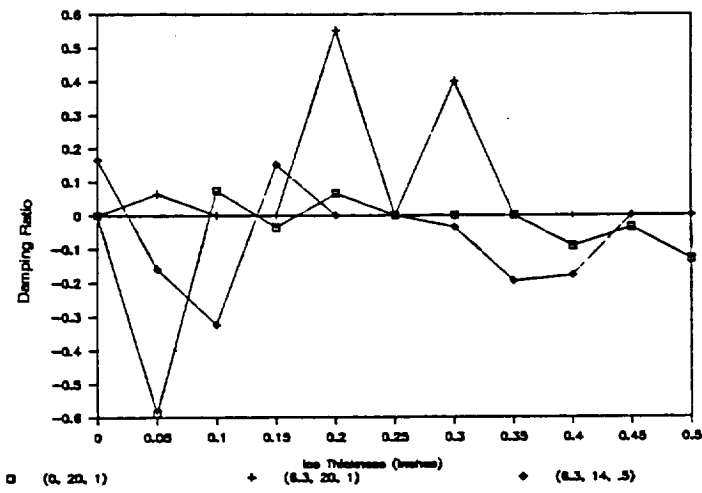
Figure 1 - Continued



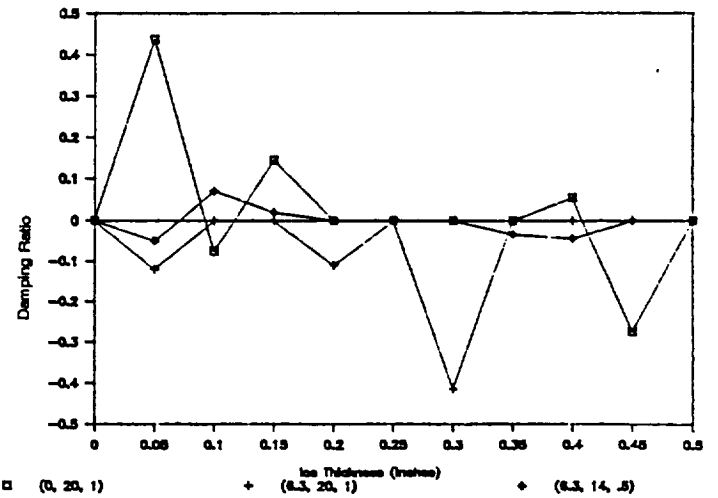
(e) Fifth Local Damping



(f) Sixth Local Damping

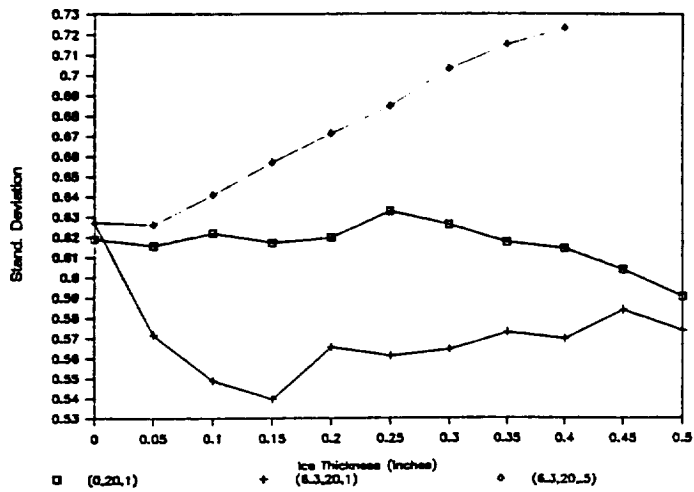


(g) Seventh Local Damping

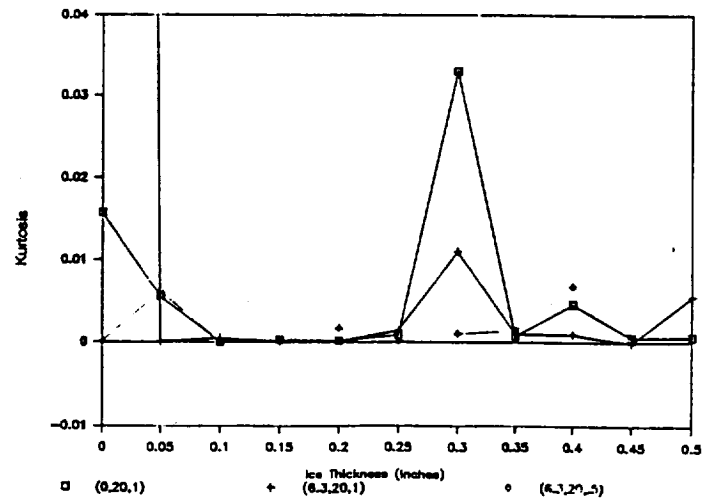


(h) Eighth Local Damping

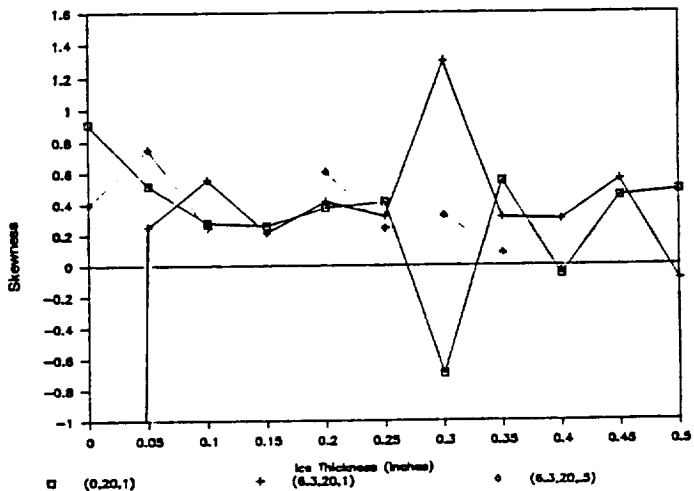
Figure 1 - Continued



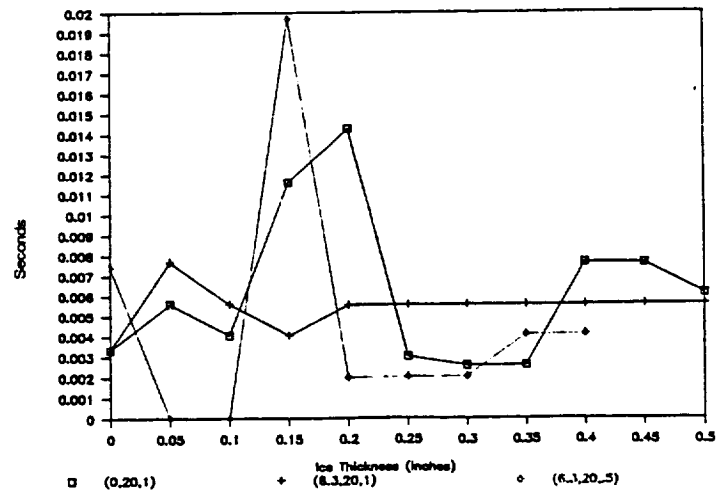
(i) Standard Deviation



(j) Kurtosis

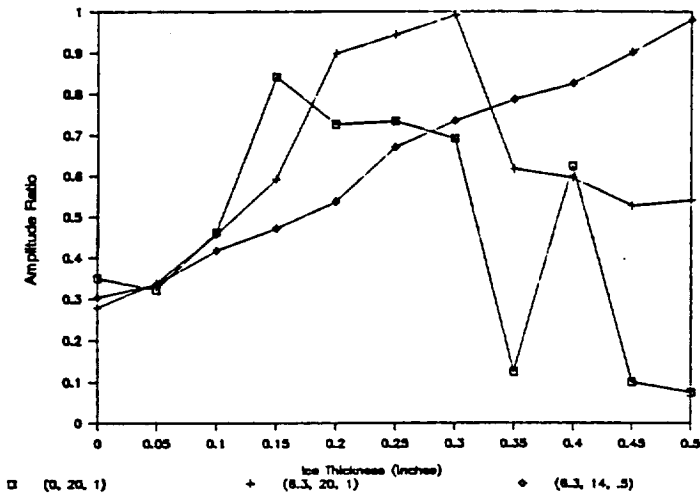


(k) Skewness

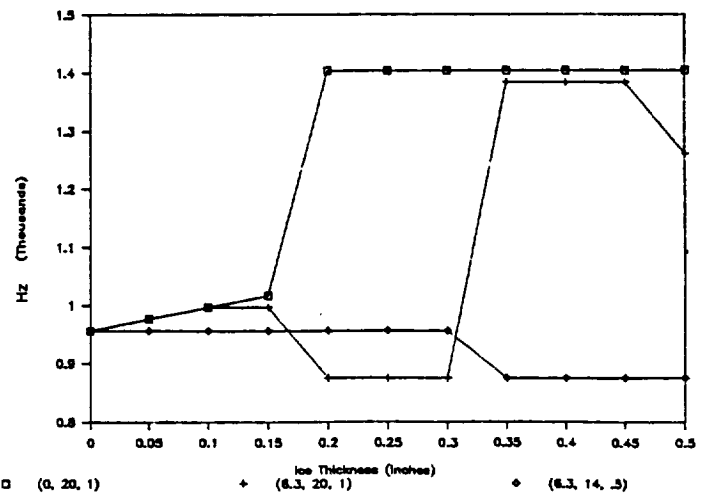


(l) Time at 90% Decay

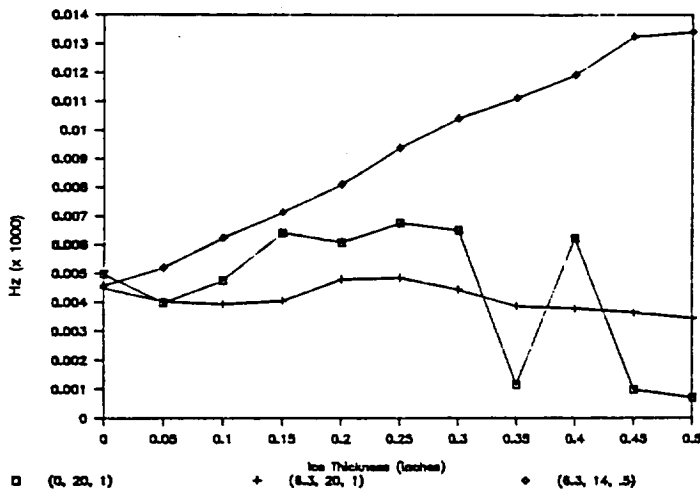
Figure 1 - Continued



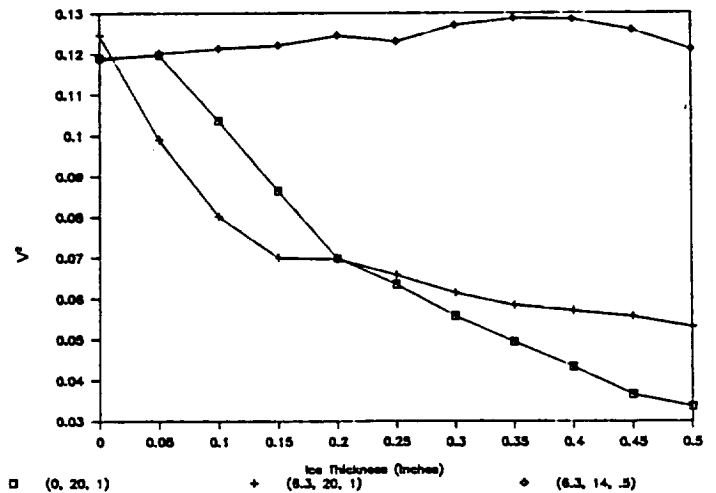
(m) Amplitude Ratio of 2 Biggest Peaks



(n) Biggest Peak Frequency

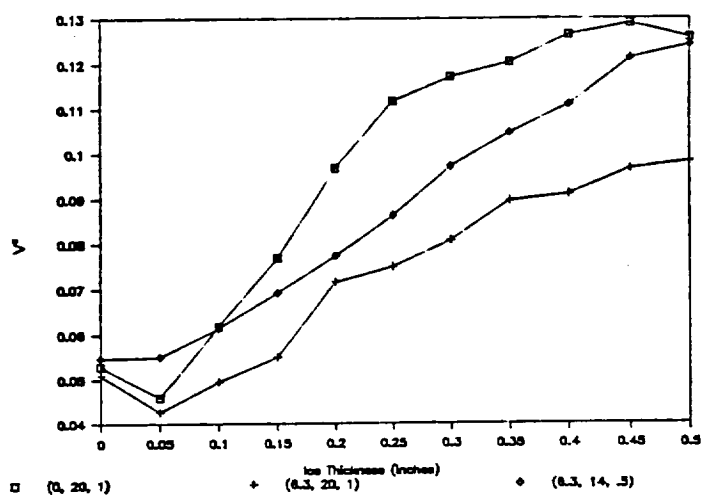


(o) Freq Difference of 2 Biggest Peaks

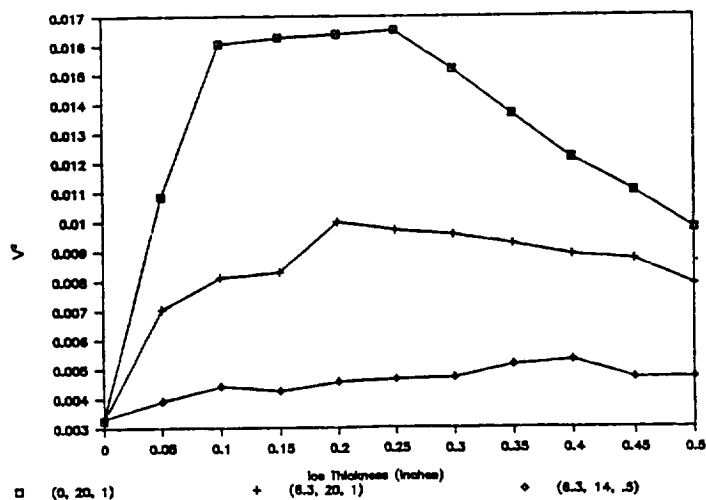


(p) Power in Freq Band 700-1150 KHz

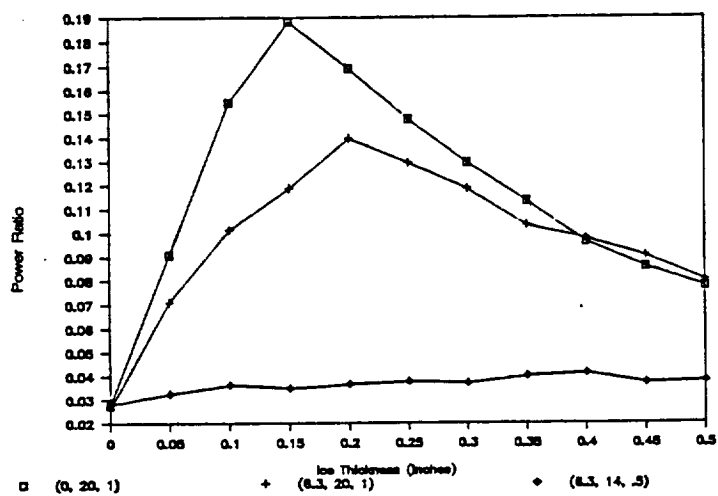
Figure 1 - Continued



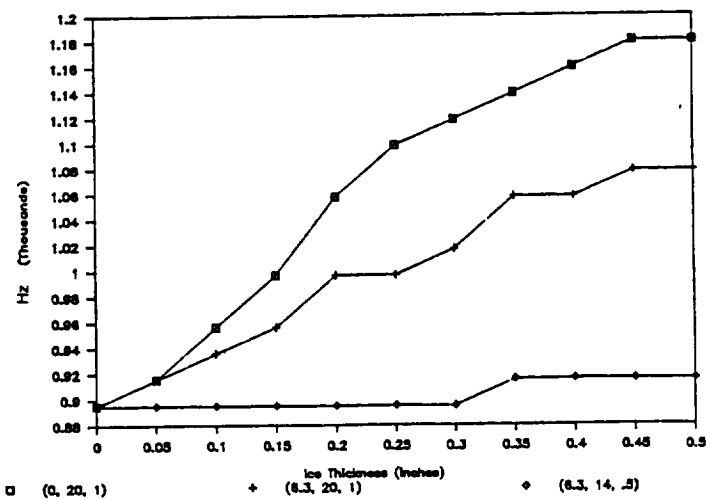
(q) Power in Freq Band 1150-1800 KHz



(r) Power in Freq Band 1800-3000 KHz

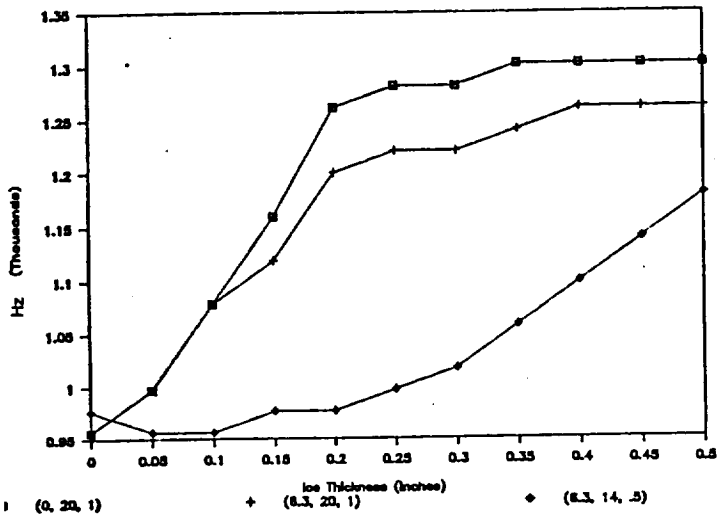


(s) Ratio of Smallest & Largest Power

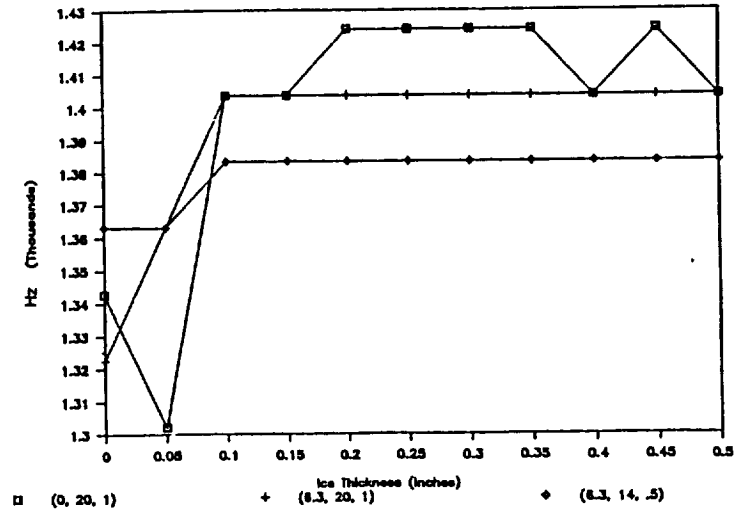


(t) Frequency with 25% of Energy

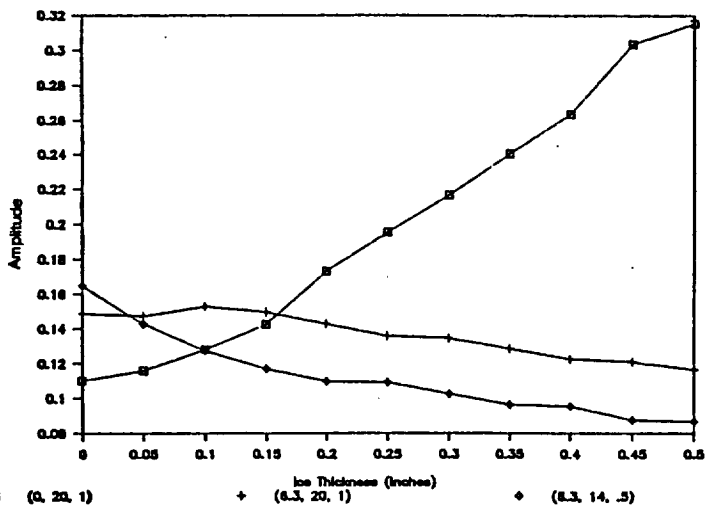
Figure 1 - Concluded



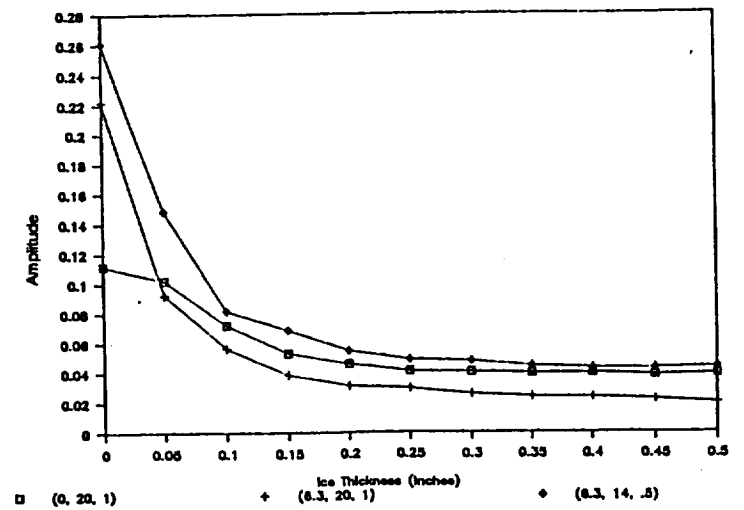
(u) Frequency with 50% of Energy



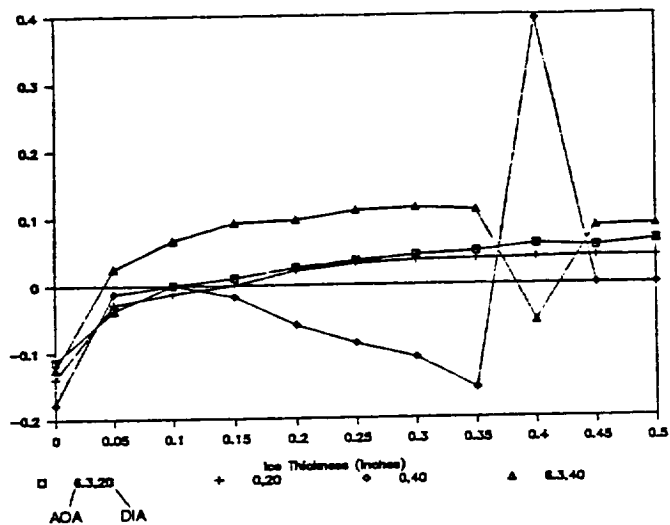
(v) Frequency with 75% of Energy



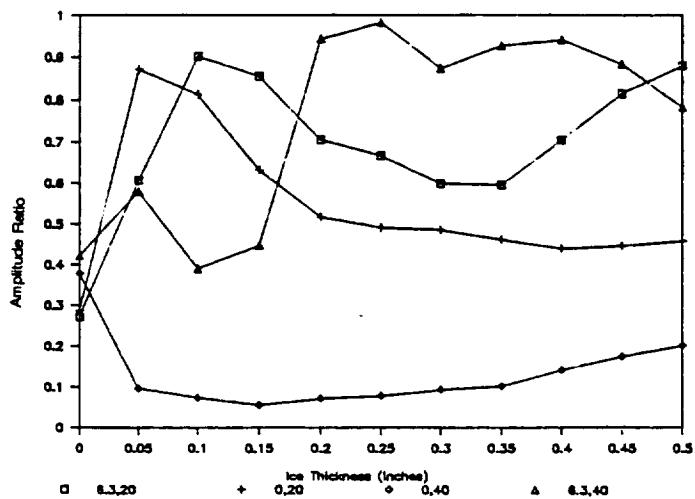
(w) Transfer Function 1



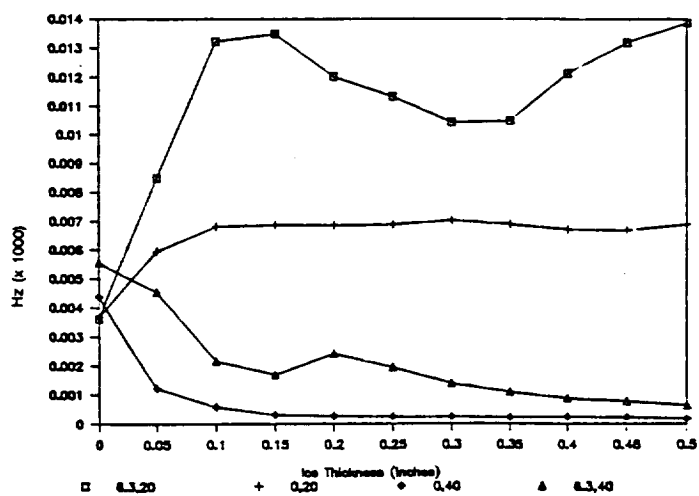
(x) Transfer Function 2



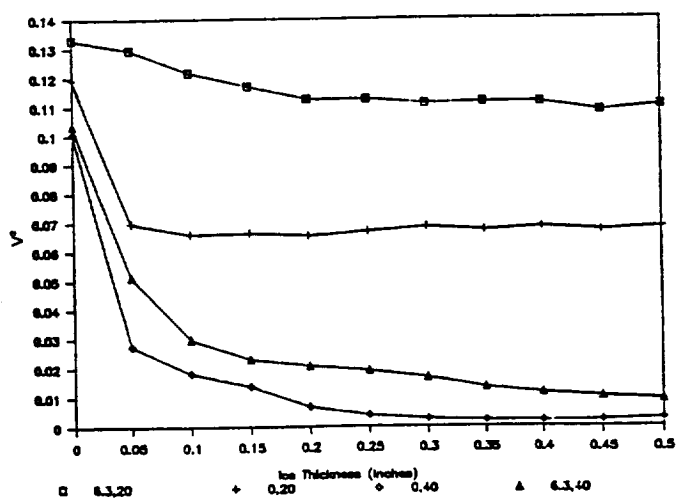
(a) First Local Damping



(b) Amplitude Ratio of 2 Biggest Peaks



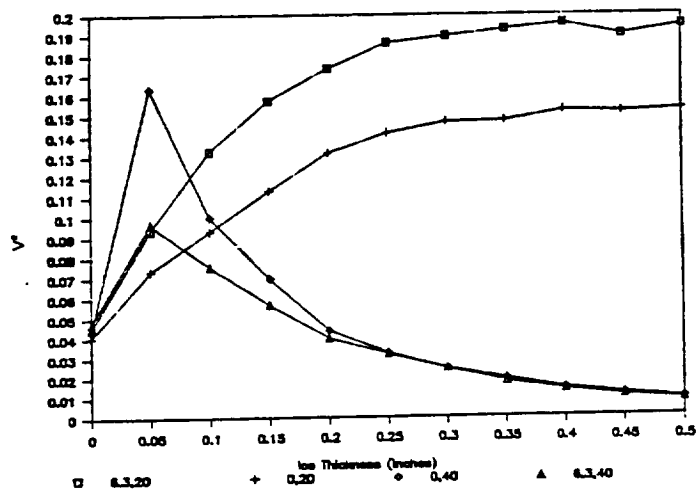
(c) Freq Difference of 2 Biggest Peaks



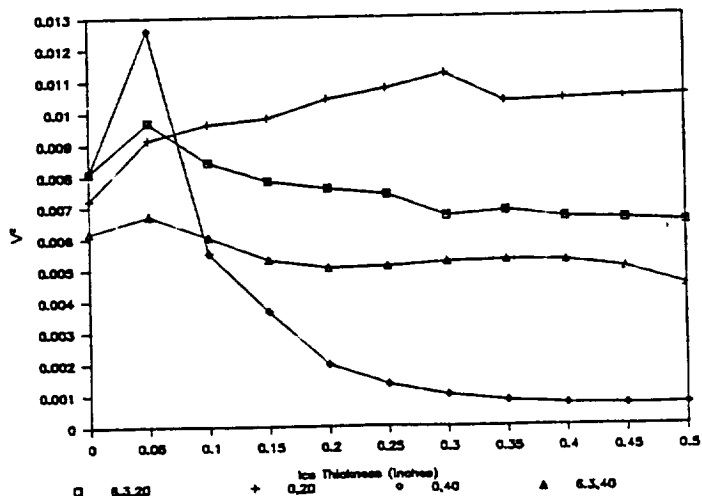
(d) Power in Freq Band 700-1150 KHz

Figure 2 - Sensor 1 Test Conditions: -9°C , 1 g/cm^3 LWC, variable AOA & DIA

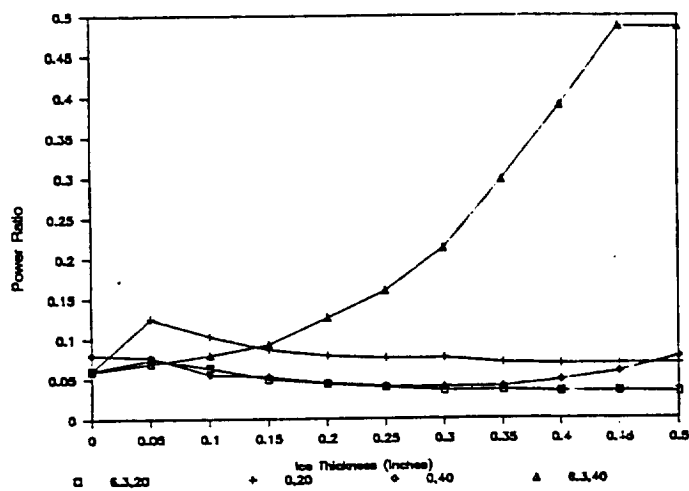
Figure 2 - Continued



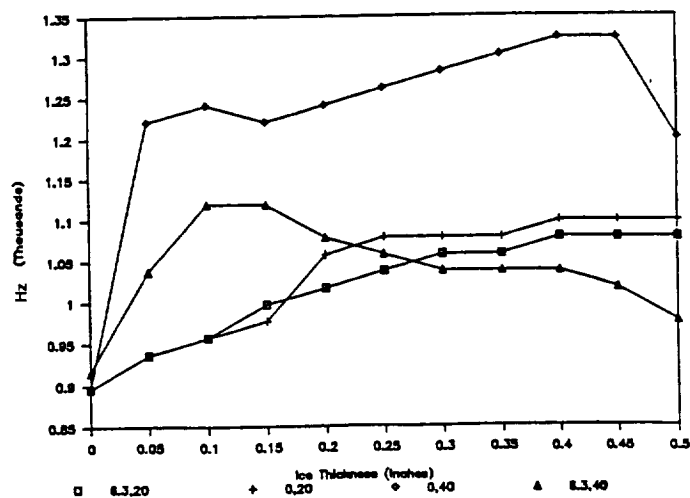
(e) Power in Freq Band 1150-1800 KHz



(f) Power in Freq 1800-3000 KHz

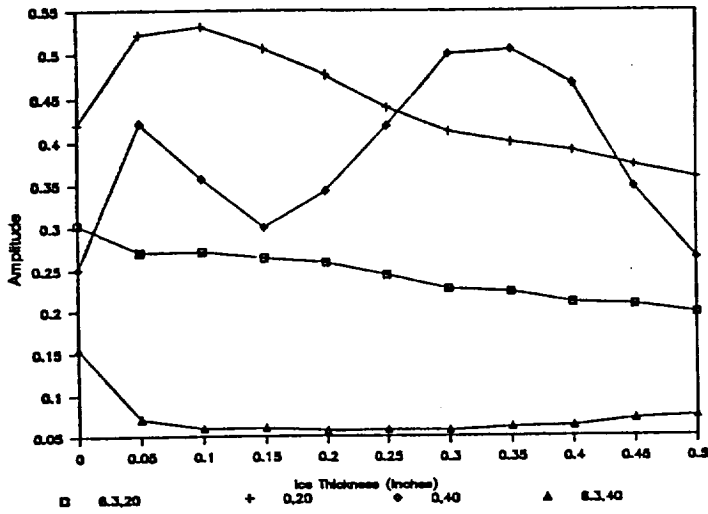


(g) Ratio of Smallest & Largest Power

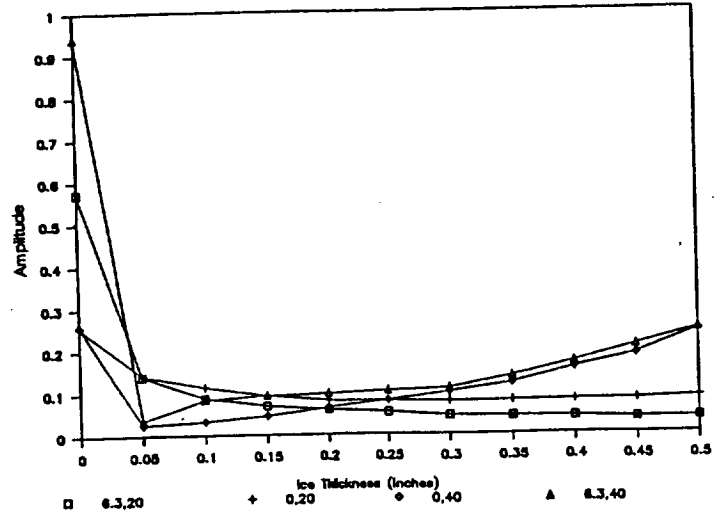


(h) Freq with 25% of Energy

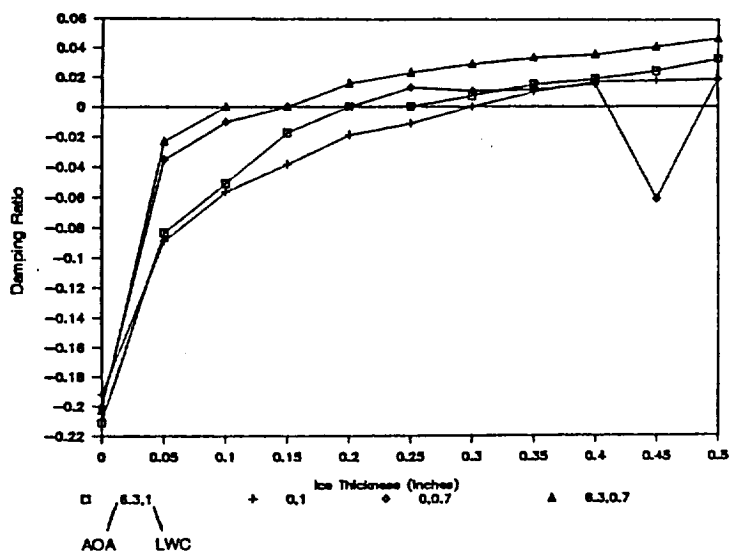
Figure 2 - Concluded



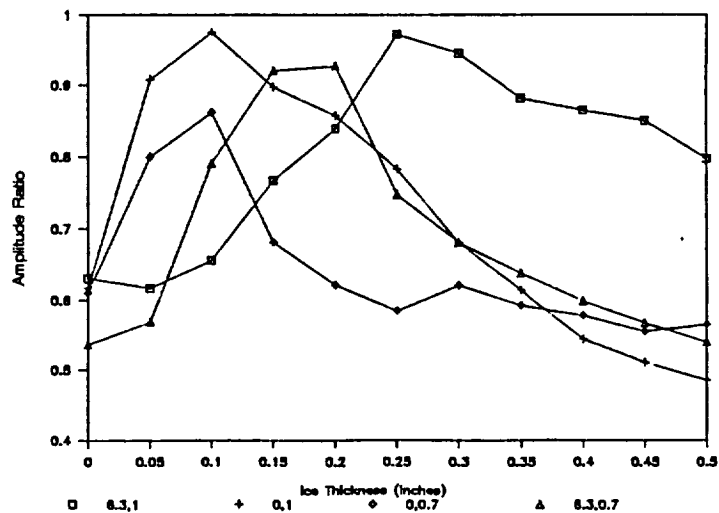
(i) Transfer Function 1



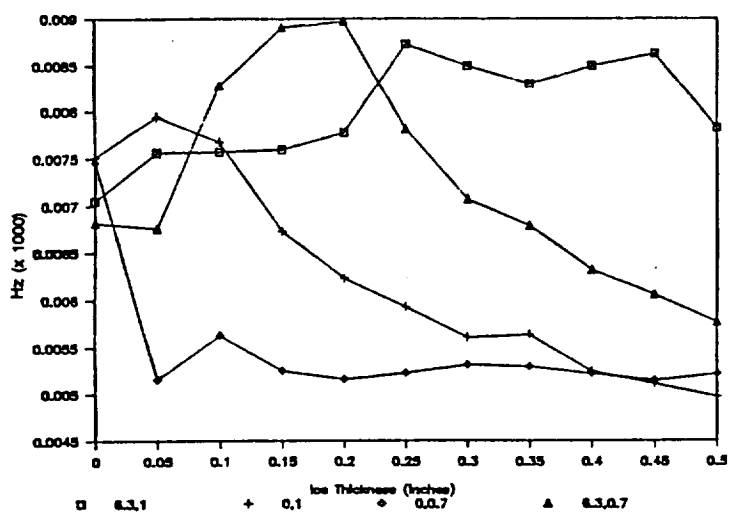
(j) Transfer Function 2



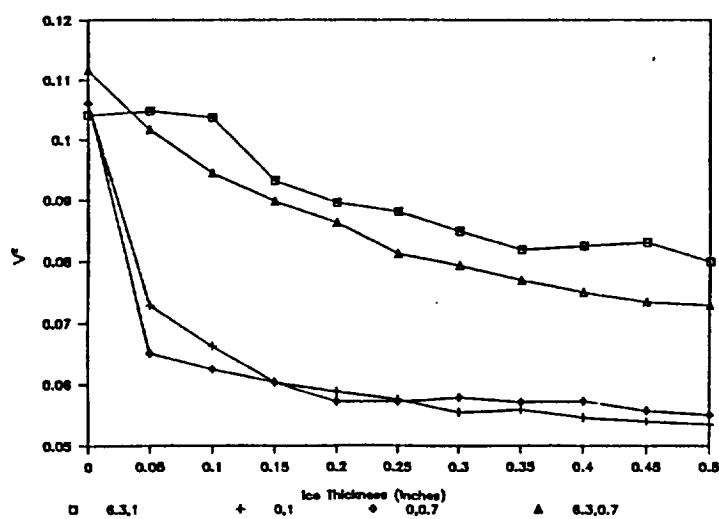
(a) First Local Damping



(b) Amp Ratio of 2 Biggest Peaks



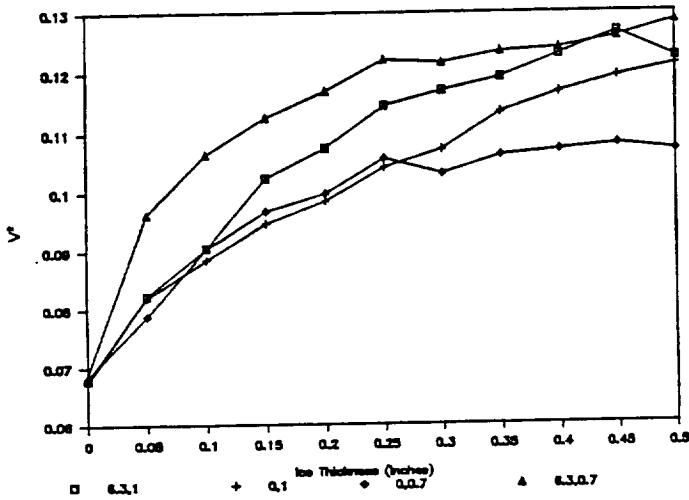
(c) Freq Difference of 2 Biggest Peaks



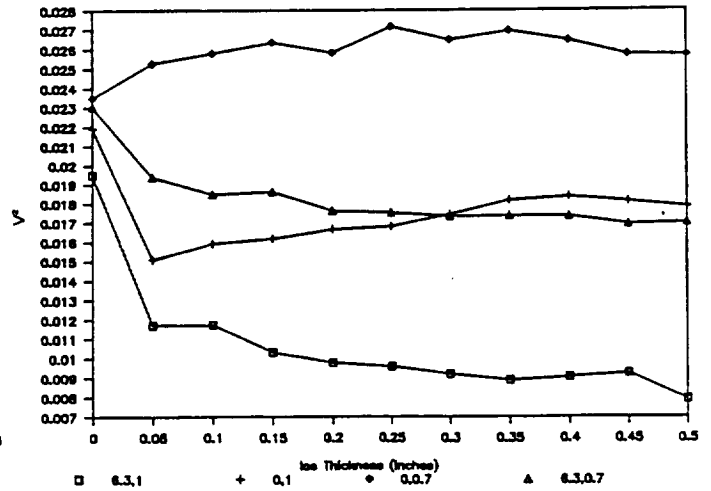
(d) Power in Freq Band 700-1150 KHz

Figure 3 - Sensor 1 Test Conditions: -23°C , $20\mu\text{m}$ DIA, variable AOA & LWC

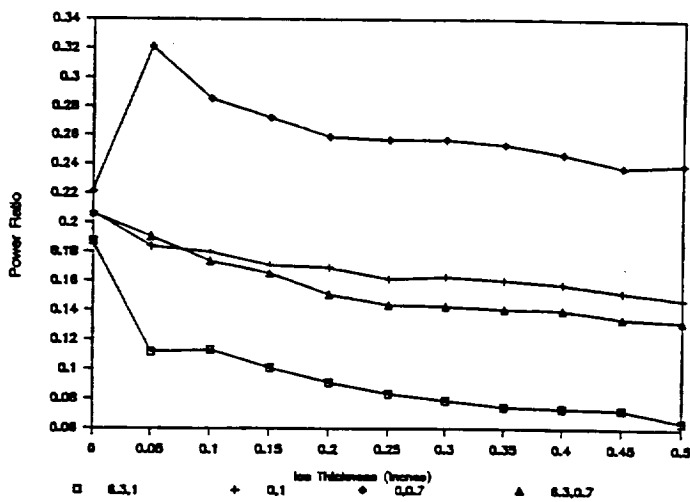
Figure 3 - Continued



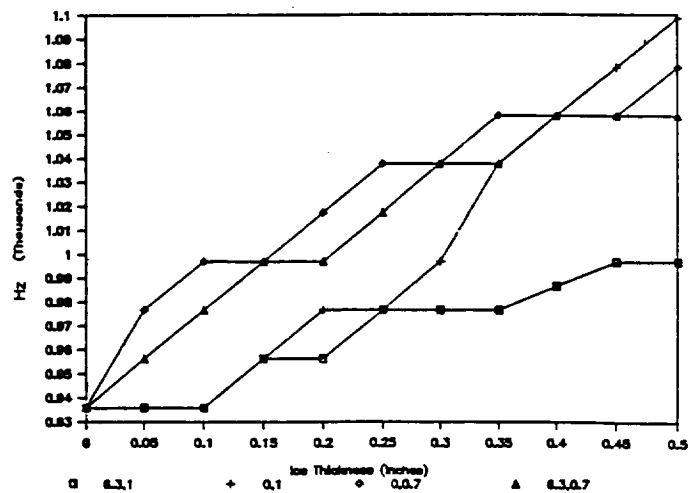
(e) Power in Freq Band 1150-1800 KHz



(f) Power in Freq Band 1800-3000 KHz

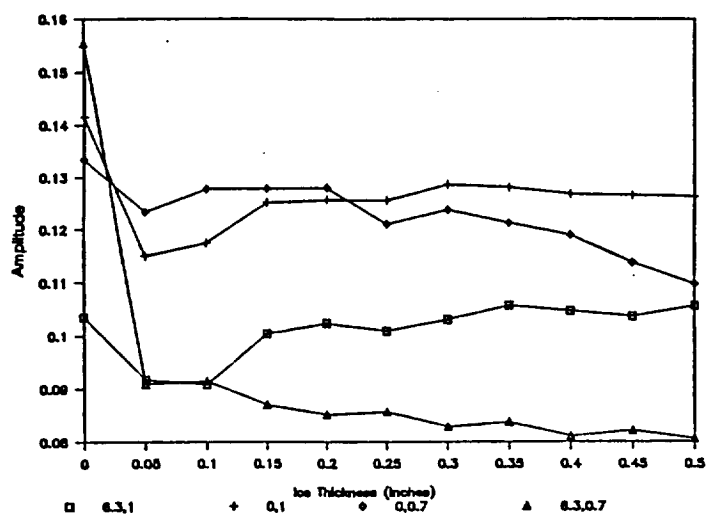


(g) Ratio of Smallest and Largest Power

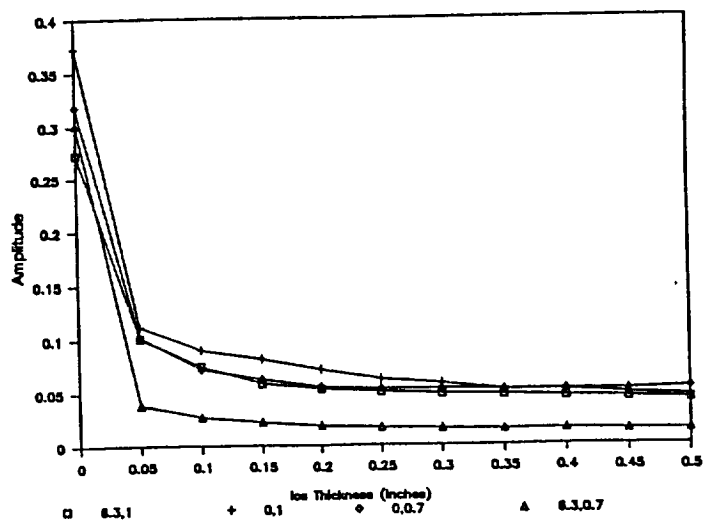


(h) Freq with 25% of Energy

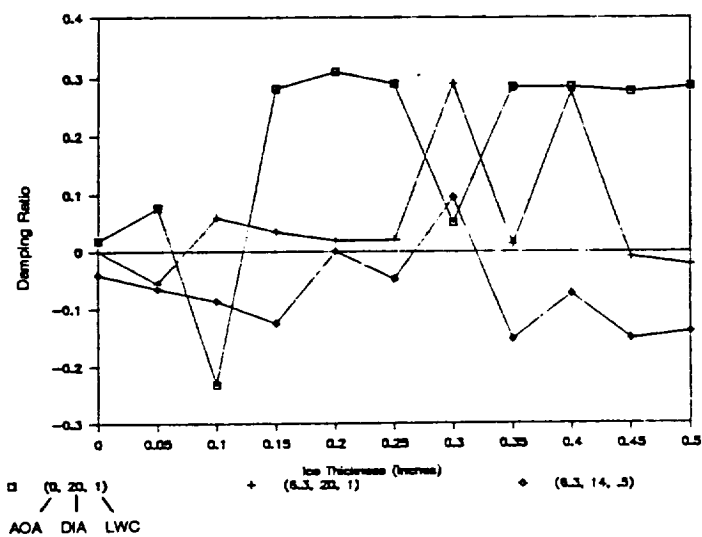
Figure 3 - Concluded



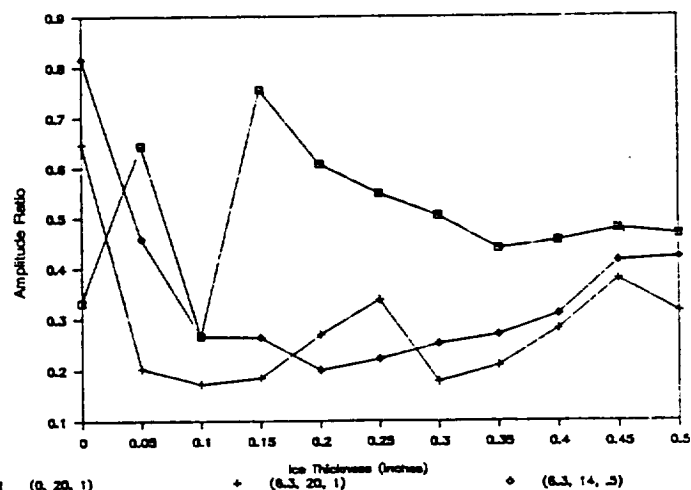
(i) Transfer Function 1



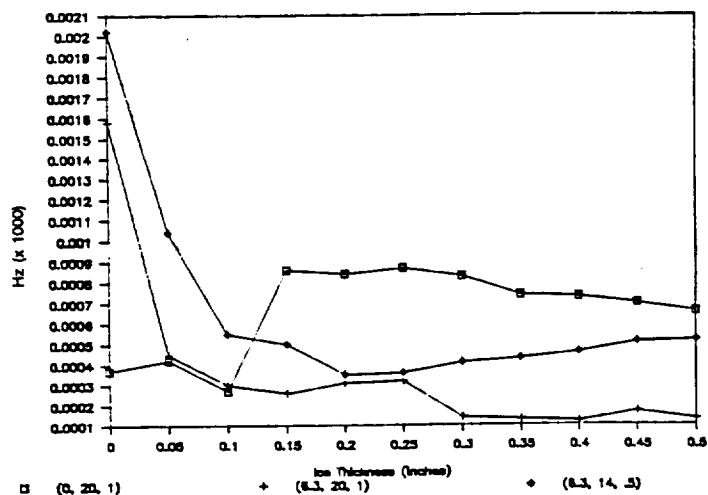
(j) Transfer Function 2



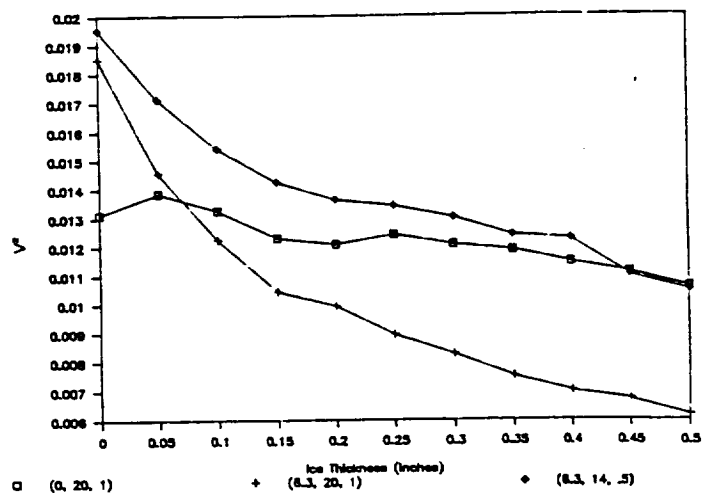
(a) First Local Damping



(b) Amp Ratio of 2 Biggest Peaks



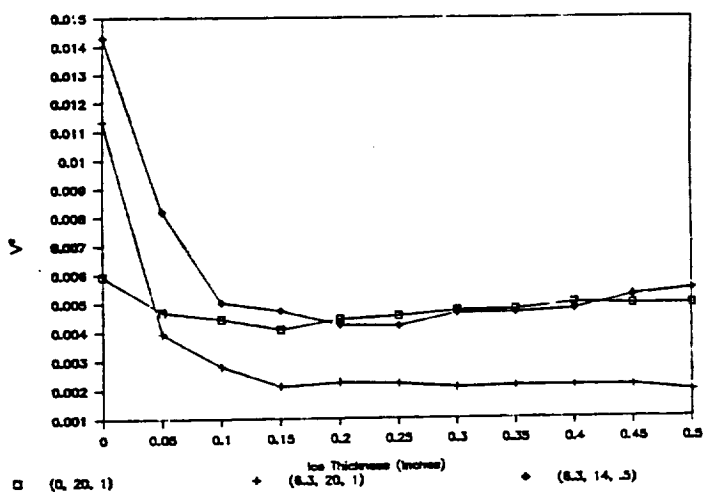
(c) Freq Difference of 2 biggest Peaks



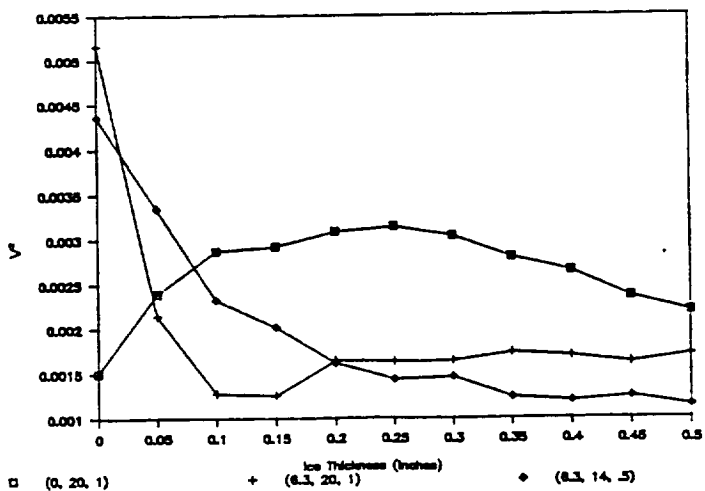
(d) Power in Freq Band 700-1150 KHz

Figure 4 - Sensor 2 Test Conditions: -1°C , variable AOA, DIA, & LWC

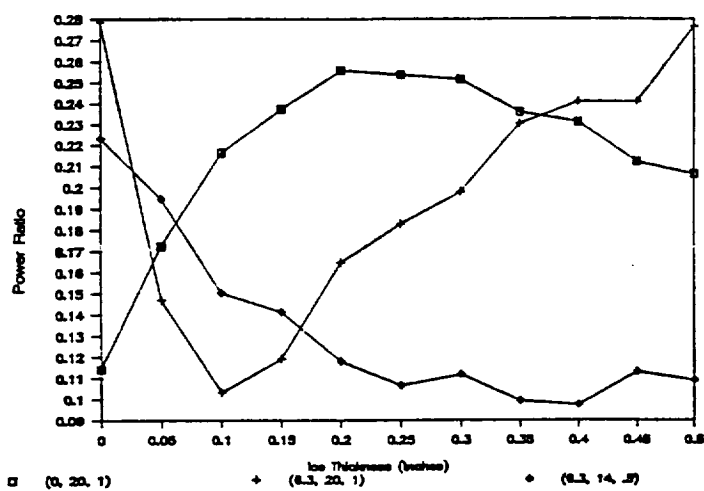
Figure 4 - Continued



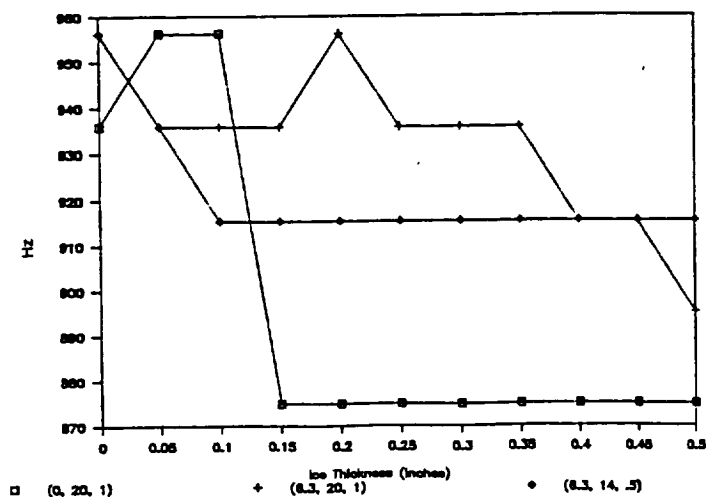
(e) Power in Freq Band 1150-1800 KHz



(f) Power in Freq Band 1800-3000 KHz

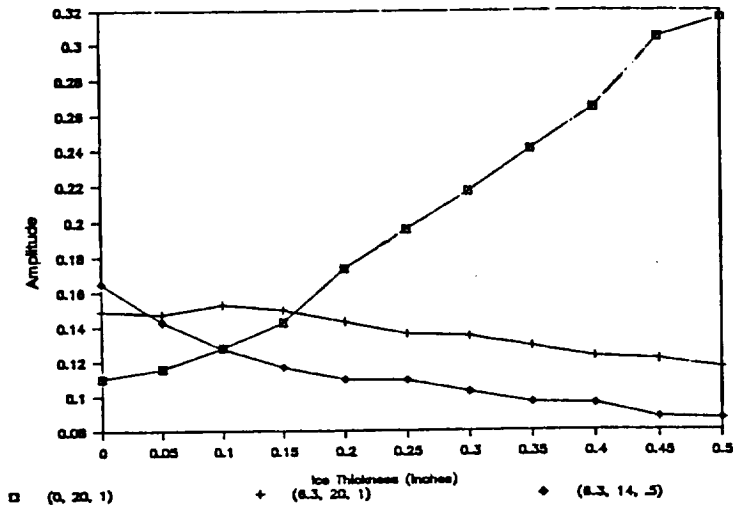


(g) Ratio of Smallest & Largest Power

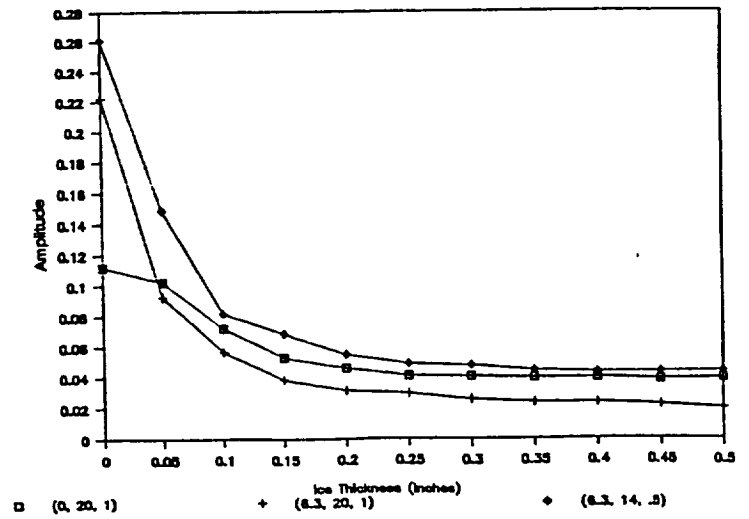


(h) Freq with 25% of Energy

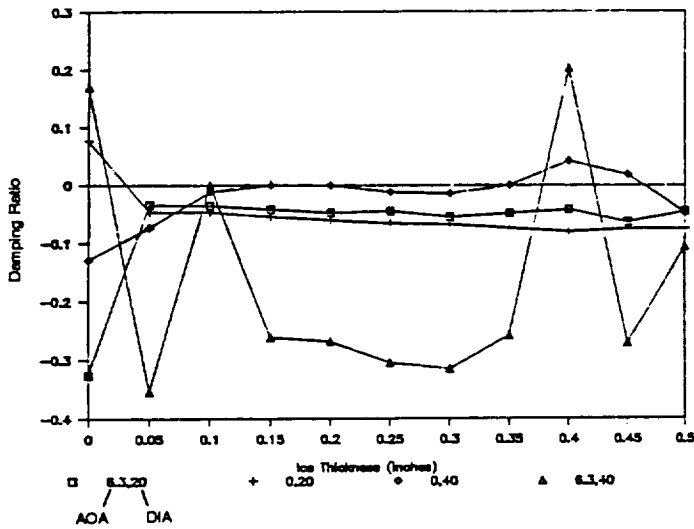
Figure 4 - Concluded



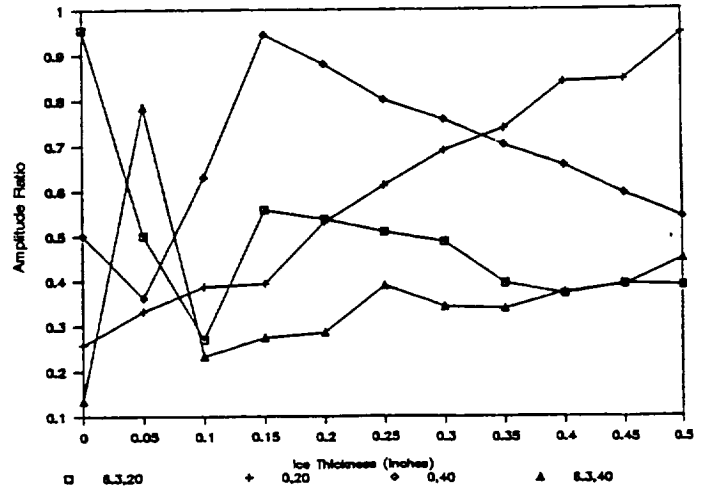
(i) Transfer Function 1



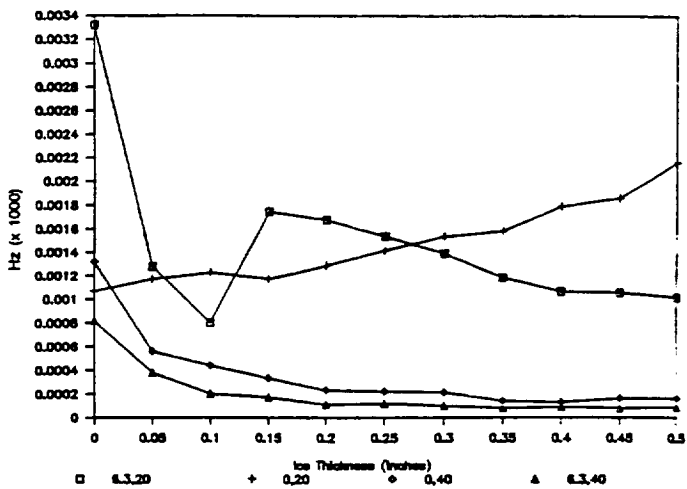
(j) Transfer Function 2



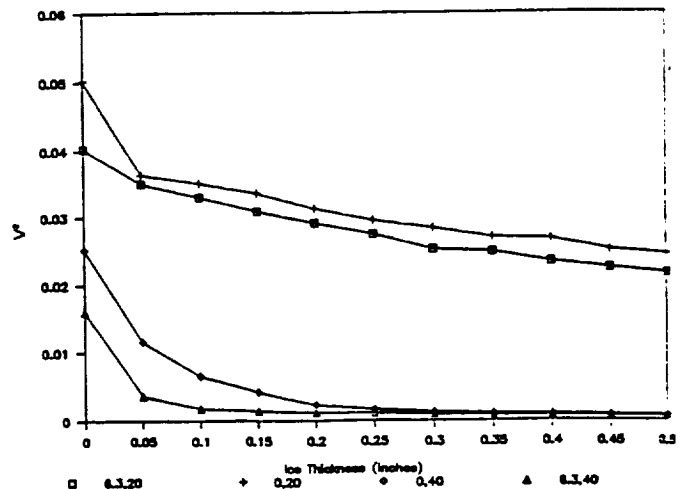
(a) First Local Damping



(b) Amp Ratio of 2 Biggest Peaks



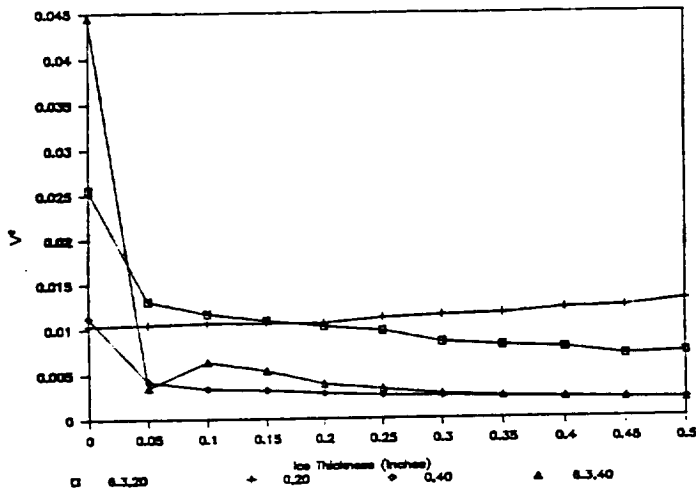
(c) Freq Difference of 2 Biggest Peaks



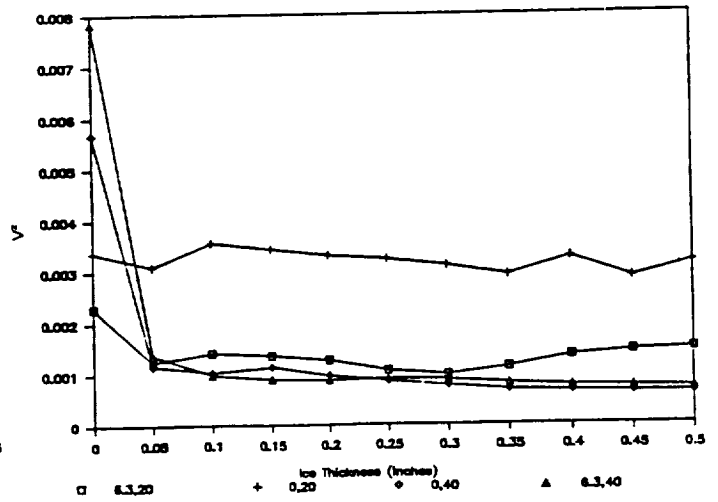
(d) Power in Freq Band 700-1150 KHz

Figure 5 - Sensor 2 Test Conditions: -9°C , 1 g/cm^3 LWC, variable AOA & DIA

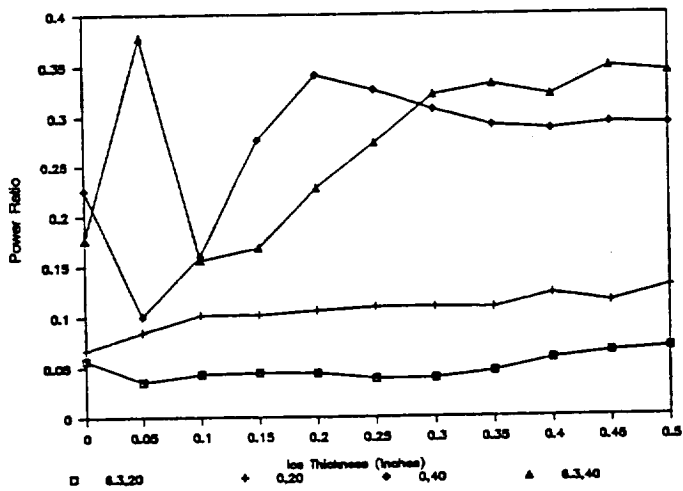
Figure 5 - Continued



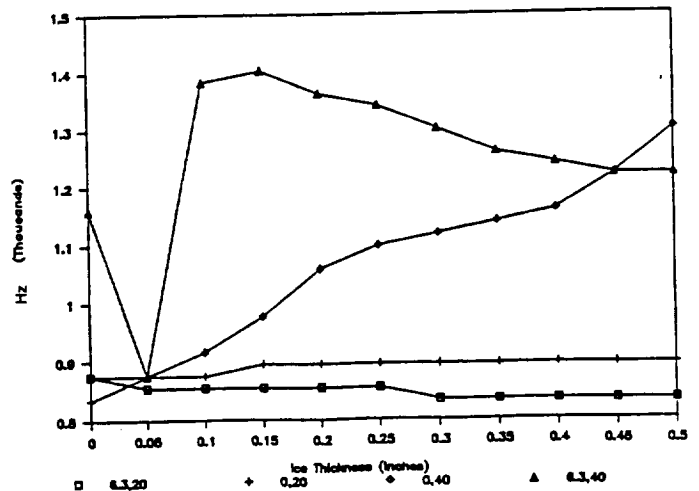
(e) Power in Freq Band 1150-1800 KHz



(f) Power in Freq Band 1800-3000 KHz

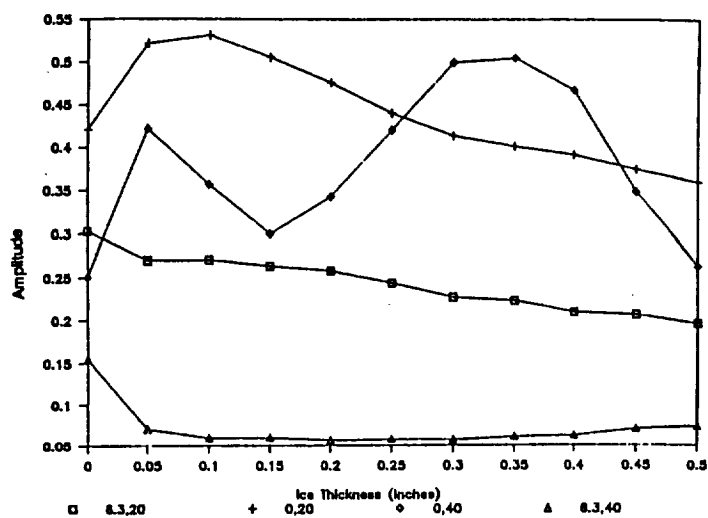


(g) Ratio of Smallest & Largest Power

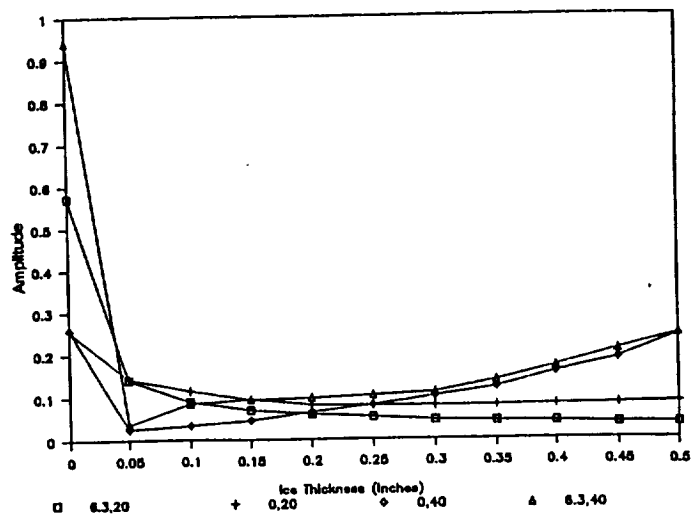


(h) Freq with 25% of Energy

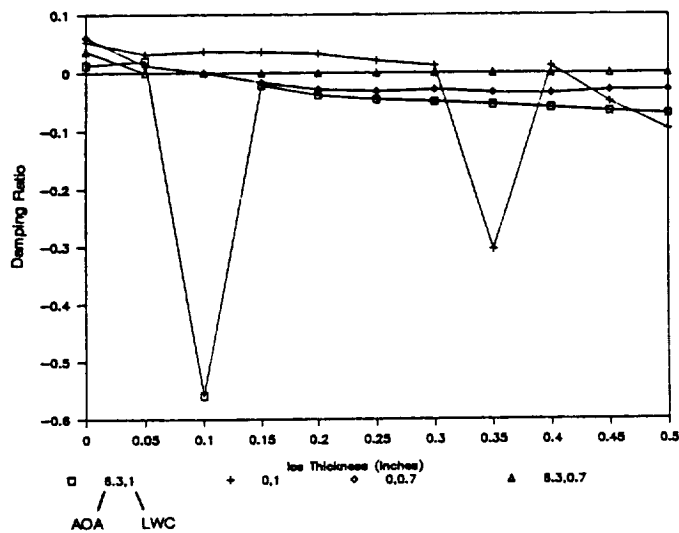
Figure 5 - Concluded



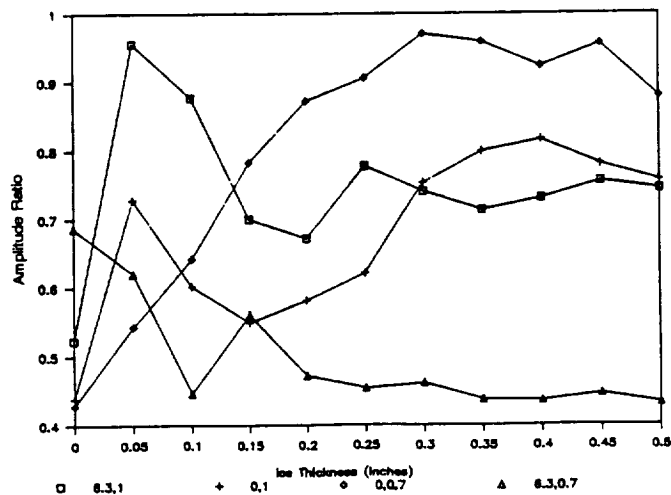
(i) Transfer Function 1



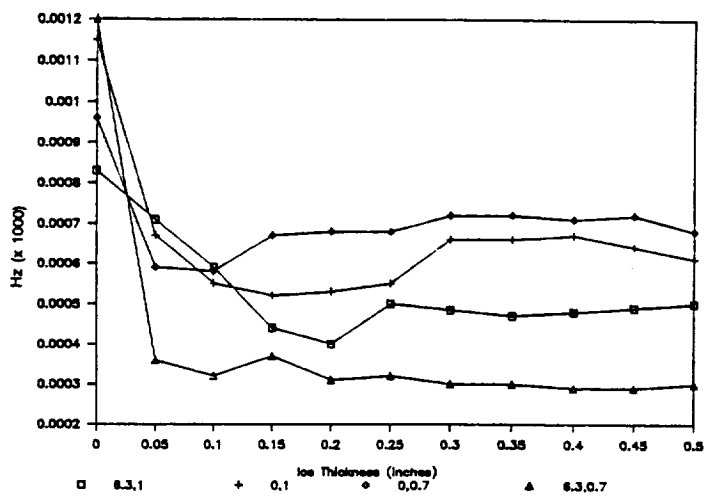
(j) Transfer Function 2



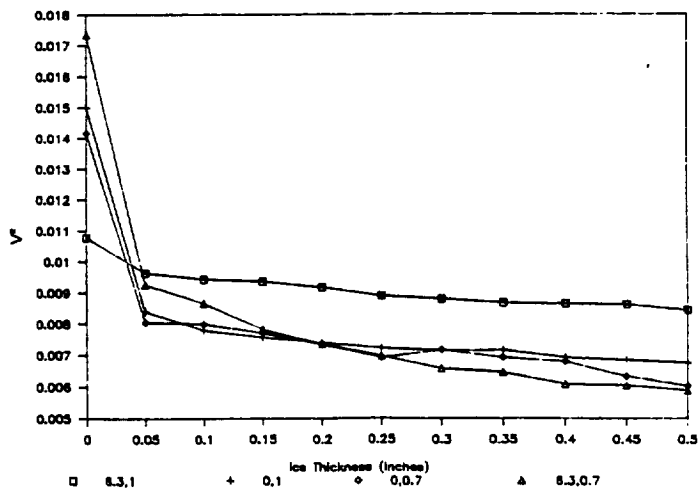
(a) First Local Damping



(b) Amp Ratio of 2 Biggest Peaks



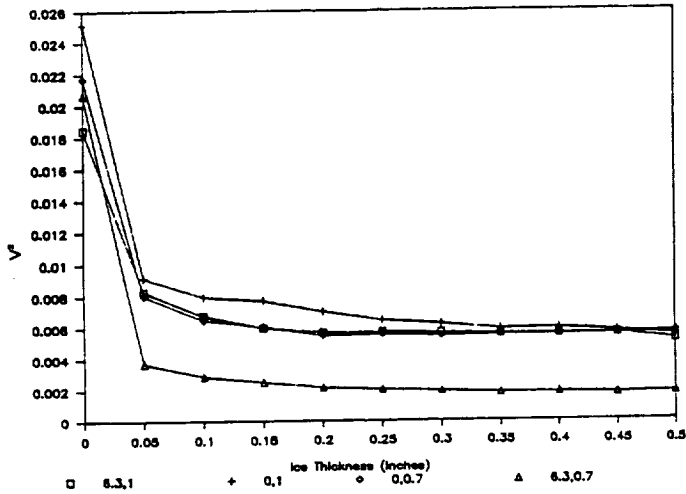
(c) Freq Difference of 2 Biggest Peaks



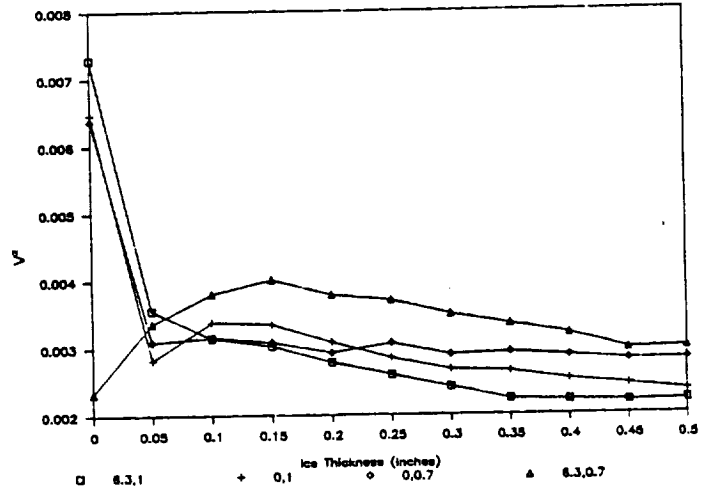
(d) Power in Freq Band 700-1150 KHz

Figure 6 - Sensor 2 Test Conditions: -23°C , $20\mu\text{m}$ DIA, variable AOA & LWC

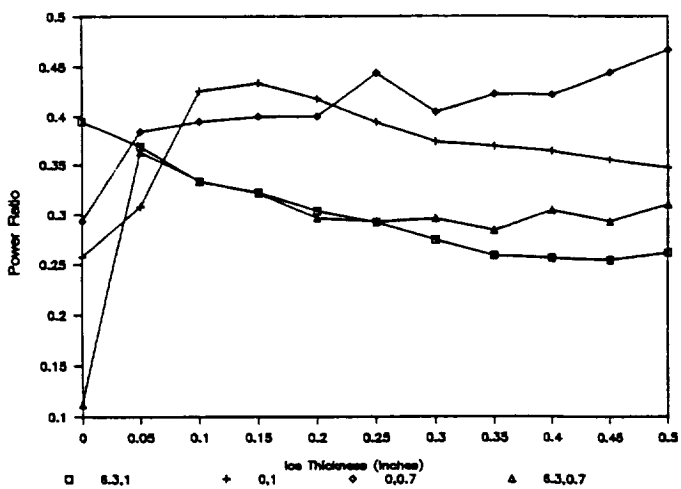
Figure 6 - Continued



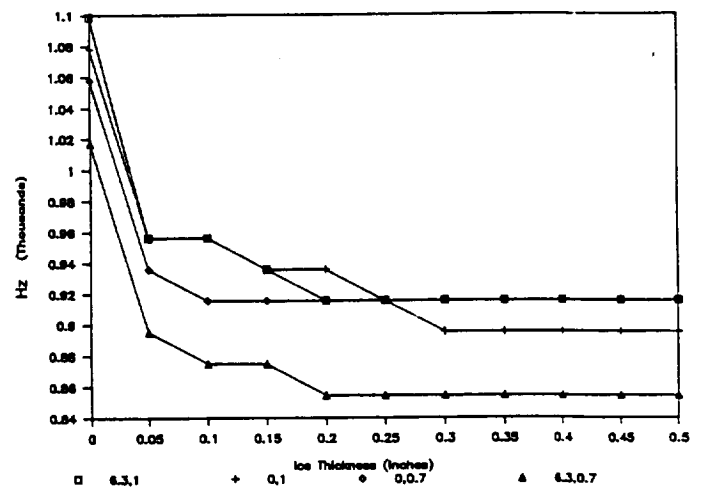
(e) Power in Freq Band 1150-1800 KHz



(f) Power in Freq Band 1800-3000 KHz

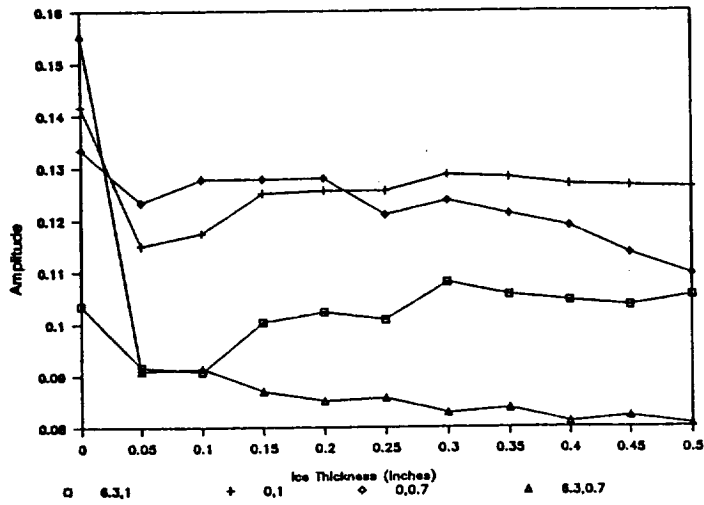


(g) Ratio of Smallest & Largest Power

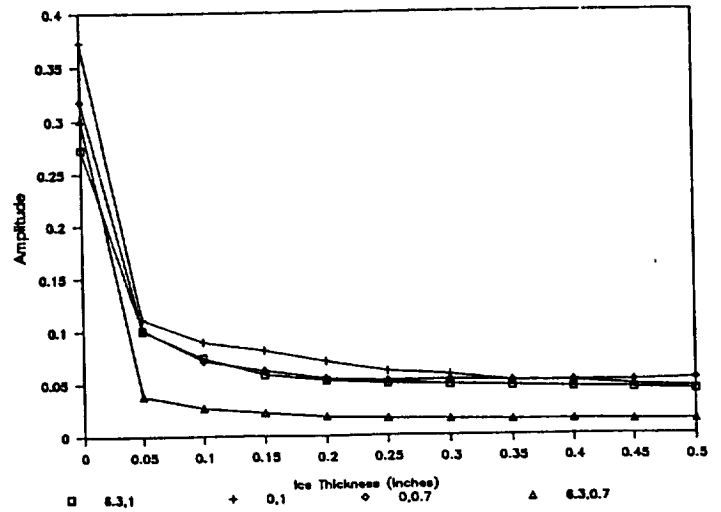


(h) Freq with 25% of Energy

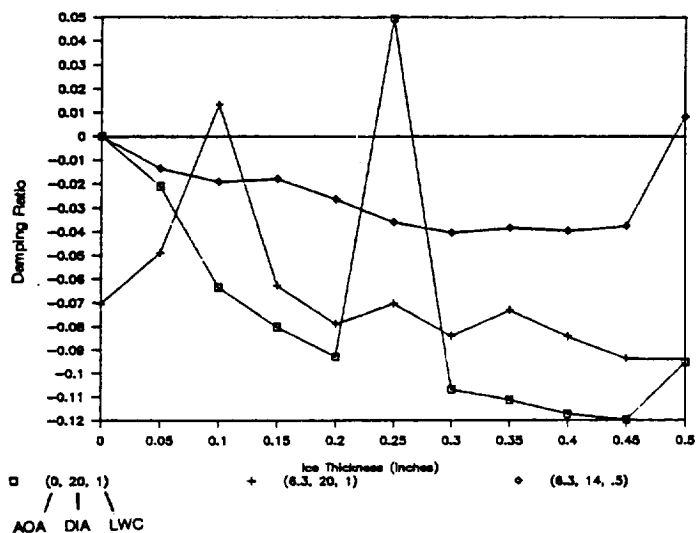
Figure 6 - Concluded



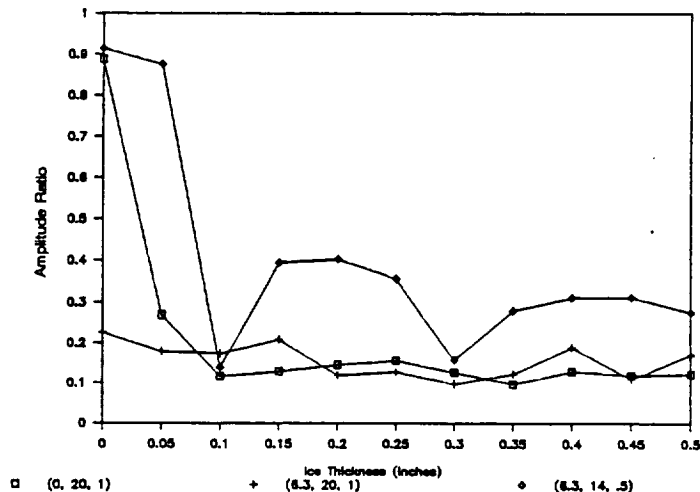
(i) Transfer Function 1



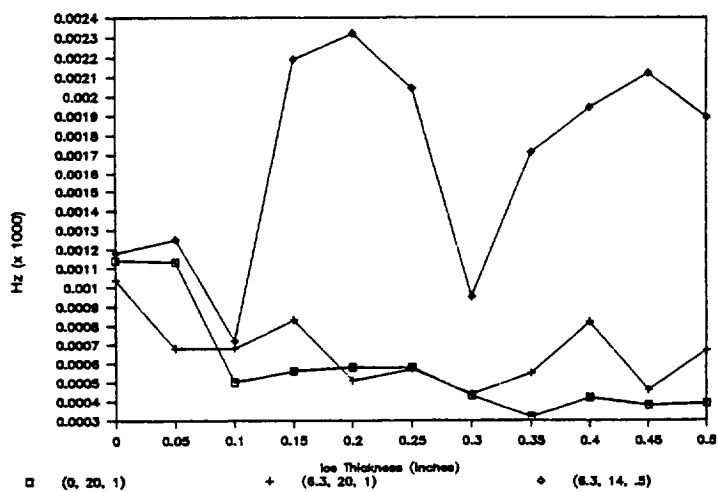
(j) Transfer Function 2



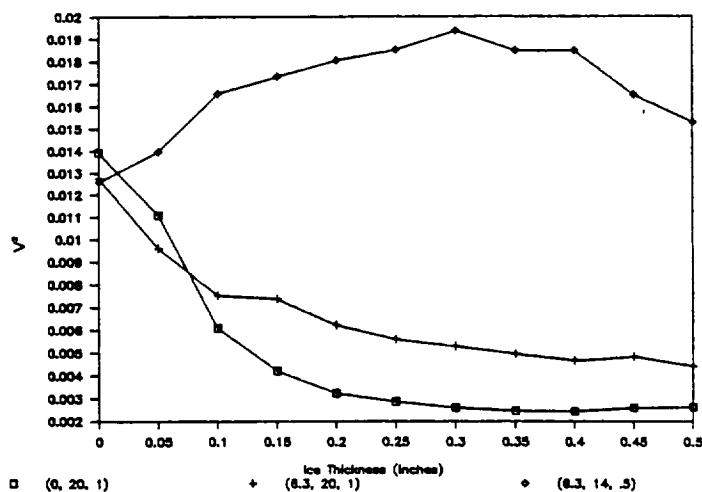
(a) First Local Damping



(b) Amp Ratio of 2 Biggest Peaks



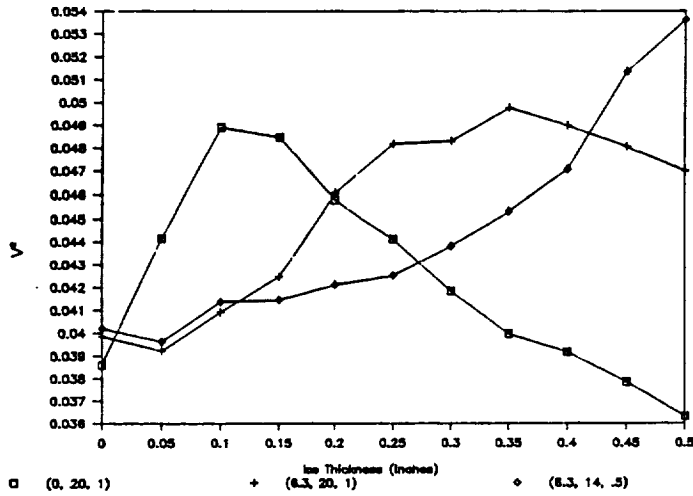
(c) Freq Difference of 2 Biggest Peaks



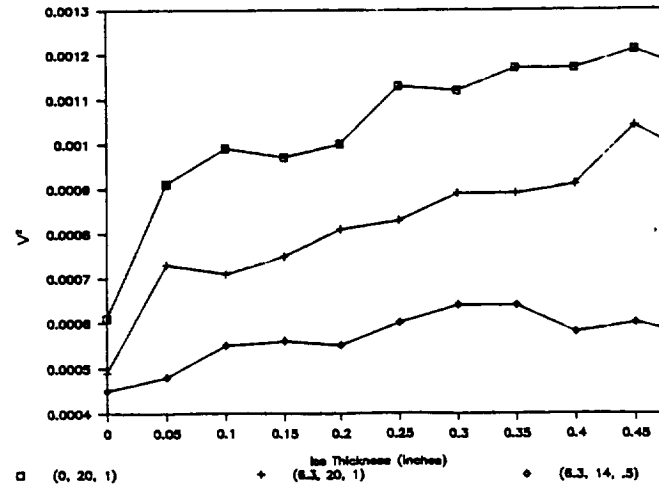
(d) Power in Freq Band 700-1150 KHz

Figure 7 - Sensor 3 Test Conditions: -1°C , variable AOA, DIA, & LWC

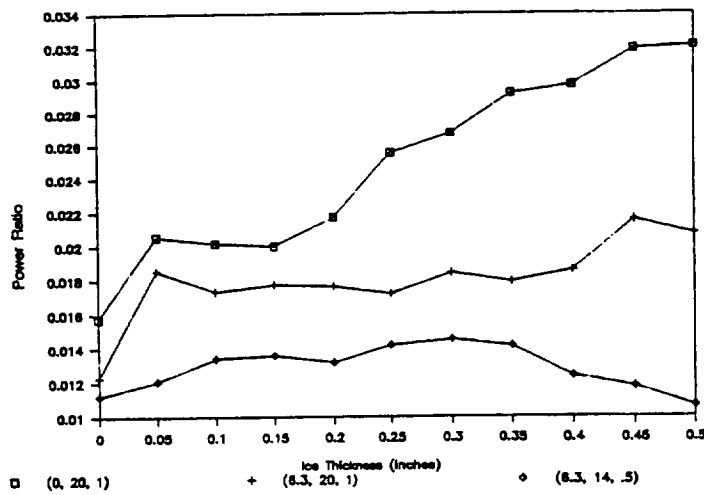
Figure 7 - Continued



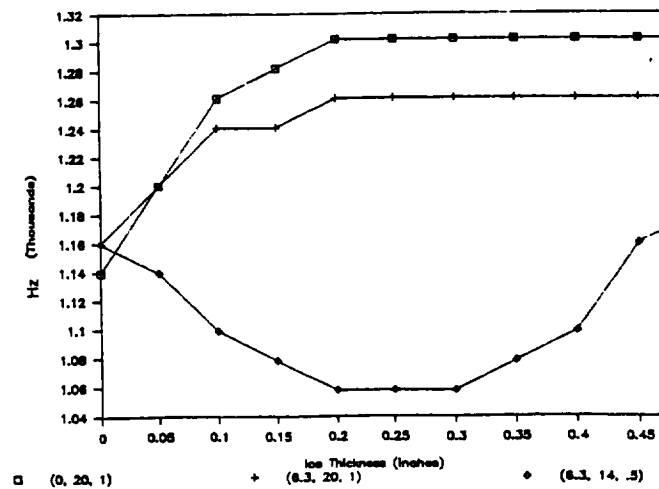
(e) Power in Freq Band 1150-1800 KHz



(f) Power in Freq Band 1800-3000 KHz

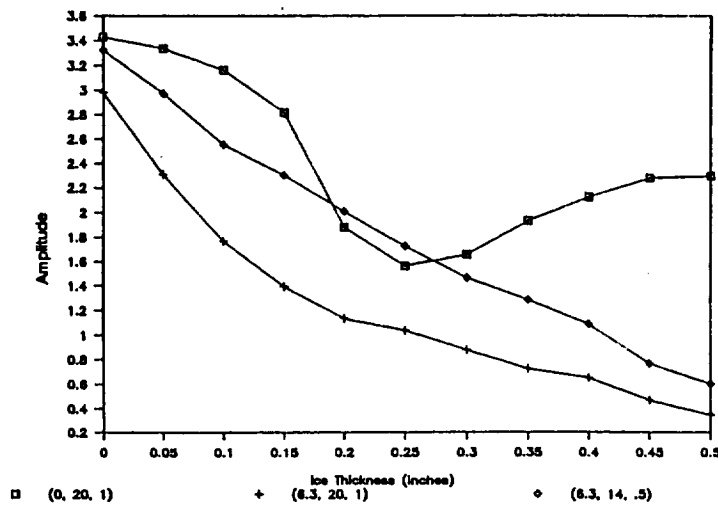


(g) Ratio of Smallest & Largest Power

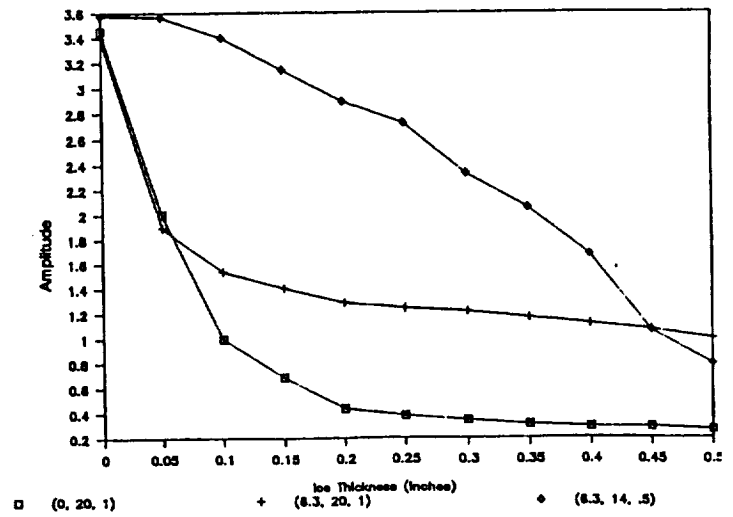


(h) Freq with 25% of Energy

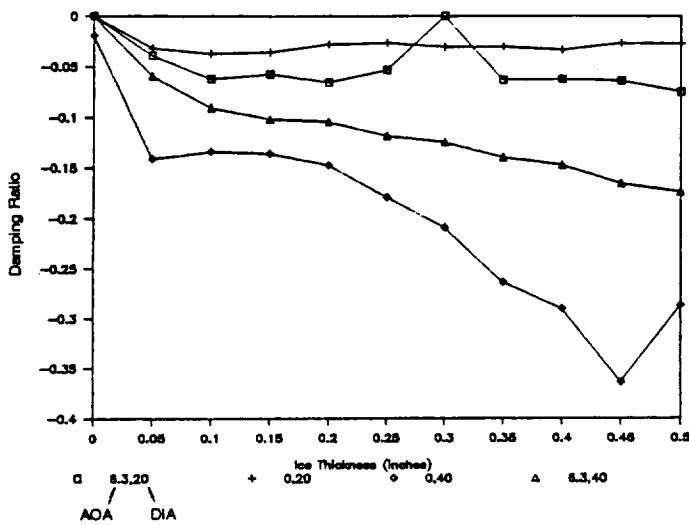
Figure 7 - Concluded



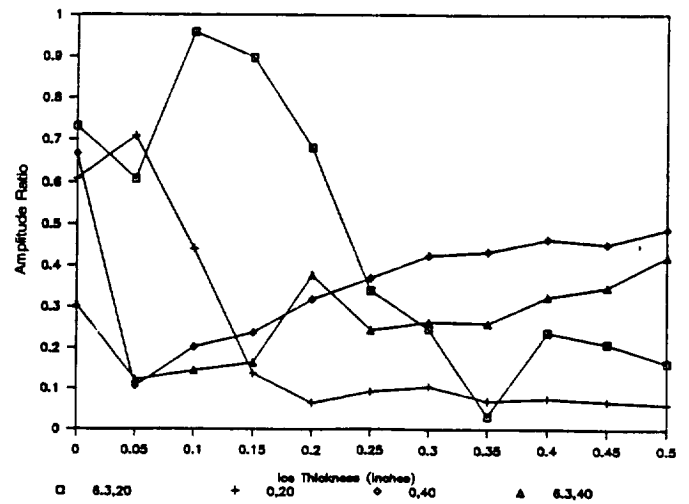
(i) Transfer Function 1



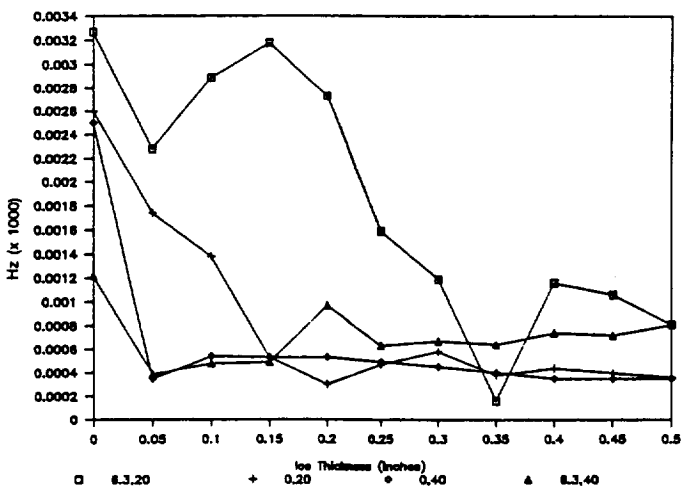
(j) Transfer Function 2



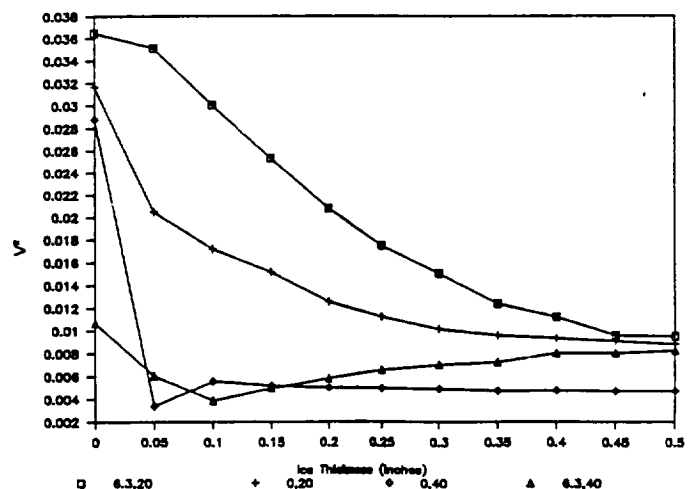
(a) First Local Damping



(b) Amp Ratio of 2 Biggest Peaks



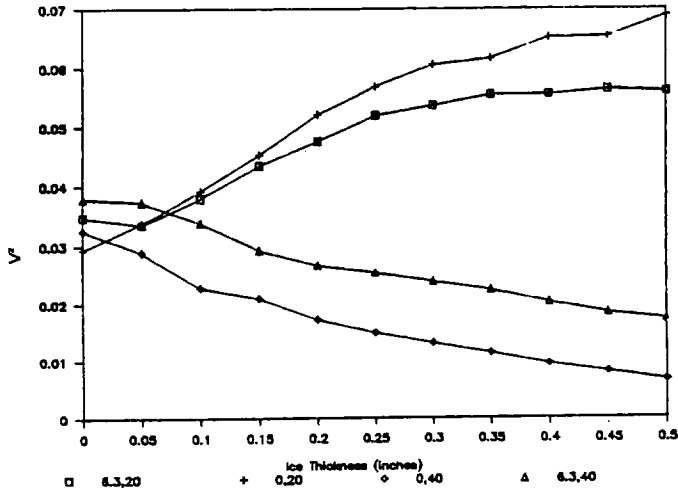
(c) Freq Difference of 2 Biggest Peaks



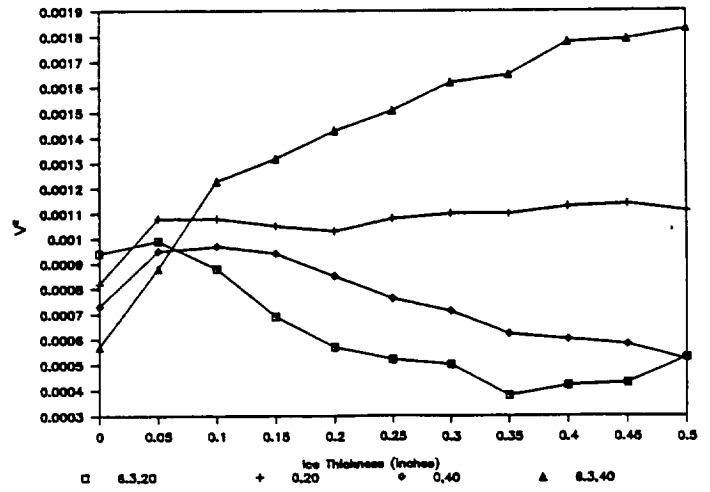
(d) Power in Freq Band 700-1150 KHz

Figure 8 - Sensor 3 Test Conditions: -9°C , 1 g/cm^3 LWC, variable AOA & DIA

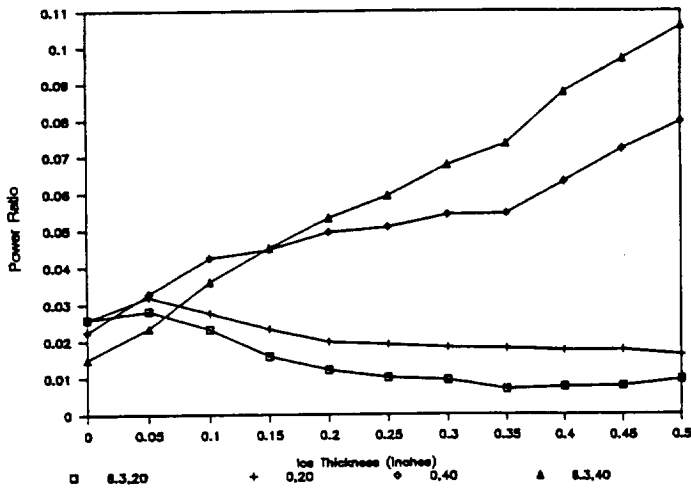
Figure 8 - Continued



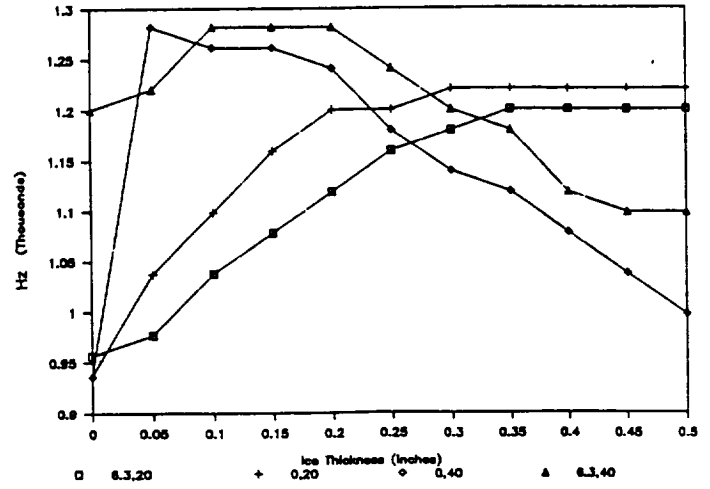
(e) Power in Freq Band 1150-1800 KHz



(f) Power in Freq Band 1800-3000 KHz

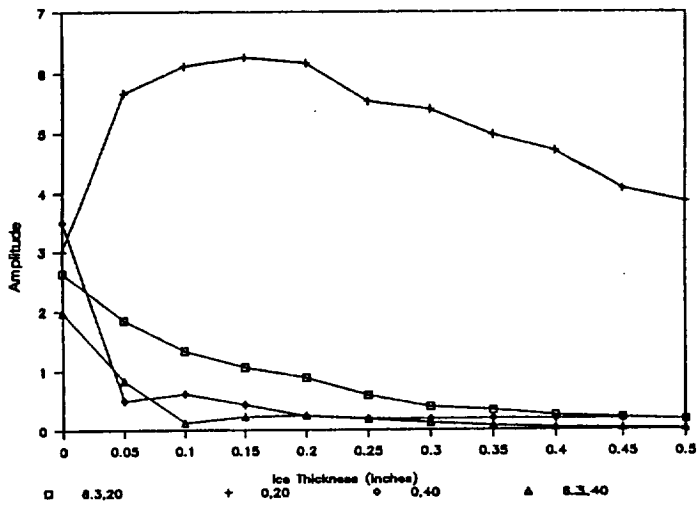


(g) Ratio of Smallest & Largest Power

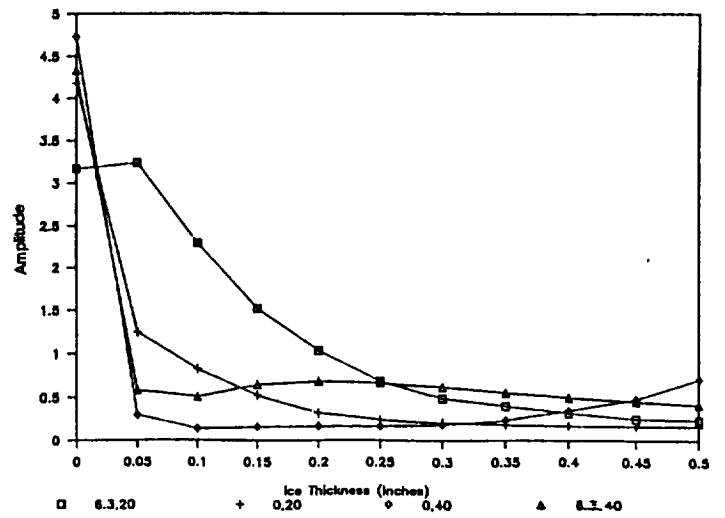


(h) Freq with 25% of Energy

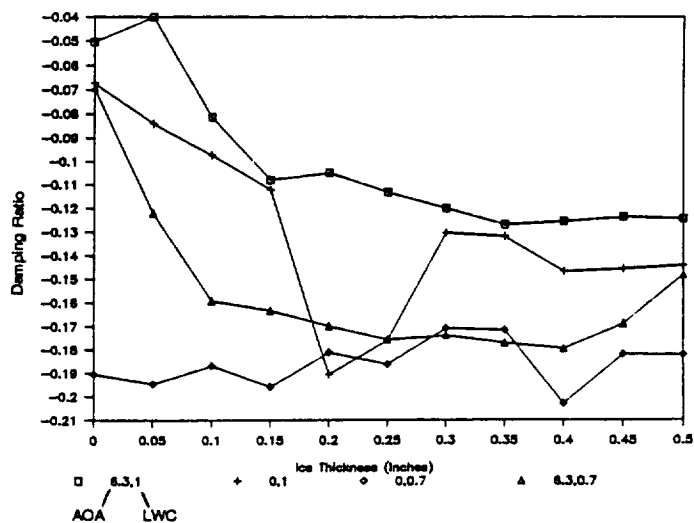
Figure 8 - Concluded



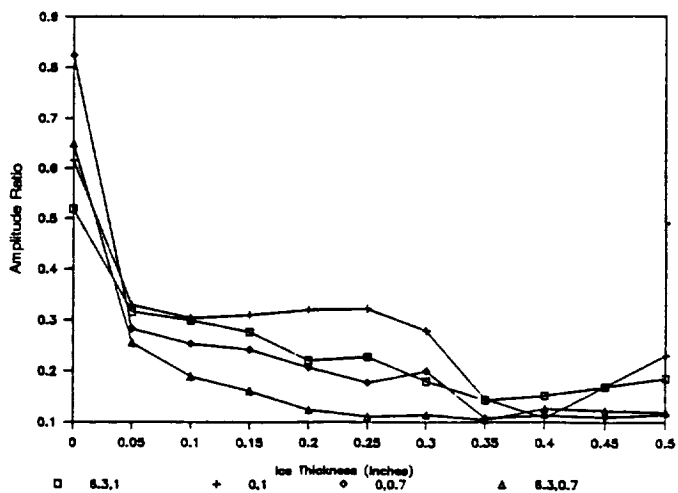
(i) Transfer Function 1



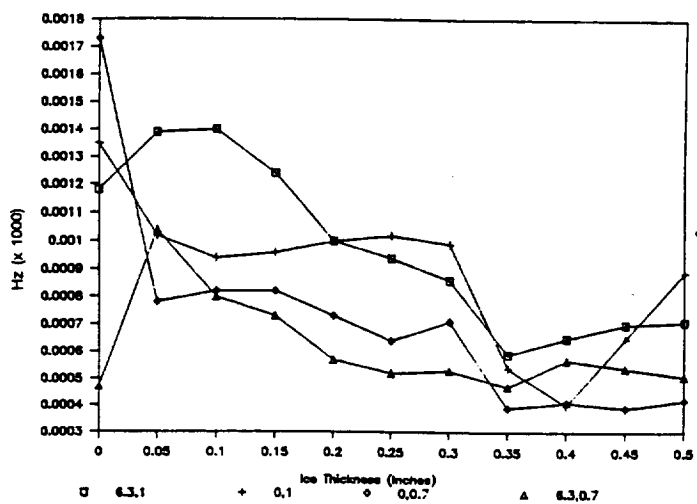
(j) Transfer Function 2



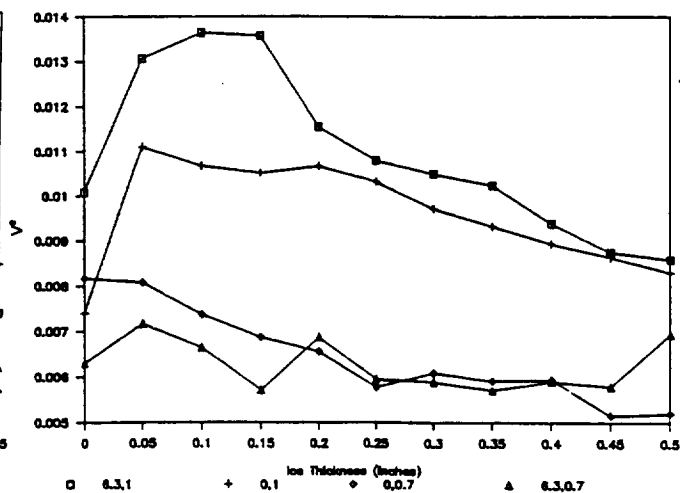
(a) First Local Damping



(b) Amp Ratio of 2 Biggest Peaks



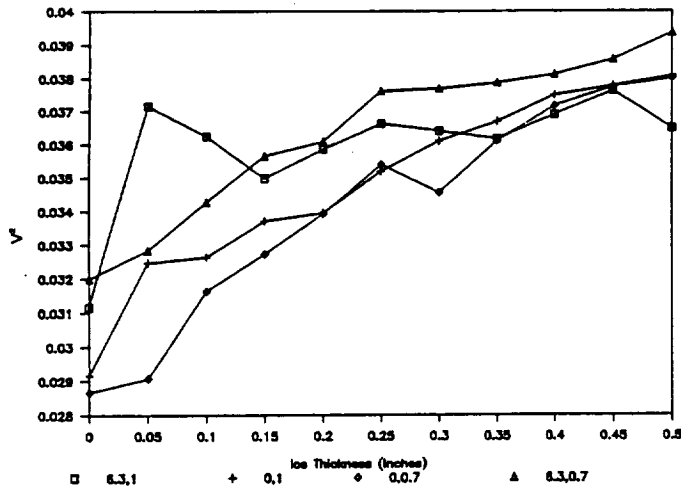
(c) Freq Difference of 2 Biggest Peaks



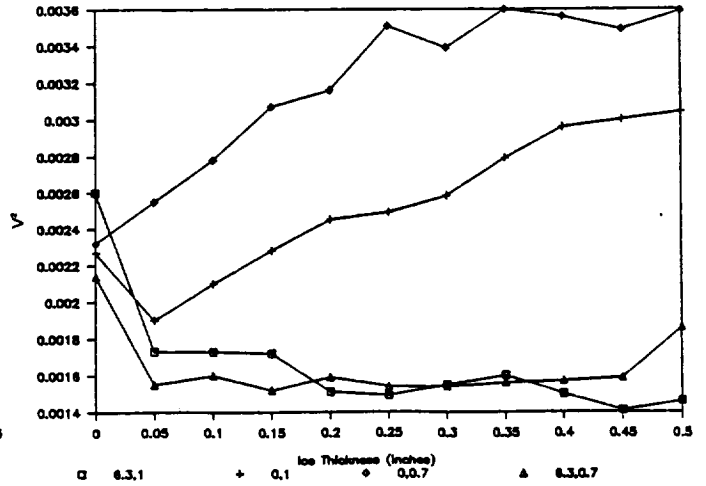
(d) Power in Freq Band 700-1150 KHz

Figure 9 - Sensor 3 Test Conditions: -23°C, 20µm DIA, variable AOA & LWC

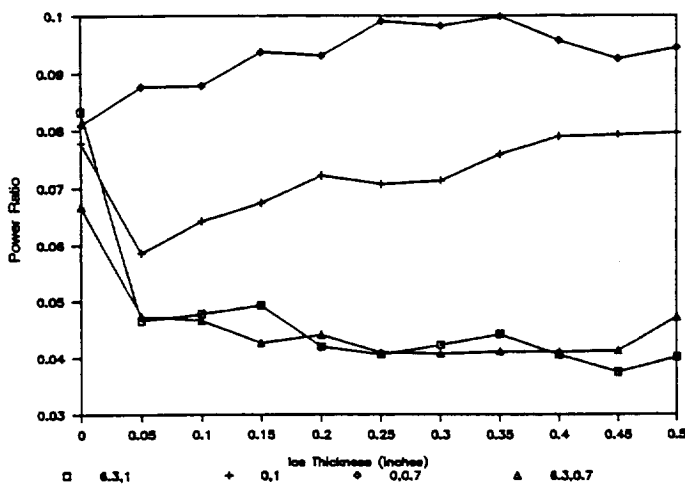
Figure 9 - Continued



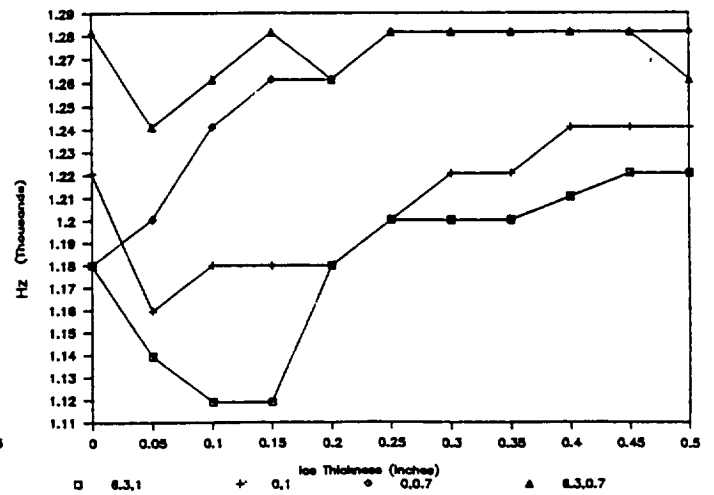
(e) Power in Freq Band 1150-1800 KHz



(f) Power in Freq Band 1800-3000 KHz

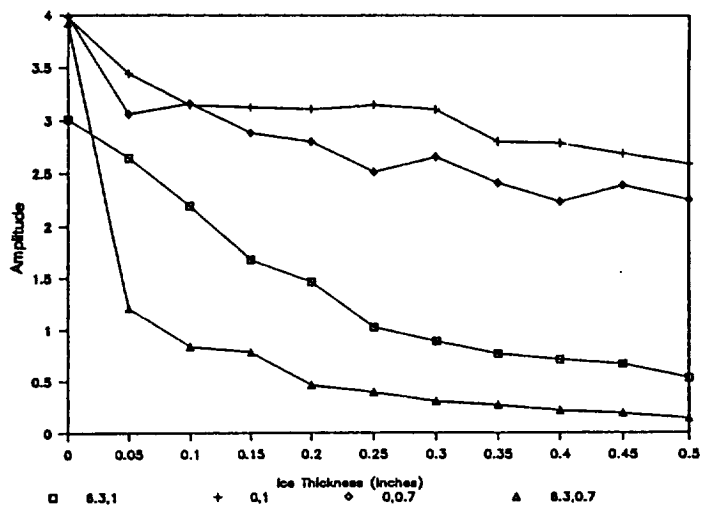


(g) Ratio of Smallest & Largest Power

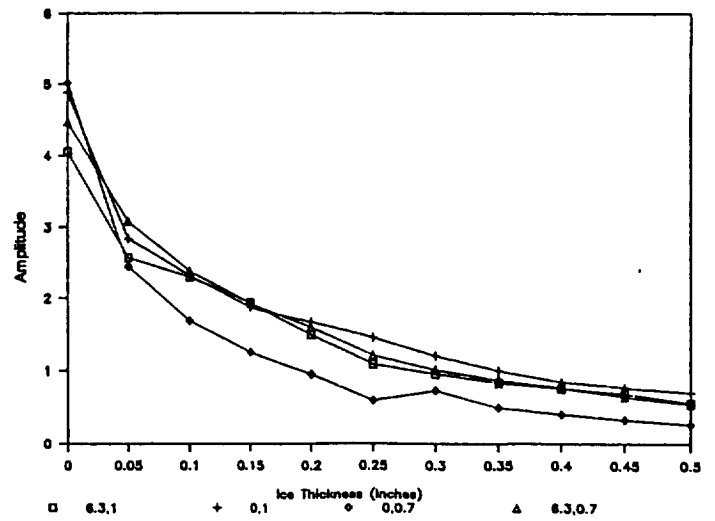


(h) Freq with 25% of Energy

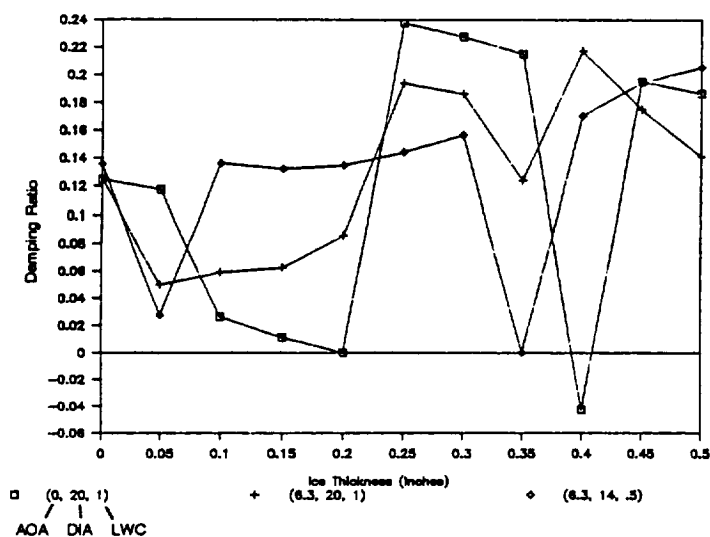
Figure 9 - Concluded



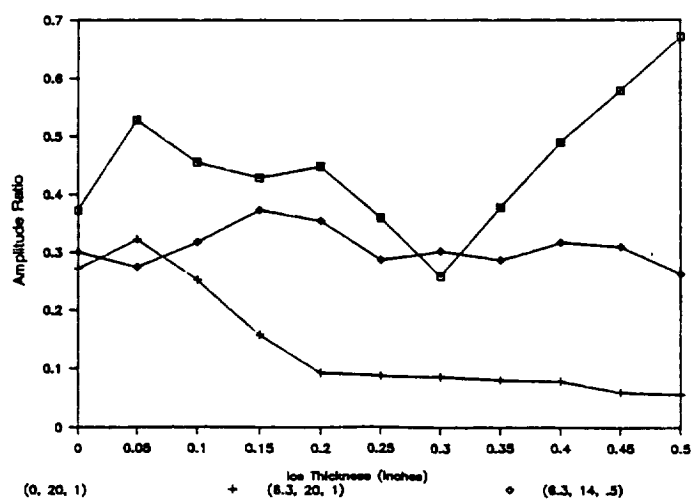
(i) Transfer Function 1



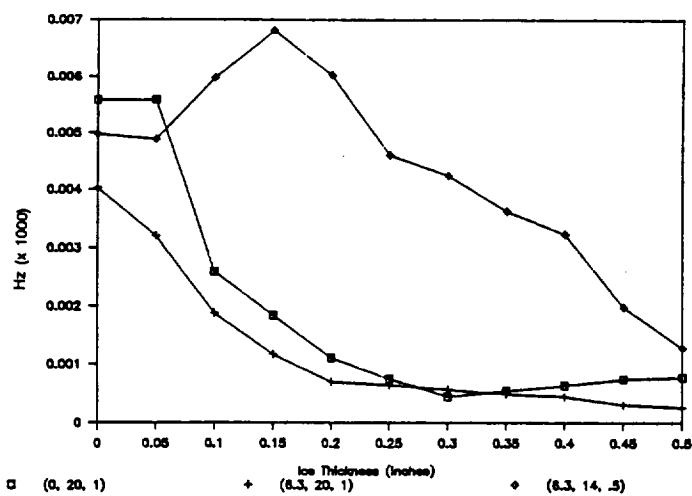
(j) Transfer Function 2



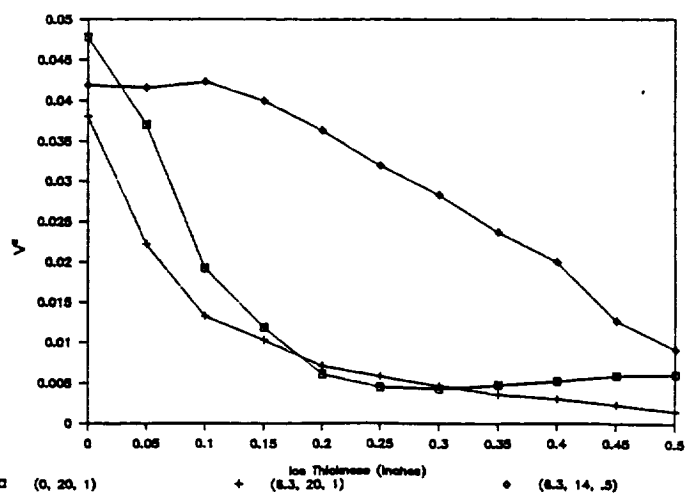
(a) First Local Damping



(b) Amp Ratio of 2 Biggest Peaks



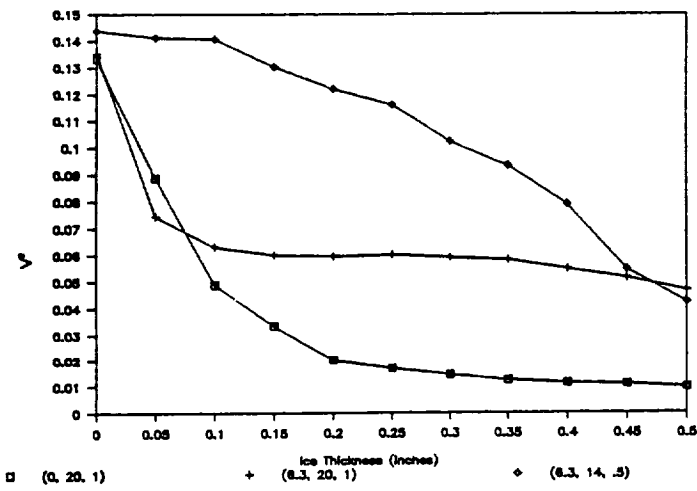
(c) Freq Difference of 2 Biggest Peaks



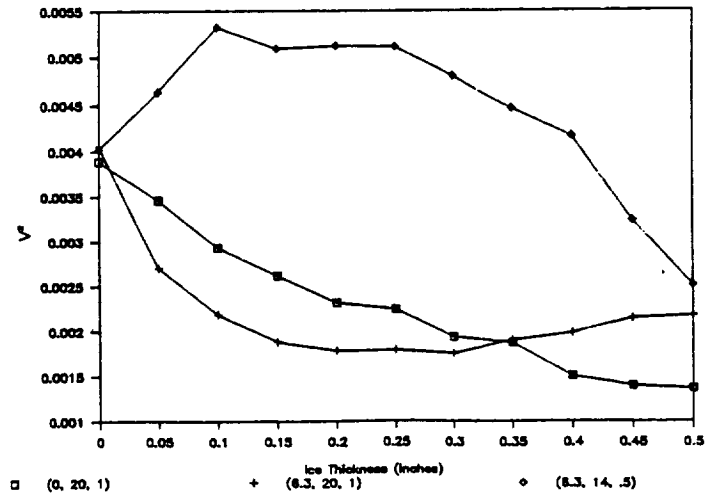
(d) Power in Freq Band 700-1150 KHz

Figure 10 - Sensor 4 Test Conditions: -1°C, variable AOA, DIA, & LWC

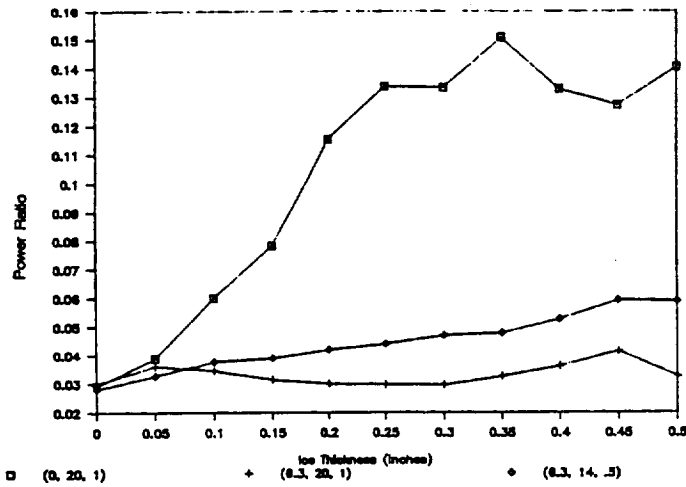
Figure 10 - Continued



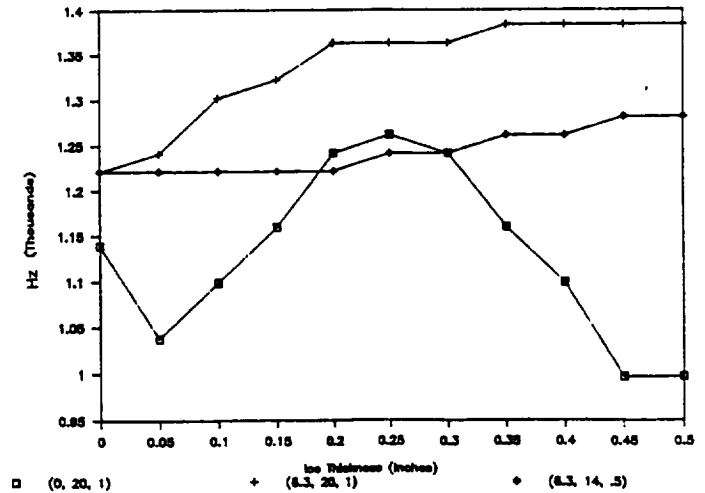
(e) Power in Freq Band 1150-1800 KHz



(f) Power in Freq Band 1800-3000 KHz

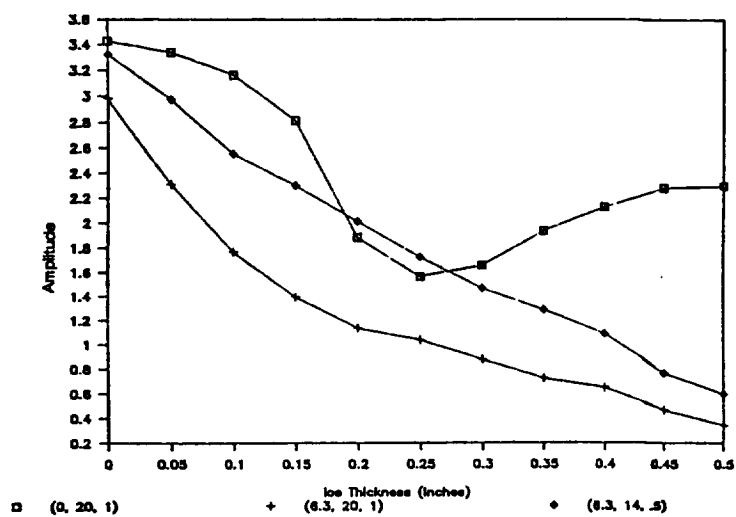


(g) Ratio of Smallest & Largest Power

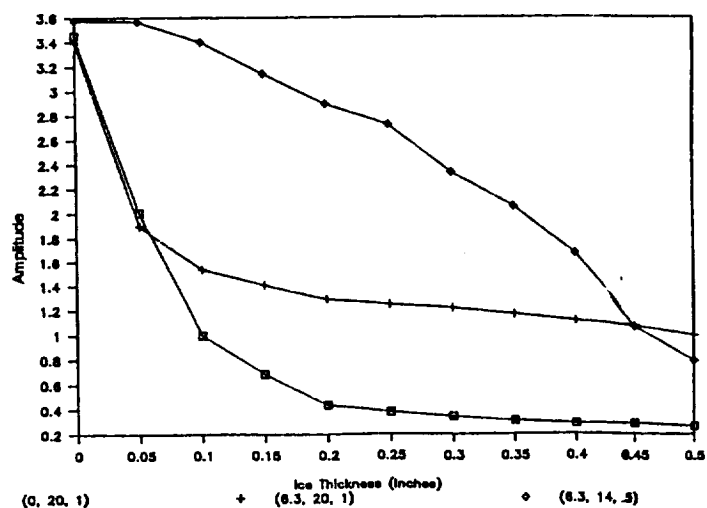


(h) Freq with 25% of Energy

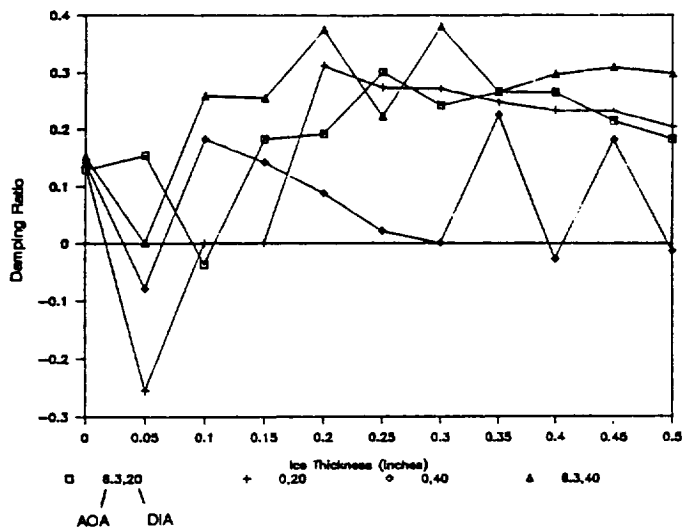
Figure 10 - Concluded



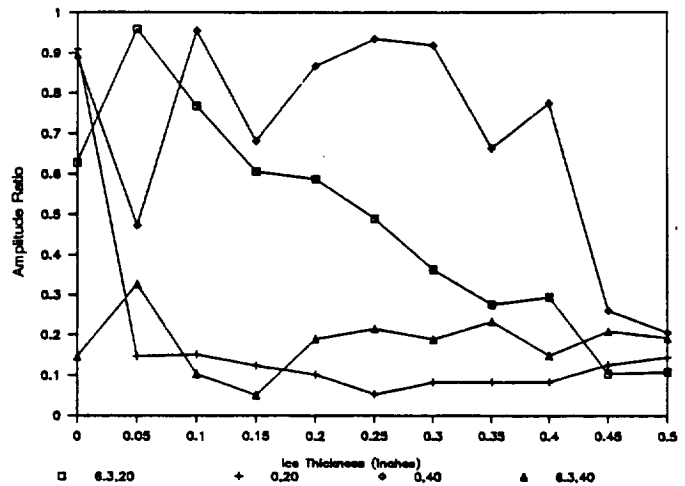
(i) Transfer Function 1



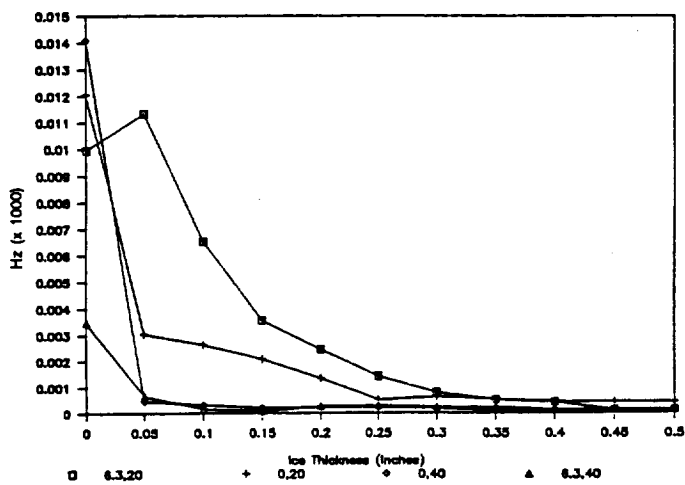
(j) Transfer Function 2



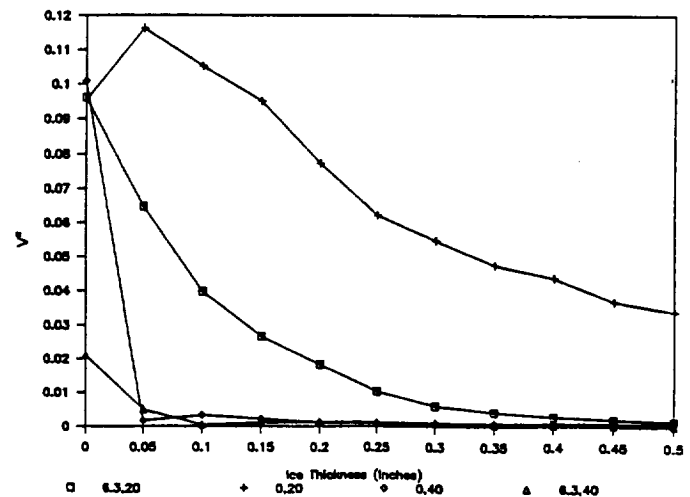
(a) First Local Damping



(b) Amp Ratio of 2 Biggest Peaks



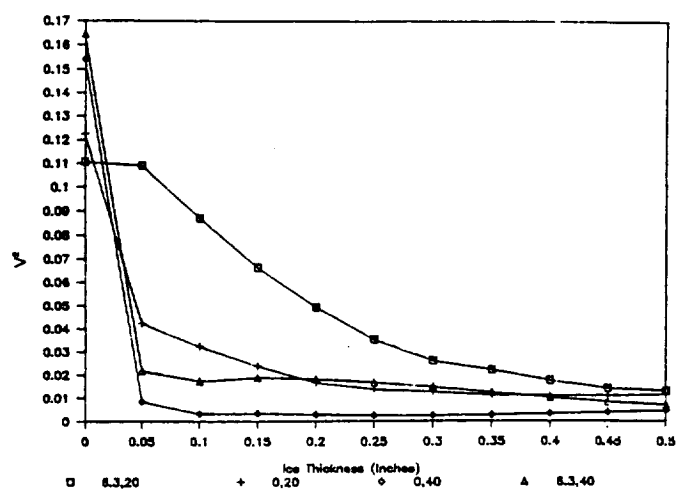
(c) Freq Difference of 2 Biggest Peaks



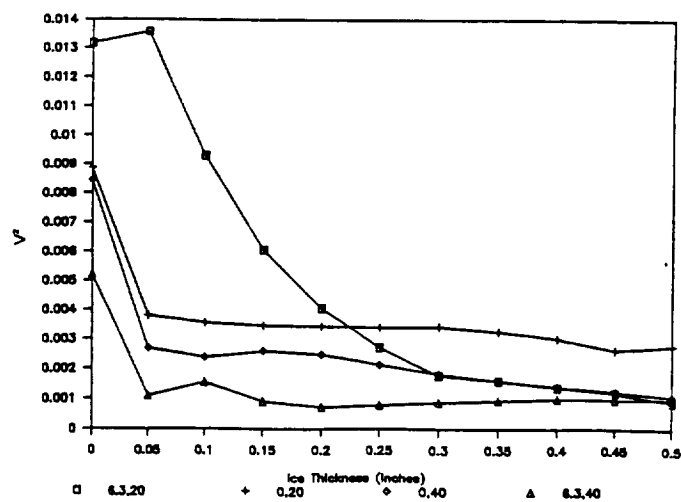
(d) Power in Freq Band 700-1150 KHz

Figure 11 - Sensor 4 Test Conditions: -9°C , 1 g/cm^3 LWC, variable AOA & DIA

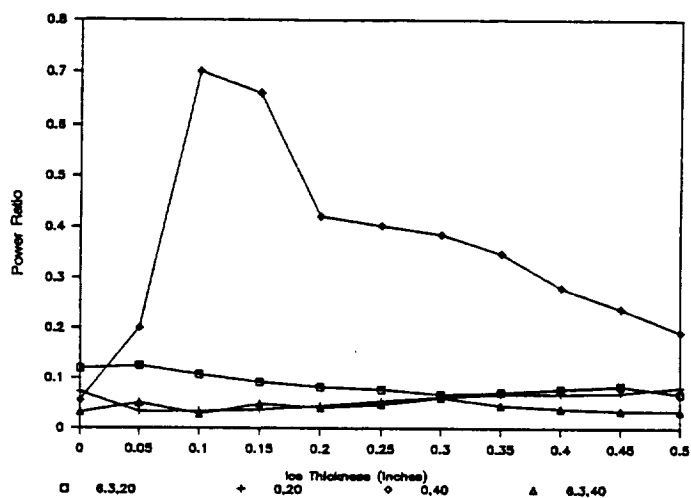
Figure 11 - Continued



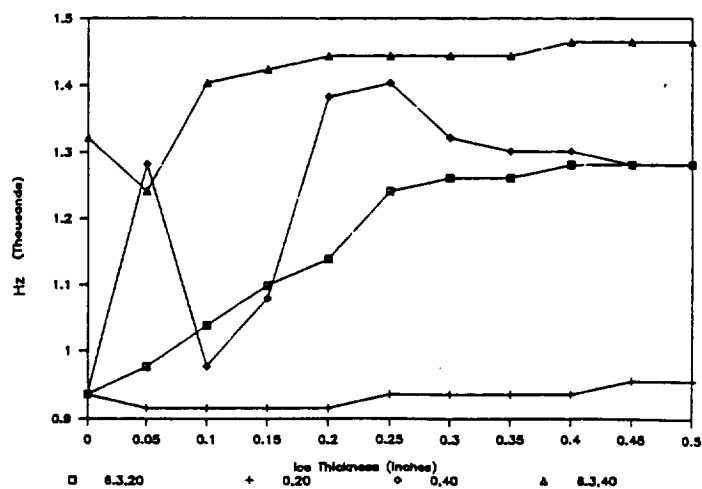
(e) Power in Freq Band 1150-1800 KHz



(f) Power in Freq Band 1800-3000 KHz

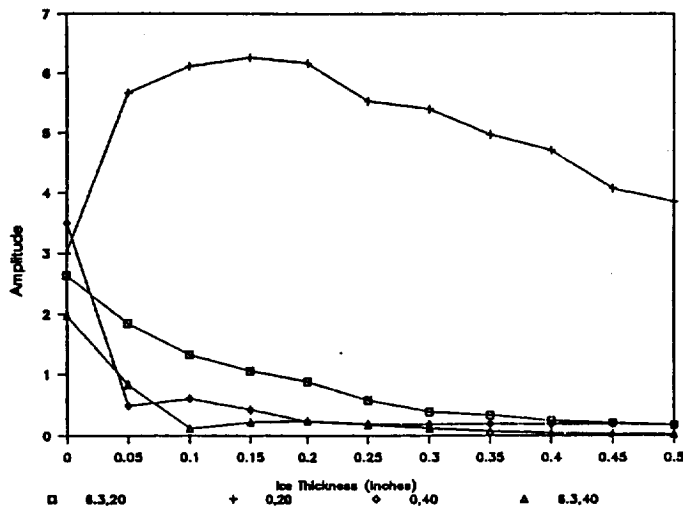


(g) Ratio of Smallest & Largest Power

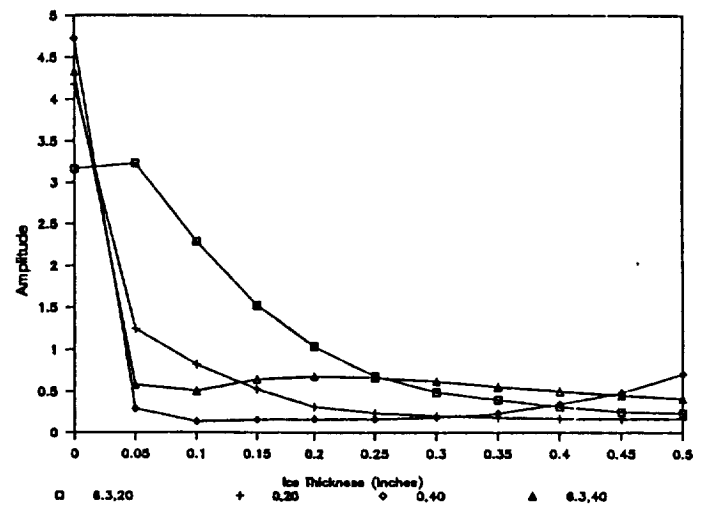


(h) Freq with 25% of Energy

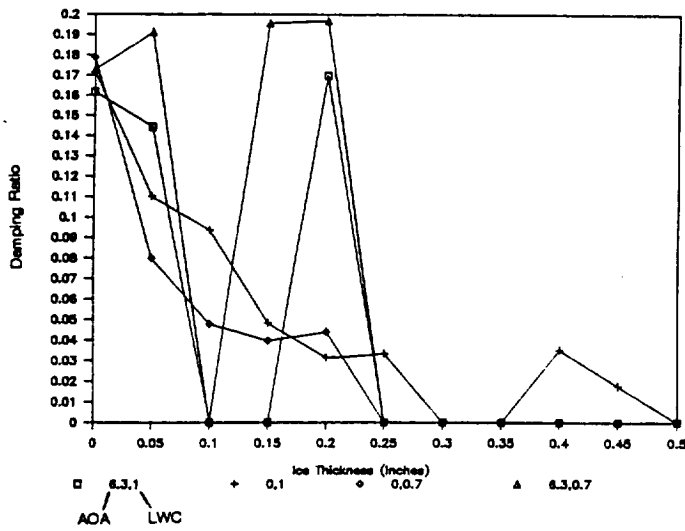
Figure 11 - Concluded



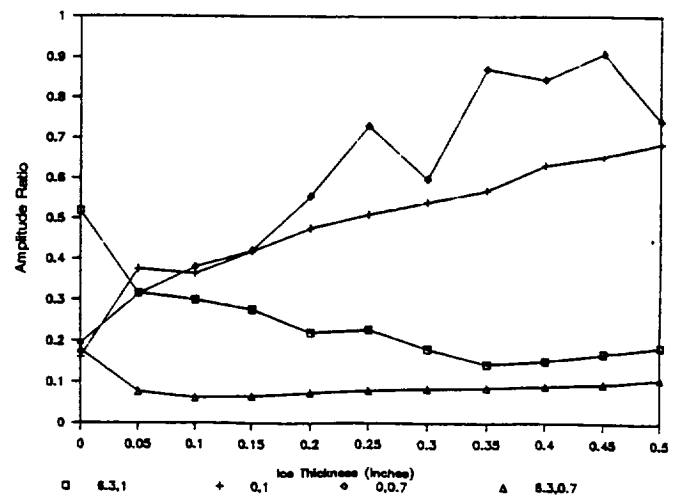
(i) Transfer Function 1



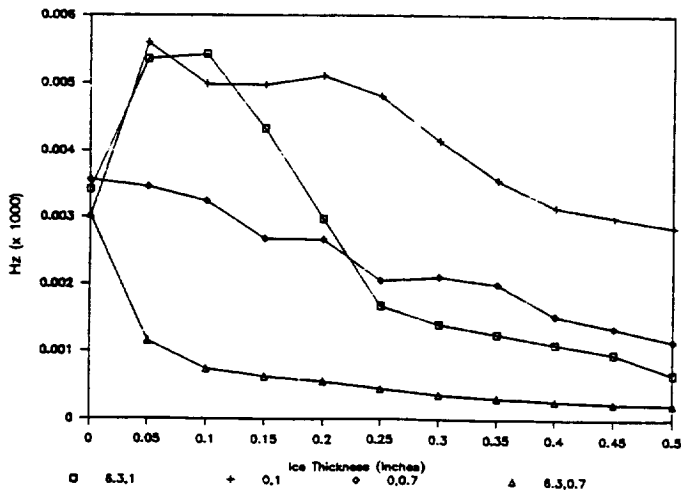
(j) Transfer Function 2



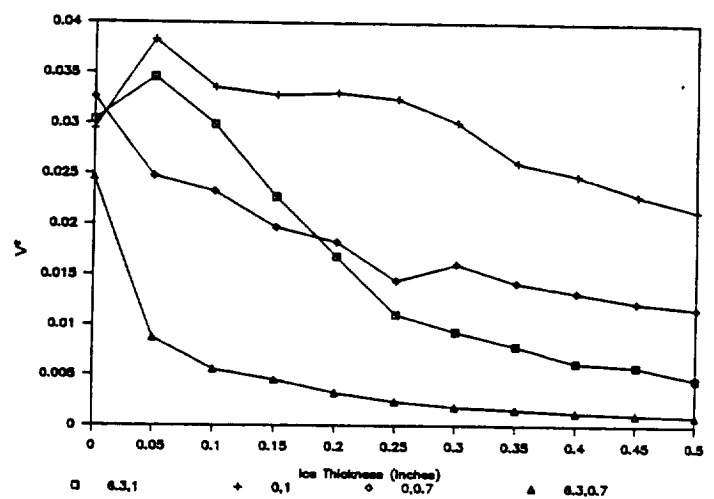
(a) First Local Damping



(b) Amp Ratio of 2 Biggest Peaks



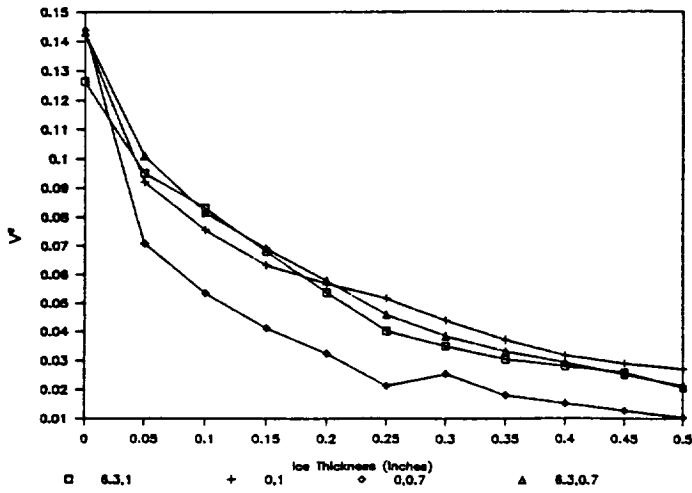
(c) Freq Difference of 2 Biggest Peaks



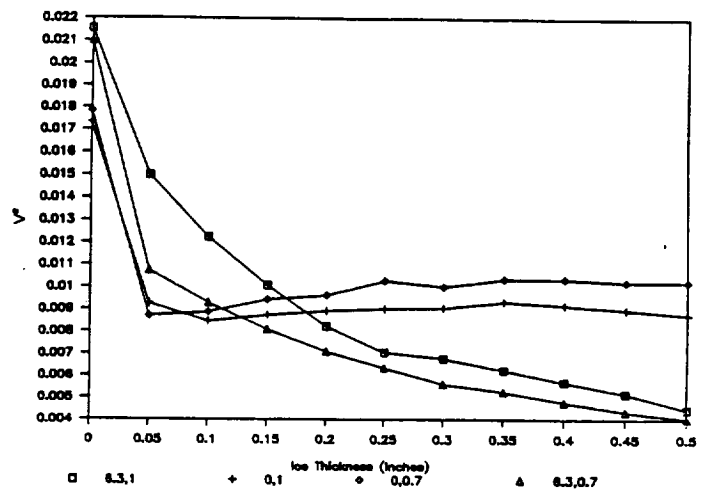
(d) Power in Freq Band 700-1150 KHz

Figure 12 - Sensor 4 Test Conditions: -23°C, 20 μ m DIA, variable AOA & LWC

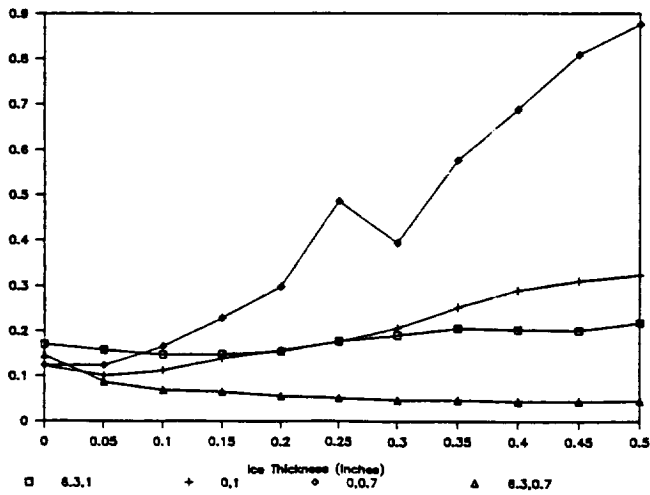
Figure 12 - Continued



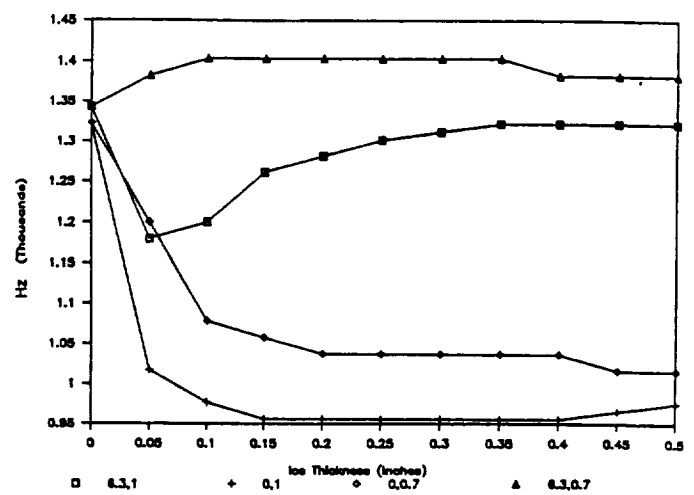
(e) Power in Freq Band 1150-1800 KHz



(f) Power in Freq Band 1800-3000 KHz

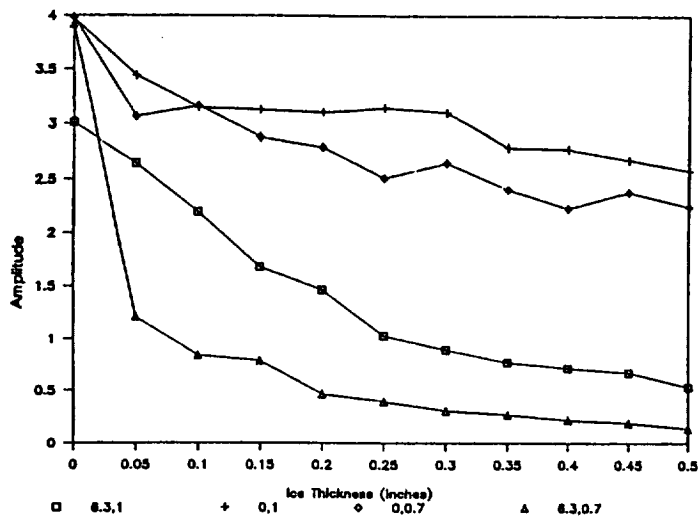


(g) Ratio of Smallest & Largest Power

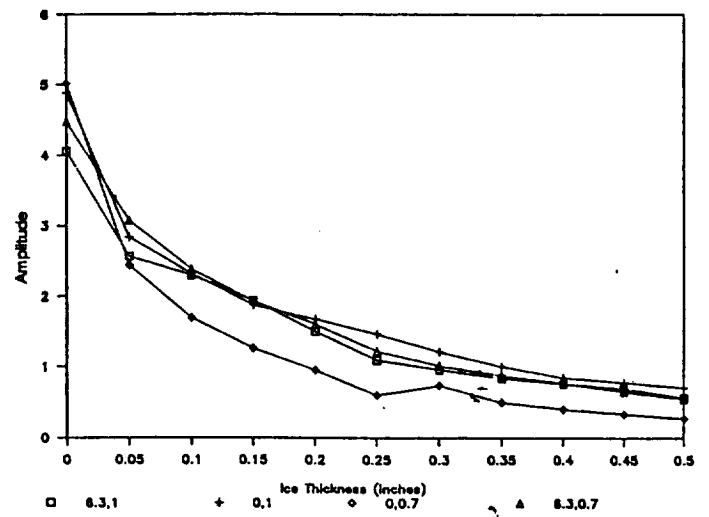


(h) Freq with 25% of Energy

Figure 12 - Concluded



(i) Transfer Function 1



(j) Transfer Function 2